THÈSE

En vue de l'obtention du

DOCTORAT DE L'UNIVERSITÉ DE TOULOUSE

Délivré par :

Institut National Polytechnique de Toulouse (INP Toulouse)

Discipline ou spécialité :

Microondes, ElectroMagnétisme, Optoélectronique

Présentée et soutenue par :

Lucie CAMPAGNOLO

le : vendredi 26 avril 2013

Titre :

Optical Feedback Interferometry sensing technique for flow measurements in microchannels

Ecole doctorale :
Génie Electrique, Electronique et Télécommunications (GEET)

Unité de recherche :
Laboratoire d'analyse et d'architecture des systèmes (LAAS)

Directeur(s) de Thèse :
Prof. Thierry Bosch

Rapporteurs :

Prof. Guy Plantier
Prof. Santiago Royo

Membre(s) du jury :
Dr. Abdallah Ougazzaden
Prof. Guy Plantier
Prof. Santiago Royo
Prof. Thierry Bosch
Dr. Julien Perchoux
Prof. Eric Lacot

i

Ô Lac !
L'année à peine a fini sa carrière,
Et près des flots chéris qu'elle devait revoir,
Regarde ! je viens seul m'asseoir sur cette pierre
Où tu la vis s'asseoir !

Alphonse de Lamartine (1820)

Remerciements

Je tiens à exprimer mes plus chaleureux remerciements à Thierry Bosch qui fut pour moi un directeur de thèse attentif et disponible malgré son emploi du temps chargé. Ses compétences scientifiques ainsi que sa clairvoyance et sa patience m'ont beaucoup appris.

J'ai eu l'honneur d'être la première doctorante encadrée par Julien Perchoux, et je le remercie pour sa disponibilité, son aide et son amitié tout au long de ses trois années.

Je remercie cordialement M. Abdallah Ougazzaden d'avoir fait l'honneur d'accepter de présider mon jury de thèse. Je souhaite également adresser mes sincères remerciements à Messieurs Santiago Royo, Guy Plantier et Eric Lacot d'avoir accepté d'examiner mon travail.

J'adresse toute ma plus profonde gratitude à mes collègues et amis australiens, et en particulier à Aleksandar Rakìc, qui m'a accueillie dans son laboratoire, son université et dans sa famille pendant mes séjours en Australie. Je remercie Yah Leng Lim pour sa rigueur scientifique et ses alignements optiques imbattables, Milan Nikolìc (Mikan le destructeur de lignes) pour avoir appris le français avec des podcasts écossais, Karl Bertling pour son soutien inconditionnel à tout heure du jour et de la nuit, Russel Kliese pour sa bibliographie infinie et toute l'équipe de UQ pour leur accueil chaleureux.

Je remercie toutes les personnes du LOSE/LAAS-OSE (suivant la période) qui ont contribué à la réalisation de cette thèse, et en particulier Francis Bony sans qui l'idée d'appliquer le self-mixing à la fluidique ne se serait peut-être pas concrétisée si facilement, Francis Jayat et Clément Tronche pour avoir monté les manips les plus tordues en un temps record, et Jean-Claude Csont pour son don inné en mécanique.

Un grand merci à Emmanuelle Tronche, Pierre Lescure, Françoise Lizion, Han-Cheng Seat, Olivier Bernal, Chiarra Fillipini et Emilio Ramirez Miquet.

Je remercie également Raphael Teysseyre, Antonio Luna, Florent Bouyjou, Emmanuel Moutaye, Bendi Tanios, Blaise Mulliez, Lucas Perbet et Us-

v

Contents

vii

List of Figures

xii

xiv

List of Tables

1

Introduction

The invention of the light microscope during the XVIIth century allows the human eye, by means of a lens or combinations of lenses, to observe enlarged images of tiny objects. It made visible the fascinating details of a micro-world, which was until then unsuspected. From that time on, continuous technical headways have enabled the fabrication and study of various microsystems.

The evolution of microelectronics highlights perfectly the impact of the device miniaturization on modern technology. In particular, semiconductor industry has benefited from this evolution. Since 1960, the size of a transistor has decreased from 1 cm to the 28-22 nm range in 2011. Therefore, the advancements in the field of microelectronics have enabled the process of extremely small devices, for applications as diverse as micromechanics or biology. The advantages of device miniaturization are a reduced size, weight and cost, and a rise of the device's performance and of the calculation speed.

Microfluidic devices are a specific sort of microsystems used for transporting liquids or gases. At first, the main interest for downscaling flowchannels was to improve the device's performance in the field of analytical chemistry. In electrophoresis for example, when the size of a device is reduced by 10, the reaction time is divided by 100 [16]. The reduction of chemical reagent, and the possibility of performing multiple parallel analyses on the same chip appeared to be a significant motive for reducing the size of fluidic devices. The original idea was that photolithography and associated clean room technologies that had been so successful in silicon microelectronics, would be directly applicable to microfluidics. As a matter of fact, the first modern microfluidic devices, developed by Manz et al. [17], were fabricated in silicon and glass using conventional, planar fabrication techniques (photolithography and etching) adapted from the microelectronics industry.

However, polydimethylsiloxane (PDMS), which is a silicon-based organic polymer, appears to be an appropriated material for the fabrication of microfluidic devices. PDMS is an inexpensive and flexible material, and is optically transparent down to 230 nm [18]. Therefore, it is compatible with many optical methods for detection. It is also compatible with biological studies because it is impermeable to water, non toxic to cells, and permeable to gases. Finally, a major advantage of PDMS over glass and silicon is the ease with which it can be fabricated and bonded to other surfaces. In addition, to cover a range of complex applications, new materials and microfabrication techniques were tested (microcontact printing [19], microtransfer moulding [20], Polymer-based channels [21] ...). Consequently, the average dimension of microchannels has been reduced from 1 μm in 1998 [22] down to 30 nm in 2011 [23].

Microfluidics deals with the behavior, the precise control and the manipulation of fluids. Some applications of microfluidics are introduced here, to give a general overview of this multidisciplinary field intersecting engineering, physics, chemistry, microtechnology and biotechnology.

First, microfluidic devices are of great interest to miniaturize and parallelize classical immunologic and genomic detection assays [24]. On-chip real time polymerase chain reaction (for DNA copy) [25], immuno-sensors (to detect the presence of a substance in a liquid sample) [26], and microarrays [27] belong to the most promising technologies for biological agents or markers detection. For example, a simple drop of blood can be divided into one thousand microdrops in order to perform parallel analysis at the same time. This method can easily replace standard methods, asking for a larger quantity of reagent and a longer reaction time. It is also possible to replicate DNA sequence from a tiny initial quantity to detect genetic disorders [28,29], avoiding invasive analysis. New "Labs-on-a-chip" can provide up to one million copy of a DNA sequence in 30 minutes.

Micro Total Analyzing Systems (μTAS), which can be implanted directly in the human body, are another microfluidic application. μTAS can perform some in-vivo analysis to determine what drug amount the patient needs and adapt the delivered drug dose. The University of Minnesota developed a micropump for drug administration that manages pain and treats neurodegenerative disorders [30,31].

Multiphase flows generators are also of high interest in microfluidics as laminar flows facilitate the generation of monodisperse droplets [32–34]. Emulsions and double emulsions can be used for nanoparticle synthesis or drug microencapsulation [35]. Microdroplets can also be used as single microreactors in biodetection systems [36].

Furthermore, new microfluidic technologies allow the manipulation of discrete, independently controllable droplets, using the modification of the wetting properties of a surface by applying an electric field (electro-wetting). Following the analogy of digital microelectronics, this approach is referred to as digital microfluidics [37].

In rheology, working with low Reynolds numbers, which is the case in small channels, enable to investigate viscous liquids and to study non-linear viscous properties [38]. A number of microfluidic rheometry systems have been investigated and provide an alternative to conventional characterization methods [39,40]. The study of fluids transport across micro-nanofluidic porous media is also of high interest for oil recovery applications in petrol extraction [41]. Moreover, a number of fundamental questions around the slip velocity at the solid-liquid interface can also be investigated using microfluidic devices together with flow visualization techniques [42–44].

Another microfluidics applications is the microchannel reactor, a device in which chemical reactions take place in a confinement with typical lateral dimensions below the millimeter range [45]. It offers many advantages over

conventional scale reactors, including vast improvements in energy efficiency and reaction speed. This lead to better safety and reliability, and allows on-site/on-demand production as processes can be controlled at a much finer degree [46–48].

More examples and detailed applications for integrated microfluidic devices can be found in the enhanced microfluidics review of Erikson [49]. The nascent field of nanofluidics (the study of fluids in channels with nanometre-scale dimensions) indicates that the research on always smaller microchannels is of great interest for future industrial applications [50].

Blood capillaries and artificial microchannels are closely linked. First, small vessels which size varies between 50 µm (arterioles) and 10 µm (capillaries) can be considered as "natural" microfluidic systems [51]. In addition, biological phantoms are developed to mimic the optical and mechanical properties of biological tissues to facilitate sensor design while minimizing animal use, and use microfluidics manufacturing processes.

Theoretically, monitoring fluid flow in microchannels and blood capillaries require the same technology. However, blood capillaries are surrounded by various tissues and other vessels, and their geometry and shape is not regular.

A challenging application for flow measurement in biological tissues is the monitoring of blood microcirculation. For many tasks, like the diagnosis of burn depth or the inflammation of subcutaneous blood vessels, only the visualization of blood flow is necessary [52, 53]. Blood flow monitoring is usually more convenient than microfluidics complex devices, insofar as high spatial and temporal resolution is generally not needed. In most cases, the capillary blood flow is almost stationary, and the determination of the volume flow rate from the measurement of the mean velocity is possible under the assumption of a parabolic velocity profile in the channel [54]. Nevertheless, higher spatial resolution may be required for the evaluation of volume flow rates when the velocity profile is unknown (e.g. in bends, bifurcations, non-circular vessels, and near flow obstacles) [55, 56].

Finally, measuring the blood flow flow is of great interest in the early detection of malignant melanoma. Nowadays, diagnosis of melanoma involves a magnification technique (dermoscopy) in which benign nevi and malignant melanoma can be discriminated by observing differences in form and colour (ABCD rule) [57]. However, while malignant melanoma and benign nevi are similar in appearance, their origins are completely different. In a malignant melanoma, malignant transformation needs a rapid increase of nutrients and oxygen supply for the cancer cells, leading to the development of new blood vessels around the tumour. Consequently, a local rise of the blood flow velocity can indicate a melanoma, and monitoring blood perfusion in the area of suspected tumours can contribute to early cancer detection [58, 59]. Thus, the detection of early melanomas that lack specific dermoscopic criteria can

be meliorate by considering blood flow increase as an indicator of possible presence of melanoma.

The miniaturization of flowchannel leads to a need of non-invasive sensors with a very high resolution, to measure fluid flow rates and flow profiles. In particular, the emergence of bio and nano technologies gave a boost to the resolution of traditional optical sensors. Optics components became assembled into compact detectors to develop portable instrumentations based on microfluidics devices, generating a new field of research "Optofluidics".

Thus, this thesis presents a compact, low-cost, high-resolution sensor based on optical feedback interferometry (OFI) that accurately measure the local velocity of a fluid for microfluidics applications. The present work describes the theoretical background, as well as the hardware and signal processing required to size and develop such a sensor. The thesis manuscript has been written with the following order:

The first chapter has been dedicated to a review of existing optical technologies for flow measurement in microchannels, highlighting how the submillimeter spatial resolution has been reached. Well-documented techniques of Laser Doppler Velocimetry (LDV), Particle Image velocimetry (PIV), Speckle related techniques and Dual-slit are described following a chronological order. A particular attention is paid to OFI, in order to lay the foundation of this thesis.

The second chapter is an introduction to the theory of OFI. In its first section, the equivalent cavity model, that describes the steady state behaviour of a laser diode suffering from optical feedback, is used to derive the expressions for the threshold gain and allowed emission frequencies, as well as the phase and the optical output power. In the second section, we propose an equivalent cavity model adapted to velocity measurement, when the distance to the target is constant. The modified expressions for the phase and the optical output power are presented and discussed.

The third chapter presents a major portion of the research work achieved during this thesis. It starts by identifying the differences between well-known rough targets and colloidal suspensions, and by presenting an adaptation for flow measurement of the model described in chapter II. Then, the experimental set-up used to measure fluid velocity is detailed. Typical experimental OFI signals for fluid flow measurement are presented, and their variations with flow rate are studied, leading to the development of relevant signal processing methods for flow rate calculations. In addition, the effects of set-up parameters on the signal's shape are investigated. Moreover, appropriated signal processing methods are proposed to calculate the flow rate of a liquid

in critical configurations (i.e. when the signal deviates from the theoretical behaviour). Finally, a special attention is paid to multiple scattering effects, that occur when the density of seeding increases, and strongly affect the sensor performance.

The fourth and final chapter presents the reconstruction of velocity profiles inside channels of various dimensions (from 100 μm to 3 mm). The velocity profile of the liquid is directly measured, thus avoiding the need for model-based profile calculation and uncertainties inherent to this approach. The sensor presented in Chapter III, as well as the corresponding signal processing methods, are validated by successfully extracting the flow profiles in both Newtonian and Non-Newtonian liquids.

Finally, a general conclusion is proposed.

Chapter I

Optical sensors for flow measurement

I.1   Introduction

The exponential growth of microfluidics in the last decade has been demanding accurate flow measurement. A variety of liquid flow sensors have been developed, based among others on thermal, electrical, mechanical and optical principles.

Ultrasonic Doppler velocimetry is one of the most conventional techniques in fluid characterization and blood circulation measurement, and an enhanced description of this technology can be found in the following books and articles [60–62].

Techniques for extracting flow velocity information from nuclear magnetic resonance imaging (MRI) are reviewed by Smith [63] and Bradley [64].

Single photon emission computed tomography and positron emission tomography are reviewed by Lodge et al. [65], Cuocolo et al. [66] and Zhao et al. [67]. Computational fluid dynamics techniques are exhaustively studied by Anderson [68] and Chung [69].

A range of methods for injecting and tracking scalar markers including laser-induced fluorescence, flow-tagging velocimetry, molecular tagging velocimetry, laser-induced molecular tagging and Infra-Red thermal velocimetry have been described by Sinton [70].

The review in this chapter is restricted to non-invasive optical methods that measure directly fluid flows and velocities in microchannels. Optical techniques for fluid flow measurement are non-invasive and provide a good compromise between spatial resolution, temporal resolution, and cost. As compared to optical methods, MRI exhibits a very high spatial resolution but a poor temporal resolution and an extremely high cost. On the other hand, Ultrasound sensors provide real time measurement for a satisfying compactness and price, but the spatial resolution is not high enough to investigate the velocity distribution in sub-millimeter channels. Computational fluids dynamics techniques and positron emission tomography are advanced techniques, which are more suitable for complex applications, but not appropriated for low-cost microfluidics devices.

In this chapter, the historical development of optical flowmeters is described, and the evolution of theses techniques to catch the microfluidic evolution is investigated. A special attention is paid to two standard and widely commercialized optical sensors, the Laser Doppler Velocimeter (LDV) and the Particle Image Velocimeter (PIV). In addition to theses well-known techniques, there is large amount of performing and inventive flow sensors, and technical advancements provide continuously new ones.

I.2 The Laser Doppler Velocimeter (LDV)

Laser Doppler Velocimetry (LDV), also known as Laser Doppler Anemometry (LDA) is an optical interferometric technique based on the Doppler effect to measure local fluid velocity. LDV was applied to flow rate measurement in the 60's, becoming historically the first mature technique to measure fluid velocity. From then on, LDV has shown a stable and steadily growing development, and is now a well-proven commercialized technique that measures fluid velocity accurately and non-invasively.

I.2.1 History : first LDV configuration

In the 60's, the only non-invasive technique to measure a flow pattern consisted in injecting dyes into the fluid stream [71], and in observing the stream lines produced by the dyes as there are carried by the current. Beside the fact that this method was difficult to set-up, it provided only quantitative results and was inaccurate for low velocities, due to the dominance of diffusive effects. Therefore, in 1964, Yeh and Cumins proposed to utilize a laser spectrometer that they had previously developed for Rayleigh diffusion broadening measurements [72] to measure locally the velocity of a fluid [1]. The basic principle of this first Laser Doppler Velocimeter (LDV) was to use **the Doppler effect** to measure the velocity of small scattering particles immersed into a fluid under test. The Doppler effect in light scattered by particles embedded in liquids is detailed in Appendix A.

In Yeh and Cummins first experimental set-up, the laser beam of a He-Ne gas laser was divided by a beamsplitter; one beam acted as a local optical oscillator, while the other beam illuminated a volume of polystyrenes spheres in water. The two beams were recombined on a photomultiplier, and the beat signal was processed to recover the frequency shift induced by the motion of the scattering spheres. A simplified schematic of the first LDV experimental set-up is presented in Fig. I.2.1.

They demonstrated a linear relationship between the flow rate and the beat frequency measured on the photomultiplier, and they reconstructed 11 % of the velocity profile in the middle of a circular 10 cm flow-channel. The solution had a laminar behaviour (See Fig. I.2.1), and the theoretical flow profile is known by the Poiseuille's law [73]. The resolution of their system, limited by the beam diameter, has been estimated to be 0.16 cm. This first experiment opened the way to the study of many fluidic systems.

In 1966, Foreman et al. [74] presented an improved version of Yeh and Cummins LDV to measure velocities in liquids and gases, when the particles' size and concentration is not consistent. They used tap water and the impurities it may contain instead of size-calibrated polyspheres, and they successfully reconstructed the entire velocity profile in a 1.2 cm diameter

(a)

(b)
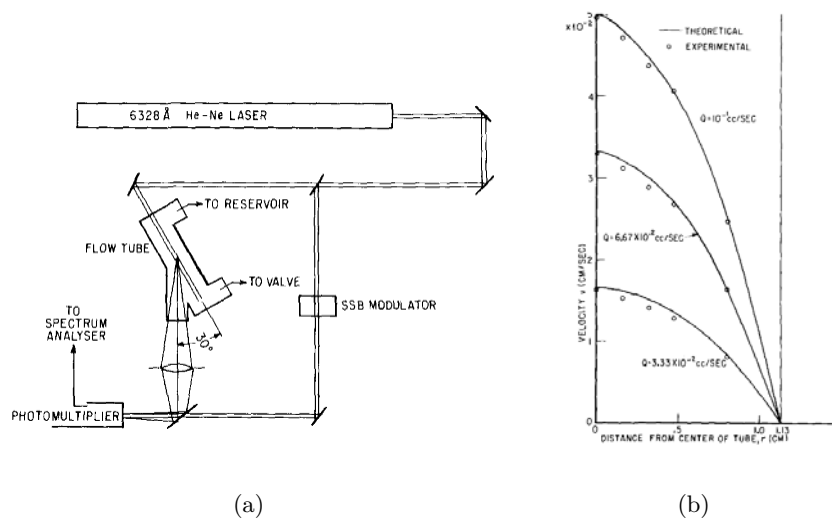
Figure I.1: First LDV for measuring fluid flow, proposed by *Yeh and Cummins in 1964* [1] (a) Experimental set-up : The light source was a He-Ne gas laser emitting at 632.8 nm, the FUD was a circular 10 cm diameter tube containing a solution of polystyrene spheres. (b) The flow was laminar, and the velocity profile following Poiseuille law has been reconstructed for several pumping rates.
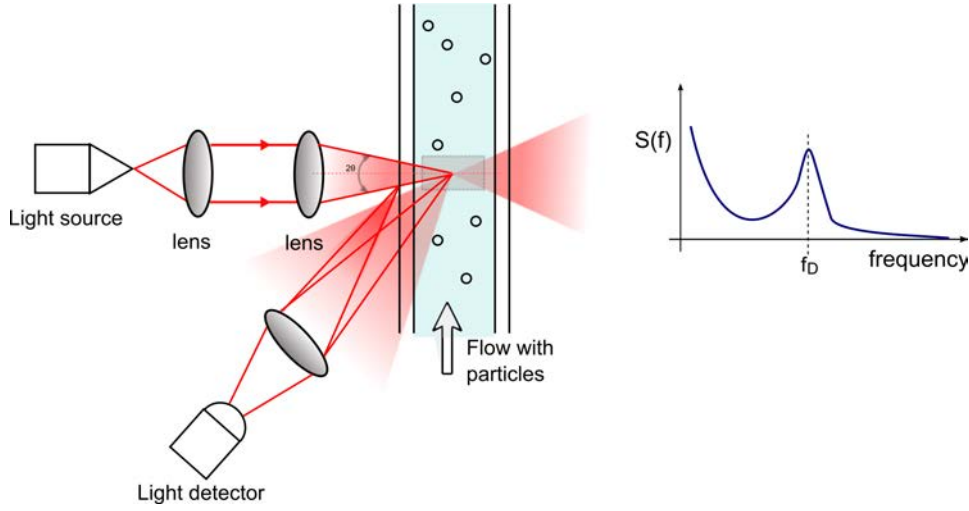
Figure I.2: Schematic plot of a LDV in single-beam configuration.

circular pipe.

I.2.2 Sensing scheme

I.2.2.a Interferometric sensing scheme : single beam configuration

A basic implementation of LDV consists in illuminating a part of the flow field with a laser beam, in collecting some of the light reflected from it, in mixing it with the original light and in measuring the resulting beat frequency. A schematic plot of the LDV principle is presented on Fig. I.2.

This technique provides a linear relationship between the measured Doppler frequency f_D and the particles velocity in the detection volume:

$$f_D = \frac{2Vn\sin(\theta)}{\lambda} \tag{I.1}$$

where V is the velocity of the particles embedded in the liquid, acting as seeding, n is the refractive index of the surrounding aqueous phase, θ is the angle between the laser beam and the fluid velocity direction, and λ is the wavelength of the laser.

I.2.2.b Interferometric sensing scheme : dual beam configuration

Another LDV configuration considers two beams obtained by splitting a single beam, in order to ensure the coherence between the two (Fig. I.3). A transmitting optic focuses the beams to intersect at their waist in the
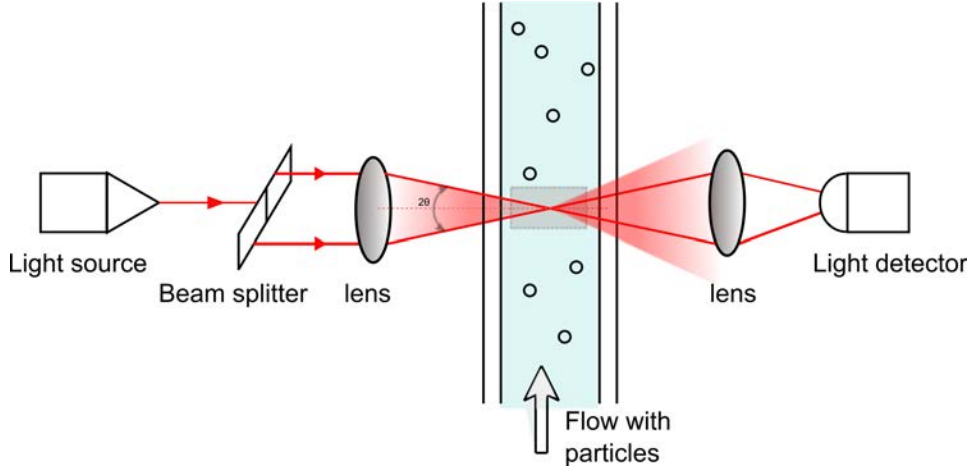
Figure I.3: Schematic plot of a LDV in dual-beam configuration. The two incident beams are crossed at their waist, and the velocity of the particle is recovered from the detected signal fluctuations.

fluid, where they interfere and generate a set of fringes. As a particle passes through the fringes, light is reflected. It is then collected by a receiving optics, and focused on a photodetector.

Lets consider a particle moving along the flow direction at a velocity V. This particle travels through the detection volume, and is illuminated from two different directions. For the upper left beam in Fig. I.3, the particle is moving towards the laser at a velocity $-V\sin(\theta)$. For the other beam, the particle is moving away from the laser, and the velocity component is $V\sin(\theta)$. Therefore, the frequency shift of the reflected light is different for the two laser sources. The resulting beat frequency depends on the angle of the two laser beams θ and the tracer velocity magnitude V, and can be written:

$$f_D = \frac{nV\sin(\theta)}{\lambda} - \frac{(-nV\sin(\theta))}{\lambda} = \frac{2nV\sin(\theta)}{\lambda} \tag{I.2}$$

where V is the particle velocity, 2θ the angle between the two incident beams, n the refractive index of the fluid aqueous phase, and λ the laser's wavelength.

I.2.2.c Fringe crossing detection scheme

In 1969, Rudd proposed an alternative model to explain the LDV mechanism [75]. The Doppler effect is interpreted in term of scattering centres crossing a set of fringes, rather than actually causing a shift in the light
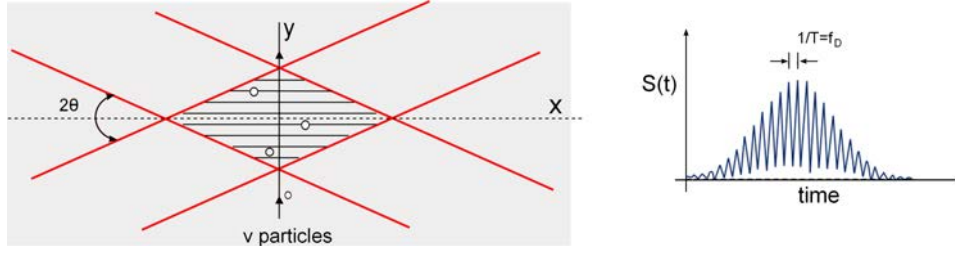
Figure I.4: Schematic illustration of two laser beams forming interference fringes

frequency. He also demonstrated that the two approaches are entirely equivalent.

When the two beams described on Fig. I.3 intersect, a fringe pattern is created. When the two incident waves are in phase, constructive interferences appear, locally leading to a maximum of intensity (bright fringes), whereas when the two incident waves are in antiphase, destructive interferences occur, leading to a minimum of intensity. This pattern is fixed in space, and this is a direct consequence to the fact that the two incident beams have the same frequency. The dark and bright fringes are equally spaced, and parallel to the line bisecting the angle between the two beams. The spacing between dark and bright fringes s is defined as:

$$s = \frac{\lambda}{2n\sin(\theta)} \tag{I.3}$$

Where θ the half-angle between the two incident beams.

When a tracer particle moves along axis y in Fig. I.4, and crosses a bright fringe, it will reflects light on the photodetector, whereas when it crosses a dark fringe it will not reflect any light. The intensity of the light received by the photodetector will fluctuate with a regular period. The photodetector records a signal burst, whose amplitude is modulated by the fringe pattern. The frequency of the modulation f_D induced by the particle moving at a velocity V is described as:

$$f_D = \frac{V}{s} = \frac{2nV\sin(\theta)}{\lambda} \tag{I.4}$$

The two approaches lead to the same result, and the shift of frequency can be detected in frequency domain as well as in time domain, opening the way for versatile sensors based on this technique. From there, research teams implemented the more appropriate LDV configuration, regarding to their experimental constraints.

14

I.2.3 LDV technical evolution

Basic LDV configurations suffered from severe technical limitations. During the next decades, various complicated and sophisticated LDV systems were built, improving drastically their performance. At the end of the 90's, LDV systems provided 3D flow profiles, could discriminate the flow stream direction, and had a better resolution by using semiconductor elements instead of traditional gas lasers.

Use of optical fibers The ease of handling of LDV systems was a prime motivation for the development of fiber-optics probes, which can now be found in most of LDV applications. Fiber-optics probes provided a higher degree of spatial and temporal resolution [76, 77].

Semiconductor components The LDV had to be simplified optically in order to become an operational instrument, compact, reliable, easy to align, and usable out of optical laboratories. Gas lasers were replaced by laser diode, and the use of pin or avalanche diodes as detectors became standard [78].

Multi-velocity-components systems Measuring 2 or 3 components of the velocity in a channel has been recovered by several techniques: 2 or 3 stand-alone sensors arrangement [79], with polarization changes [80], or colour coding [81]. Crosswy et al proposed a system using a dual orthogonal bragg cell that spilt a beam into 4 beams to measure with one system two velocity components [82].

Full-field approach To avoid scanning, Serov et al. [83] replaced the widely used avalanche photodetector by a complementary metal oxide semiconductor image sensor (CMOS), leading to high speed flow imaging of larger surface.

I.2.4 LDV applied to blood flow measurement

The principal goal of research groups working on LDV for biomedical applications was to build a practical instrument for clinical use. Flow measurement in human retinal vessels was the easiest way to demonstrate that in-vivo human blood flow measurement was possible [84]. The next step consisted in measuring the human skin blood flow [13,85]. A small and relatively inexpensive laser was used, in order to permit reasonable cost as well as portability. The laser was coupled with a fiber-optic probe that can be placed on any skin surface. As a matter of fact, for many applications such as the diagnosis of burn depth or the monitoring of healing, it is sufficient

to visualize the change in blood perfusion [83, 86]. Nowadays, Moor instruments commercializes LDV for micro circulation visualization in clinical use (Post operative flap monitoring, prediction of amputation levels, burn depth investigation, cerebral perfusion following injury etc..)
More details about LDV applied to blood flow measurement, including the effect of skin and surrounding tissues can be found in Appendix B.

I.2.5 LDV applied to microfluidics

A micro-scale volume is clearly desirable for microfluidics measurement. LDV sensing volume characteristic dimension is on the order of hundred of micrometers. Reducing the sensing volume introduce severe constraints on the system that can limit its performance. Despite of theses limitations, some sensing volumes of micrometer size have been achieved. Compton and Eaton used a short focal length to obtain a measurement volume of 35x66 µm [87], and with the same technique, Tieu et al. demonstrated the laminar profile reconstruction with a 10x5 µm detection volume [88].

In 2010, Buttner et al. optimized the LDV profile sensor set-up using computed simulation and achieved a spatial resolution of 1.2 µm with a relative uncertainty on the velocity of 0.25 % [89]. Lately, the same research team demonstrated a spatial resolution of 960 nm, which is to the author's knowledge, the highest ever achieved in LDV applied to microfluidics [90].

I.3 Particle Image Velocimetry (PIV)

Particle Image Velocimetry (PIV) is the most advanced technique to measure accurately and instantaneously 2D velocity vectors in a fluid medium. Based on the acquisition of two high-defined images of a flow seeded with particles, the displacement of a particle during a known time is calculated and the corresponding velocity vector is extracted. PIV is the standard tool in microfluidics laboratories for flow study, and until now, provides the highest spatial resolution.

I.3.1 From Laser Doppler Velocimetry to Laser Speckle Photography

At the early stage of its development, LDV could measure the instantaneous velocity at a single point in a fluid. This particularity made this technique attractive for measuring the average flow at a local position in very small channels, due to this high spatial resolution. However, to obtain the entire flow pattern, the measurement has to be repeated at different locations in the liquid. Two solutions were proposed to overcome this limitation:

- To develop some efficient scanning systems

- To use a completely different approach, the Laser Speckle Photography (LSP) technique [91].

I.3.2   The Speckle effect

The notion of **Speckle** can be seen as follow: When a laser is focused on a rough surface, a high contrast granular pattern appears, on which it is difficult to focus [92]. A distribution of moving particles in a fluid can be seen as a rough surface. When illuminated by a laser beam, it shows a speckle pattern of high contrast.

When a highly concentrated liquid is illuminated by a light wave, each point on the illuminated surface acts as a source of secondary spherical waves. The light in the scattered field is made up of the waves that have been scattered from each point on the illuminated surface. A path-length differences exceeding one wavelength is created, giving rise to phase changes greater than 2π. Thus, the amplitude and the intensity of the resultant light vary randomly. The resulting intensity at a given point on the image is determined by the algebraic addition of all the wave amplitudes arriving at the point. If the resultant amplitude is zero, a dark speckle is seen, while if all the waves arrive in phase, a maximum intensity is observed.

I.3.3   History : first LSP configuration

In the experimental set-up of Grousson [91], a plane of interest within the flow field was illuminated with a thin sheet of light from a double-pulsed laser. A double exposed photograph of the resulting scattered light speckle pattern was recorded. Then, the exposed film was developed and analyzed to construct the velocity field of the particles.

This technique is based on the fact that a photographic record of two identical and mutually displaced speckle structures gives rise to parallel straight fringes [93] (Fig. I.5). The spacing and orientation of these fringes are related to the velocity of the particles.

Barker et al. reconstructed a Poiseuille laminar velocity profile in a circular duct of 12.7 mm diameter [2], and Binnington et al. used LSP to measure turbulent flow in a circular pipe [94].

I.3.4   PIV basics

In 1983, the idea of dividing the double exposure photograph into small interrogation spots and calculating their autocorrelation instead of measuring the spacing and the orientation of Young fringes was proposed for the first time [95]. The name Particle Image Velocimetry (PIV) was then introduced
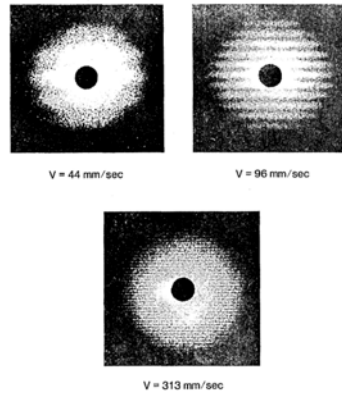
Figure I.5: Young's fringe pattern for various fluid velocities [2].

to distinguish it from the traditional LSP [96].

PIV technique in its final outcome can be described as follows:

1. The movement of tracing particles (introduced or inherent in the fluid) is recorded in two consecutive digital images.

2. The digital images are divided into small interrogation sub-windows.

3. Each sub-window of the second image is compared with different sub-windows of the first image, using cross-correlation algorithms.

4. The most likely displacement of the particle is found for the two sub-windows exhibiting a maximum of correlation.

5. The velocity of the fluid is calculated by dividing the displacement of the particle by the time delay between the two images.

A traditional set-up for PIV measurement is described in Fig. I.6.

This technique was first applied by Barakat et al. to reconstruct the velocity profile in a 14 mm circular duct [97].

As previously for LDV systems, various improvement of the initial sensor were proposed. Among others, the ambiguity about velocity direction has been overcome by Coupland et al. [98], and the measurement of the particle displacement orthogonal to the illumination plane has been demonstrated by Cedenese and Paglialunga [99]. PIV became a mature technique, allowing 3D reconstruction of velocity distribution in a liquid. An illustration of PIV applied to fluid flow distribution in a T-junction is described in Fig. I.7.
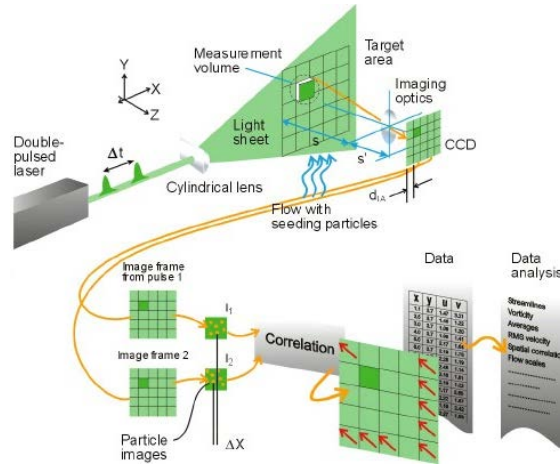
Figure I.6: PIV configuration: two pulses of light illuminate the flow, and the recorded images are compared to estimate the particle velocity *(Source: Dante dynamics)*
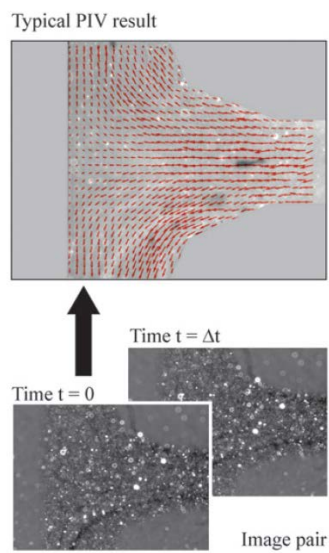
Figure I.7: Two images acquired using PIV from a liquid flowing in a curved T-joint microchannel and it corresponding velocity field. [3]
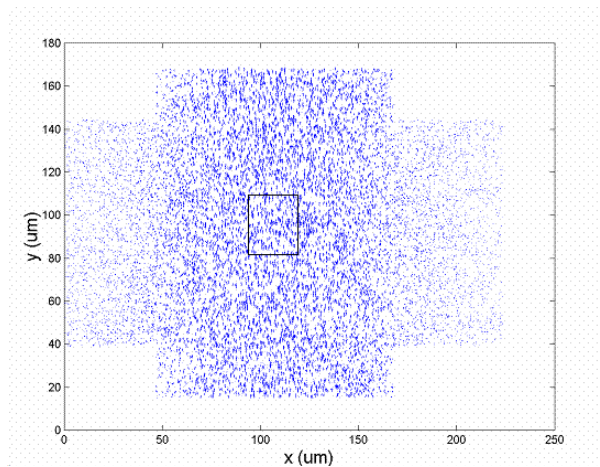
Figure I.8: Particle tracking velocimetry measurements for 500 nm diameter particles in a pressure driven flow through a cross-channel interaction [4]

In the 80's, the greatest challenge was the interrogation of the images, due to the fact that the computer were not powerful enough to complete two dimensional analysis. Therefore, there was considerable interest in less memory-demanding methods, such as tracking particle individually.

I.3.5 Low particle concentration : Particle Tracking Velocimetry (PTV)

Particle Tracking Velocimetry is also known as Low Image Density PIV. In this case, instead of averaging the displacements of many images inside a small interrogation spot, particles are tracked indivually [100, 101].

In practice, a light sheet illuminates the particles while several consecutive images are recorded. After locating the particles in the different recorded frames, their path is calculated and reconstructed. A pair of particles is matched by predicting their position on the next frame, using their momentary velocity. Differences in size, place and shape are taken into account. When the particle paths are known, the total velocity field can be calculated (Fig. I.8).

I.3.6 Recent advance in PIV and μ-PIV: microscale flow measurement

I.3.6.a Super-resolution PIV

To improve the spatial resolution of basic PIV interrogation windows, Keane et al. introduced the super-resolution PIV [102], inspired from PTV algorithm.
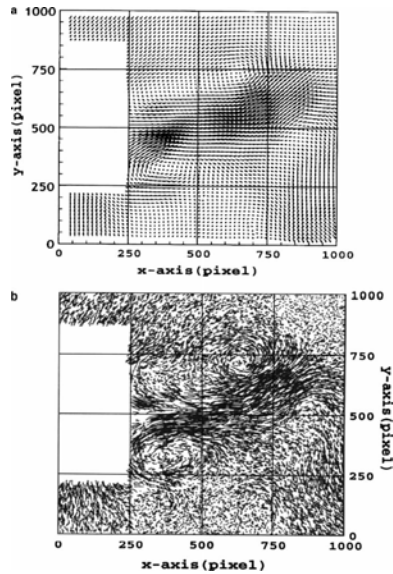
Figure I.9: (a) Flow distribution using standard PIV (b) Super resolution PIV using velocity vectors from (a) to apply PTV algorithm [5]

A standard PIV analysis is first performed using the maximum resolution on interrogation sub-windows. This method provides an estimation of the mean velocity in this area. This mean velocity is then used as an a-priori data, insofar as the vectors from the standard analysis are used to enable reliable image pairing for PTV. An example of the increase of spatial resolution using super resolution PIV is shown in Fig. I.9. Many improvements to this method have been proposed, in order to extend the particle-tracking approach into higher density flow [5, 103, 104].

I.3.6.b   Micro-scale Particle Image Velocimetry: μ-PIV

The adaptation of PIV to microscale flows was demonstrated by Santiago et al. [105]. For μ-PIV, the optical and mechanical configurations are different as volume illumination is used in μ-PIV in opposition to light sheet illumination common in PIV. Fluorescent imaging is typically used to improve the signal and overcome diffraction effects due to small particle size.
μ-PIV applied to microfluidics has been investigated by Meinhart et al. [106], who measured the velocity distribution within a microchannel with a spatial resolution better than 1 μm [107, 108].

However, μ-PIV for microfluidics suffers from two major limitations. First of all, it requires some tracer particles seeding the flow. Due to the small dimension of the microchannels, an appropriate particle size must be chosen such that it is small enough to avoid the channel clogging, and large
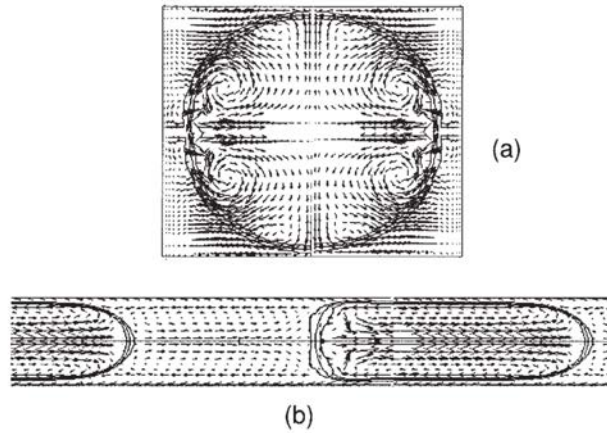
Figure I.10: µ-PIV measurement of the velocity distribution inside a moving droplet. (a)View of the section of the droplet at half its length (b) Longitudinal view [6]

enough to reflect sufficient light. Furthermore, the significant parameters for µ-PIV configuration are the numerical aperture and the magnification of the optical setup, which determine the resolution of the measurements, the field of view, as well as the distance between the microscope objective and the flow. To increase the spatial resolution, the working distance needs to decrease, leading to some mechanical limitations.

The highest resolution in micro-PIV has been achieved by Chuang [109] in 2012. They developed a new algorithm named single pixel evaluation (SPE) in order to enhance the resolution of micro-PIV to its physical limit, one pixel. Thus, they achieved an extremely high resolution of 64.5 nm.

Many techniques derived from µ-PIV have been proposed in the last decade, such as for example evanescent wave µ-PIV, confocal µ-PIV or holographic µ-PIV, and an enhanced description of these new concepts have been fully reviewed by Williams [110].

Nowadays, µ-PIV systems are commercially available. TSI, Dantec Dynamics, and LaVision are the main commercial suppliers of PIV systems and related equipment.

I.3.7   Biomedical applications

Some studies were undertaken to demonstrate that PIV and PTW were suitable techniques for blood flow measurement. However they require a

transparent working medium and optical access to the area of investigation. Thus, the resolution of the acquired frames is affected by the skin, leading to a very low signal-to-noise ratio. A way to overcome this limitation is to use an intravital microscope to reach the blood vessels [111], or to inject fluorescent particles inside the patient [112]. In this configuration, these techniques cannot be considered as non-invasive any more.

I.4 Speckle techniques

In the previous section, we presented the Particle Image Velocimetry, that derived from Laser Speckle Photography technique. However, the research on Speckle effect (described in subsection I.3.2) to measure fluid flow rate split into three directions. Dividing the Laser Speckle Photography in subwindows was the ground idea of PIV, but some other groups showed interest in exploiting the spatial and temporal properties of speckle patterns. Although these two last methods were not as successful as PIV, some interesting achievement were done, especially in the biomedical field.

I.4.1 Laser Speckle Contrast Analysis

In the standard LSP set-up, two thin slits of light are used for illumination. Fercher et al. proposed to use a single-exposure speckle photography, based on the fact that the contrast of a speckle pattern is reduced by speckle fluctuations [113]. This gave rise to a new detection scheme : the Laser Speckle Contrast Analysis (LASCA), based on the study of the spatial statistic properties of Speckle.

The physical principle of LASCA is that in a finite-time laser photograph, the speckle pattern in an area where a liquid is flowing will be blurred to an amount that will depend on the velocity of flow and on the exposure time of the photograph. This blur can be quantified by measuring the contrast of the speckle image K, defined as the spatial standard deviation σ on the mean intensity $\langle I \rangle$ of the photography ratio.

$$K = \frac{\sigma}{\langle I \rangle} \tag{I.5}$$

A single photography of the flow of interest is divided into square of pixels (5*5 or 7*7). Speckle contrast K is measured for each square and its value is assigned to the central pixel in the array. The spatial resolution cannot reach 1 pixel, providing lower accuracy than PIV. However, the strengths of this technique are its simplicity and cheapness.

As for LDV earlier, great interest was shown in applying LASCA to blood flow measurement. And here again, retinal blood flow was the first invivo experiment performed. Instead of processing the Young's fringes of the
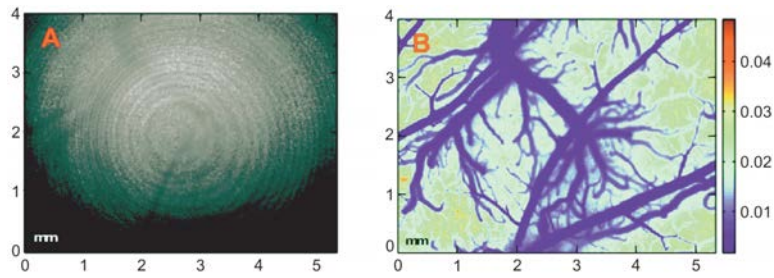
Figure I.11: (a) Single exposure image of rat's cortex(b) Lasca measurement performed on the same image [7]

speckle photography, Briers and Goodman considered the statistic properties of the intensity distribution in the speckle pattern [114, 115]. LASCA is mostly used for skin blood microcirculation imaging (Fig. I.11) but it is not appropriated for very high resolution microfluidics analysis [7, 116, 117].

I.4.2 Laser Speckle Velocimetry (LSV)

Botanical samples, illuminated by a laser, gave rise to a noisy optical phenomenon, attributed to the flow of a water inside a plant [118]. It was reasonable to assume that the light fluctuation were dependent on the flow rate of this liquid, providing information about the motion of this particles by studying their temporal statistics. The first Laser Speckle velocimeter (LSV) was born.

(a)   (b)
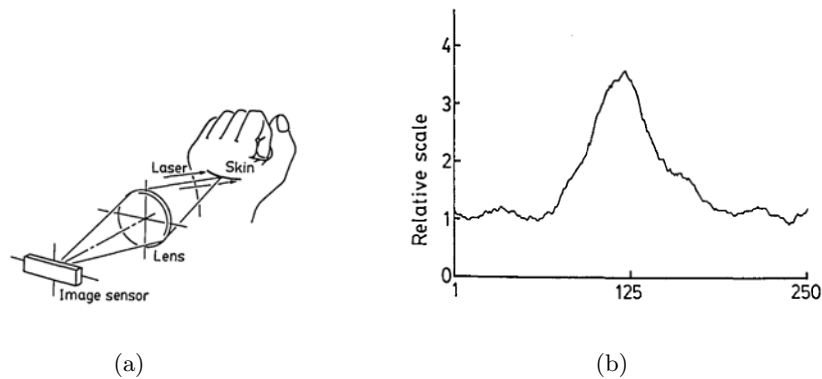
Figure I.12: (a) Optical arrangement for in-vivo microcirculation measurement using LSV (b) Increase of CCD-recorded signal on the scar area [8, 9].

Time-varying speckle is based on the evaluation of temporal statistics

24

of speckle fluctuations at a single point. On its basic configuration, a collimated laser beam illuminates a small area in the flow. Light from all points within this area interferes in the image plane and forms the speckle pattern. When the scatterers move, individual speckles at a fixed position fluctuate. The frequency spectrum of these fluctuations can be related to velocity information.

Most of LSP applications belong to the biomedical field [8, 9, 119–124]. An example of in-vivo blood flow measurement using time varying speckle is presented in Fig. I.4.2 and I.4.2.

I.5 Dual-slit technique (DS)

The Dual-Slit technique was discovered at the same period than LDV and LSP, and demonstrated good results for flow measurement in microchannels smaller 80 µm. On-line determination of blood flow velocity by DS is based on a direct measurement of time delay between recognizable peaks, acquired by two photodetectors separated from a known distance.

I.5.1 History

The Dual-Slit (DS) technique, first refereed as "Photometric double-slit technique", [125], is based on the measurement of the travel time over a known distance of a group of particles. In its original version, the dual-slit technique was restricted to capillary vessels, where individual Red Blood Cells (RCBs) or trains of RBCs are circulating in single file, at the same velocity, which can be then straightforwardly measured by temporal correlation.

A standard set-up for DS technique is described in Fig. I.13. The channel under study is trans-illuminated and two photo-sensors (slits) are positioned, separated by a known distance, L_s, along the channel axis (Fig. I.13). The slits are regions of interest on images of particle flows recorded using a high speed video camera. The modulation of light, produced by the passage of the particles flowing through the channel, is deduced by performing the sum of grey levels in both slits at each time step. For various distances L_s between the two slits, a cross-correlation velocity, $V_{ds} = L_s/T_d$, is obtained, where T_d is the time delay for which the cross-correlation between the two signals is maximum. For an optimal L_s, the final velocity at a given point represents the maximal velocity in depth. Finally, the slits are successively moved across the channel to obtain a profile of particle maximal velocities [126–129].
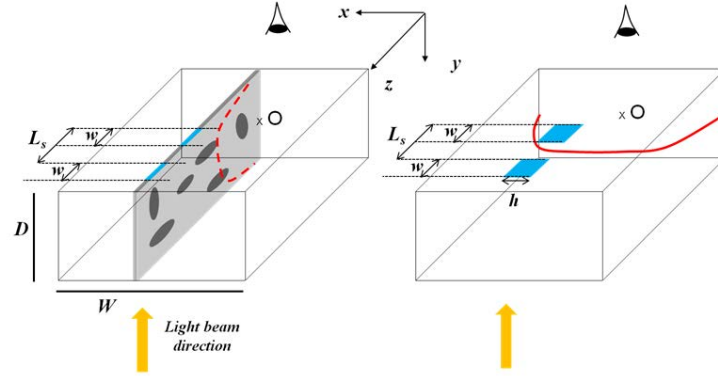
Figure I.13: Scheme of the dual-slit methodology implementation for in vitro experimentation

I.5.2 Recent advances

In case of steady-state flow, velocity profiles have been successfully reconstructed in a flow-channel of 10x10 μm, with a spatial resolution of 300 nm [130, 131]. However, this technique requires expensive equipment (high speed camera) and the related data-treatment is time consuming. Moreover, the duration of the acquisition is long (typically 2 to 40s). For these reasons, on-line measurements in cases of transient regimes are not possible.

I.6 Optical feedback Interferometry (OFI)

Optical feedback interferometry (OFI) or Self-mixing interferometry occurs when a laser is beaming onto a target (such as particles embedded in a liquid phase), and some light reflected by the target re-enters into the laser cavity. This additional light modulates the laser, and the modulation is a function of the velocity of the target. OFI principle is close to LDV, unlike the fact that the interferences occur in an active medium (the laser cavity) instead of freespace, leading to some non-linear effects. However, an OFI setup is much simpler as no double beams must be aligned and no extra detector is necessary. An enhanced description of this physical phenomenon is proposed in Chapter II.
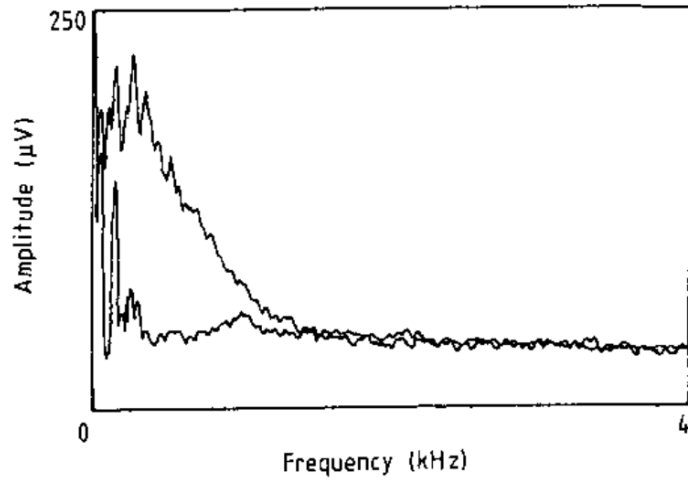
Figure I.14: Multiple scattering effect in OFI for blood flow measurement: the upper spectrum is the signal spectrum, the lower spectrum is the noise spectrum [10].
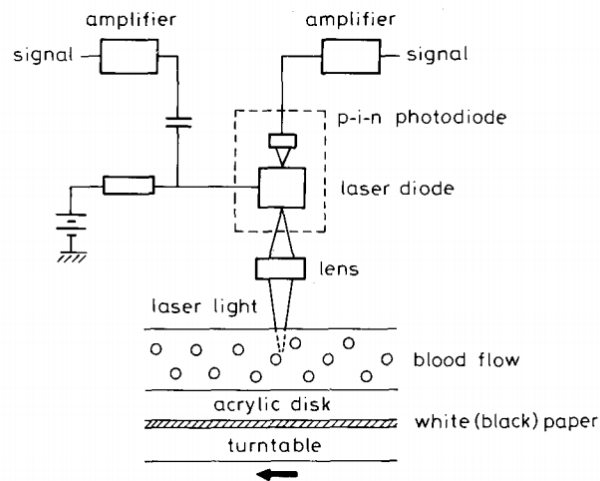
Figure I.15: Scheme of an early optical feedback interferometry sensor for blood flow measurement [11]

I.6.1 History : Blood flow measurement

Although self-mixing effect has been discovered in the 60's, its application to fluid flow measurement was first demonstrated by Koelink et al. in 1992, as they tried to measure the flow rate of rabbit's blood flowing in a circular duct [132]. OFI first experimental set-up for flow measurement was made of a single-mode laser diode coupled into a glass optical fiber using a microscope objective. The built-in photodiode was used to acquire the OFI signal. It was then amplified and converted in frequency domain through a FFT transform function. Nevertheless, the first OFI configuration for flow measurement suffered from several drawbacks. First, the measurement was invasive, insofar as an optical fiber containing the probe was inserted into the flowchannel. In addition, the probe disturbed the flow, leading to measurement errors [133]. Finally, OFI suffered from multiple scattering effect, as the sensor was calibrated on a channel filled with non-diluted blood, using red blood cells as tracking particles. As a matter of fact, for blood flow measurement, multiple scattering effect occurs, i.e. a photon is not reflected by a single particle in the flow, but suffers from multiple reflection before being re-injected into the laser cavity. In this case, the OFI spectrum did not show one Doppler peak as for a solid target, but a whole spectrum of frequencies (Fig. I.14). Because Koelink et al. had observed previously the same effect for in-vivo LDV measurement [134], they applied the same signal processing method to recover the blood flow rate. A linear relationship was demonstrated between the first moment spectrum and the liquid's flow rate. They also proposed another signal processing method, which consists in measuring the cut-off frequency (defined as the frequency where the signal spectrum reach the noise of the spectrum obtained with zero velocity) and in relating it with the theoretical Doppler frequency.

In 1992, the same research team removed the fiber and used directly the laser diode as a probe. The experimental set-up is depicted in Fig. I.15. They measured the flow of polystyrenes beads embedded in water, retrieving a well-defined Doppler peak in the OFI signal that varies linearly with the flow rate. Finally, some measurements were obtained by focusing the laser diode directly on the fingertip, and the heart beat frequency was retrieved [10, 135].

I.6.2 OFI in LDV configuration

OFI sensor for fluid flow measurement was put aside until 2000, when Hast et al. exploited OFI for various applications in biomedical optics such as pulse wave velocity measurement, shape measurements and blood pressure regulation [136–140].

Zakian and Dickinson offered a great contribution to the development of
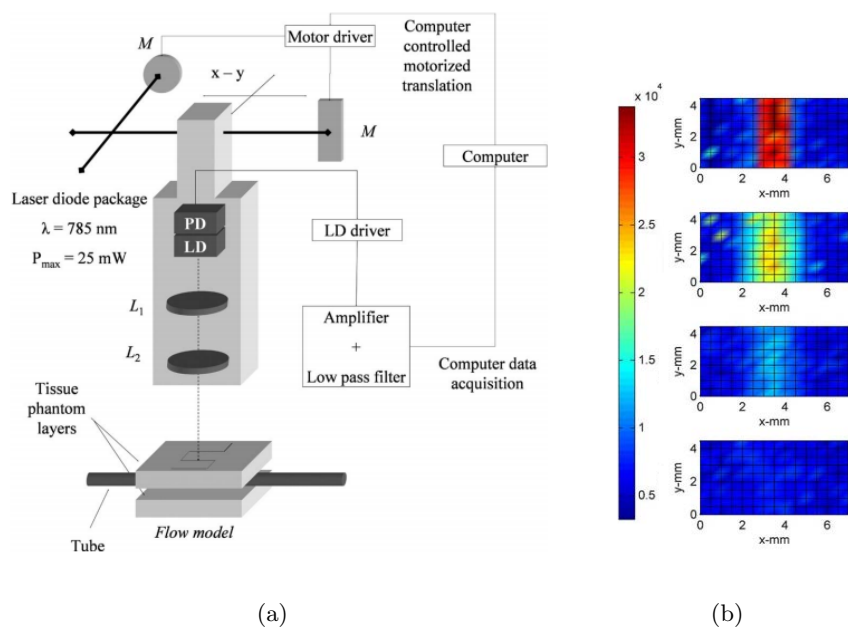
Figure I.16: (a) OFI experimental set-up for microfluidic flow imaging (b) Flow map for several width of skin-like layer ([0, 0.42 mm, 0.70 mm, 1.19 mm]); The flow rate was set at 50 mL/h and the laser diode operated at 785 nm [12]

experimental understanding of OFI flowmetry. They studied the influence of the size of the particle used as trackers, and took an interest in measuring fluid flow in narrow channels [141, 142]. Particle sizing experiment were performed by using polystyrenes spheres with diameter varying from 0.02 to 0.2 μm in a laminar flow. The size of the particles could be retrieved after calibration by quantifying the broadening of the OFI spectrum fitted with a Lorentzian function through the half-width at half-maximum (HWHM) parameter. The flow rate was also calculated by fitting the OFI spectrum with an exponential function, and by performing a calibration, leading to an analytical relationship between the flow rate and the fitting function parameter. This sensor, which paves the way for OFI in its modern form, is depicted in Fig. I.6.2.

Zakian and Dickinson also investigated the effect of a thin layer of skin between the sensor and a blood vessel by constructing skin phantoms and measuring the blood flow. The results, plotted in Fig. I.6.2 demonstrated the ability to employ OFI sensor for in-vivo blood perfusion monitoring.

I.6.3   OFI technical evolution

In the past three years, an increase of the number of papers published about OFI sensor for blood flow measurement has been noticed, proving that this technology is perfectly suitable for precise flow rate measurement, and shows major advantages over conventional optical sensors:

- Some improvements were made to consolidate **the signal processing in multiple scattering effect**, and to built a low-cost embedded sensors [143, 144].

- The first reconstruction of a velocity distribution in a circular channel of a 12 mm diameter in multiple scattering regime was demonstrated in 2011 by Rovati et al. [145], who built an OFI sensor **based on a low-cost superluminescent diode.**

- Wang et al. explained theoretically the shape of the OFI spectrum when the laser is beaming onto a **flowing Brownian solution** [146, 147]

- Lim et al. proposed a full-field OFI sensor system with simultaneous read-out from **an array of lasers** for measuring fluid-flow velocities [148].

- Kliese et al. measured the flow rate of a solution flowing in a square **100μmx100μm microchannel** [149], and improved the accuracy of flow rate measurement in **very slow flow using a blue laser** [150].

I.6.4 OFI in LSP configuration

During the last decade, Ozdemir et al. developed a flowmeter using the speckle effects in optical feedback for distance and velocity measurement. They recovered the velocity of a target either by counting the number of times the speckle signal intensity passes above a threshold value in a fixed time interval or by measuring the autocorrelation time of the speckle signal. They showed that the optical feedback speckle interferometer is suitable for non-invasive blood flow measurement over the skin, and compared the performance of their sensor over conventional LDV [151–154].

I.7 Comparison and conclusion

I.7.1 Comparison

Table I.7.1 summarizes the methods presented in this chapter, in term of spatial and temporal resolution, cost and simplicity. Each of these three types of optical methods provides accurate flow rate measurement in sub-millimetre channels, but is designed for a specific application.

Optical sensor for velocity measurement in microchannel can be summarized in three main categories:

1. Techniques that employs changes in the light properties induced by diffraction on particles embedded in a flow (Laser Doppler Velocimetry (LDV), time-varying speckle method (LSV) and optical feedback interferometry (OFI)).

2. Techniques based on statistical behaviour of a particular medium (Laser Speckle Contrast imaging (LASCA) and Laser Speckle Velocimetry (LSV)).

3. Techniques using spatial or temporal algorithm to reconstruct particles displacement (Particle Image Velocimetry (PIV or µ-PIV), Particle Tracking Velocimetry (PTV) and Dual-slit method (DS)).

LDV provide high spatial resolution due to a sensing volume defined by the waist of a laser beam. However, as a point-wise technique, the temporal resolution is limited due to the need of mechanical scanning. Furthermore, the need of external optical elements to measure 3-components velocity can increase tragically its cost and simplicity.

On the contrary, LASCA temporal resolution is high, as it is a full-field technique. Some improvement in the spatial resolution can be a useful tool for microfluidics imaging, and blood flow monitoring.

31

PIV and related technique are extensively used in microfluidics. They allow the determination of vectorial velocities with a spatial resolution that is high enough for accurate wall-shear stress measurements. Video rate or high speed imaging enables a satisfying temporal resolution. However, the use of bulky and expensive cameras makes PIV sensors more appropriated for laboratory and research use rather than for industrial applications.

Throughout this thesis, OFI for flow measurement is studied, and will be compared with the existing technologies in the concluding section.

	Method	Spatial resolution (μm)	Cost / Simplicity	In-vivo applications	Advantages	Drawbacks
Pointwise technique	LDV	0.960	Expensive / Simple	Yes	3-velocity components; Real-time visualization; Information on particles size and concentration	Low temporal resolution for large area; Low SNR nearwall; Low resolution in MS regime
	OFI	∼ 10	Low-cost / Simple	Yes	Self-aligned and compact; Can be built in fully integrated devices (array); Real-time visualization; Information on particles size and concentration	Loss of resolution due to multiple scattering regime; Research stage
Full-field technique	μ-PIV PTV	0.0645	Prohibitively expensive / Complex	Under conditions	Extremely high resolution; Coupling with other technique to improve performance	Time and memory consuming; Concentration control; Expensive and bulky elements
	Dual-slit	0.05	Expensive / Complex	Under conditions	Extremly high resolution; Suitable for high particle concentration	2-D velocity component; Research stage
	LASCA	50	Low-cost / Simple	Yes	Single exposure technique; Sensitive to both lateral and line-of-sight motion; High particle concentration	Low spatial resolution; Heavy computation and need of GPU

Table I.1: Comparison of optical methods for flow rate and velocity measurement in microscale devices

I.7.2 Evolution of microfluidics flow sensors in the future
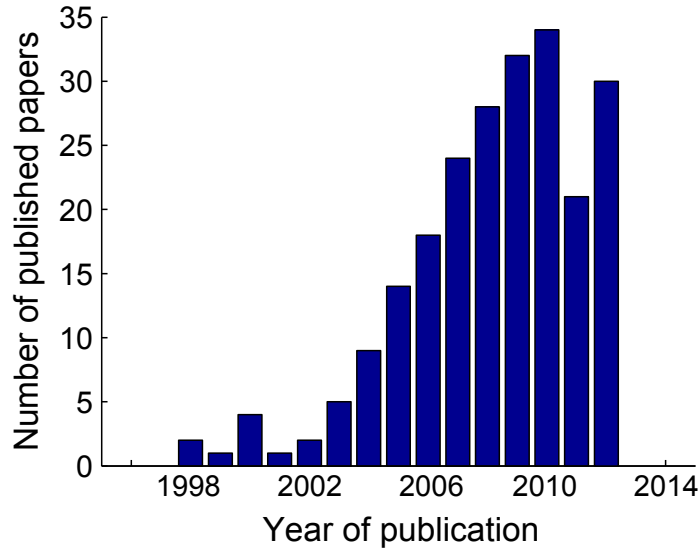
Figure I.17: Number of articles dealing with optical flowmeter for microfluidics applications per year, until November 2012 *(Source : Web of science ©)*

Many applications requires the manipulation of fluid, tending towards always smaller volume handling with precise flow and concentration control.

As of the end of 2012, 195 papers about flow sensors for microfluidics applications have been published according to the Web of Science ©. The number of published papers shows an increasing trend since 1998, when Santiago et al. proposed for the first time the μ-PIV technique to measure fluid flow velocity in micro-channels. The repartition of the number of published papers per year is presented in Fig. I.17. Although this histogram do not provide an exhaustive representation of research dealing with flow control and measurement in microdevices, it gives a good indication about the growing interest for the need of precise flowmeters in the microfluidic field.

Chapter II

Optical Feedback Interferometry: theory and model

II.1 Introduction

When a laser beam illuminates an external target which surface is diffusive or reflective, a small portion of the incident light is reflected back into the laser cavity. This phenomenon, referred as "Optical feedback" or "Self-mixing effect", occurs in most laser-based systems. It was first seen as an inconvenience because it affects seriously the laser properties, leading to unwanted perturbations. Optical isolators are commonly used to prevent the laser diode from this parasitic light.

Nevertheless, it was promptly found that this backscattered light could be exploited for many sensing applications. The potential of optical feedback was first demonstrated in 1962 by Kleinman and Kisliuk [155]. As multimode devices, Masers (Microwave Amplification by Stimulated Emission of Radiation) suffered from the excitation of many modes at the same time, generating unwanted noise effects, affecting stability and modifying the device's performances. Kleinman and Kisliuk suggested adding another reflecting plate outside the Maser. They found out that the presence of an external reflector can affect the losses of the unwanted modes, and therefore allows an artificial selection of the lasing mode. The same effect was demonstrated later using a He-Ne laser [156], and a semiconductor laser diode [157–159]. It was also experimentally found that optical feedback affects various laser properties, such as the carrier density at the threshold [160] and the laser dynamical properties [161]. Furthermore, theses changes were dependent among others on the distance between the laser cavity and the external reflector [162], and on the strength of the coupling between the reflected wave and the in-cavity wave [163].

Despite these experimental observations, there was no theoretical model that could accurately describe the origins of the dynamical operation of semiconductor lasers with optical feedback. In 1980, Lang and Kobayashi [164] presented a work showing that the dynamical changes in the carrier density of the semiconductor laser due to optical feedback lead to a modification of the refractive index, which in turn alters the resonant frequency of the laser. They also demonstrated that this information could be used to describe the dynamical behaviour of the laser's output power with optical feedback. Most of the theoretical models presented in the literature are based on the Lang-Kobayashi equations [165–167].
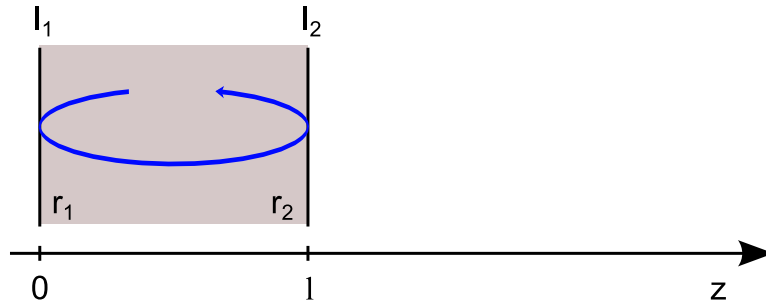
Figure II.1: Schematic arrangement of a laser diode without optical feedback.

II.2 Optical feedback interferometry: Theory

II.2.1 The laser diode in free space

The optical feedback effect can be explained by firstly considering the operation of a standalone laser. A schematic arrangement for a free running state laser diode can be represented by a two-facet Fabry-Perot cavity delimiting an active layer of length l_c. These facets (I1 and I2) are defined by their reflection coefficients r_1 and r_2 with respect to the electric field amplitude. This schematic arrangement is shown on Fig. II.1.

To describe the behavior of the laser cavity, an electromagnetic wave travelling in the z-direction along the longitudinal dimension of the cavity is considered. The electric field in the cavity can be written as:

$$E(z) = E_0 \exp\left(-jk_0 z\right) \exp\left(-\frac{1}{2}\gamma_0 z\right) \tag{II.1}$$

Considering:

$$k_0 = \frac{2\pi n_0 \nu_0}{c} \quad \text{the wavenumber} \tag{II.2}$$

$$\gamma_0 = \alpha_p - g \quad \text{the absorption gain coefficient of the medium} \tag{II.3}$$

Where n_0 represents the refractive index in the active medium, ν_0 the angular frequency of the wave and c the speed of light in vacuum. The material in the laser cavity has a power gain g and a power loss α_p.

The lasing threshold is reached when the optical gain of the laser medium is exactly balanced by the sum of all the losses experienced by the light in one round trip in the laser's optical cavity. To determine this condition, an electromagnetic wave $E(0)$ injected through the facet I_1 and a round trip travel inside the cavity is considered.

The propagation equation can be written:

$$E(0) = E(0) * r_1 e^{(-jk_0 l_c)} e^{(-\frac{1}{2}\gamma_0 l_c))} * r_2 e^{(jk_0(-l_c))} e^{(\frac{1}{2}\gamma_0(-l_c)))} \qquad \text{(II.4)}$$

yielding,

$$\boxed{1 = r_1 r_2 e^{(-2jk_0 l_c)} e^{(-\gamma_0 l_c))}} \qquad \text{(II.5)}$$

Solving equation Eq. (II.5) and differentiating modulus and phase leads to the laser allowed gain and emitting frequency(ies) equations.

$$
\begin{aligned}
\Re(\text{II.5}) &\Rightarrow r_1 r_2 e^{-\gamma_0 l} = 1 \\
&\Rightarrow g_{\text{th}} = \alpha - \frac{1}{l_c} \ln\left(|r_1 r_2|\right) \qquad \text{(II.6)}
\end{aligned}
$$

$$
\begin{aligned}
\Im(\text{II.5}) &\Rightarrow 2k_0 l_c = 0[2\pi] \\
&\Rightarrow \nu_0 = k * \frac{c}{2l_c n_0} \qquad k \in \mathbb{N} \qquad \text{(II.7)}
\end{aligned}
$$

The lasing conditions of a laser emitting in free space are defined by:

$$
\boxed{
\begin{aligned}
g_{\text{th}} &= \alpha - \frac{1}{l_c} \ln\left(|r_1 r_2|\right) \\
\nu_0 &= k * \frac{c}{2l_c n_0} \qquad k \in \mathbb{N}
\end{aligned}
}
\qquad \text{(II.8)}
$$

These conditions are often referred to as the threshold conditions for lasing. The cavity of the laser can be designed so that only one wavelength can oscillate. Such a laser is known as a single mode laser, which is commonly used in many interferometric sensing systems. The theory developed in the rest of this chapter is considering this type of laser only.

II.2.2 The laser diode under optical feedback

An equivalent model of the laser diode subject to feedback due to the presence of an external target at a distance l_{ext} smaller than the half-coherence length of the optical source is described on Fig. II.2. This three-mirror cavity can be modeled using a single equivalent cavity limited by I_1 and I_{eq}, an equivalent mirror with a reflection coefficient r_{eq} (Fig. II.3).

As previously, an electromagnetic wave doing a round trip travel inside the three-mirror cavity is considered. The electromagnetic field can be split into two parts. A part of the electric field travels along the same path inside the laser cavity than the field without optical feedback, (blue term in
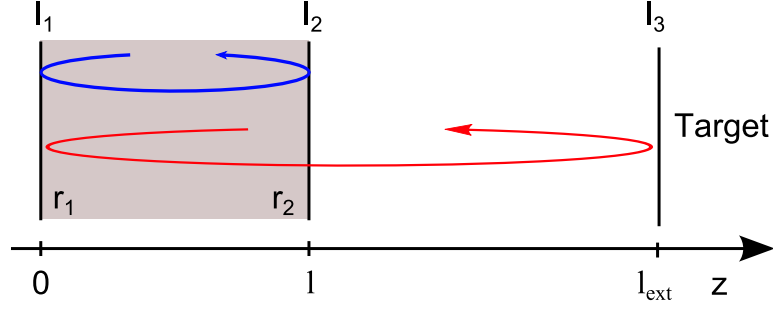
Figure II.2: Schematic arrangement for a LD under optical feedback, known as the three-mirrors cavity configuration.

Eq. (II.9)). The other part propagates outside the laser cavity, and gets reflected on the target I_3 (red term in Eq. (II.9)). The two paths are depicted in Fig. II.2. The wavenumber k_{in} (k_{ext}) and the absorption coefficient γ_{in} (γ_{ext}) refer to the wave travelling inside (respectively outside) the laser cavity.

The propagating equation becomes:

$$E(0) = E(0) * r_1 r_2 e^{(-2jk_{in}l_c)} e^{(-\gamma_{in}l_c))} + E(0) * r_1(1 - r_2^2) r_{ext} e^{(-2jk_{ext}l_{ext})} \tag{II.9}$$

where $r_{ext} = a \cdot f \cdot r_3$, with r_3 the reflection coefficient on the target, a the attenuation of the reflected electric field, and f the fraction of the reflected field that couples with the lasing mode [168].

Yielding,

$$1 = r_1 r_2 e^{(-2jk_{in}l)} e^{(-\gamma_{in}l))} \left[1 + \frac{r_{ext}}{r_2} (1 - r_2^2) e^{-2jk_{ext}l_{ext}} \right] \tag{II.10}$$

It should be noted that Eq. II.10 only considers a single round-trip in the external cavity, which is valid for most applications.

Considering the following notation: $\zeta = \frac{r_{ext}}{r_2}(1 - r_2^2)$.

$$1 = r_1 r_2 e^{(-2jk_{in}l)} e^{(-\gamma_{in}l))} \left[1 + \zeta e^{-2jk_{ext}l_{ext}} \right] \tag{II.11}$$

II.2.2.a   Modulation of the laser optical frequency

Identifying the terms in (II.11) and (II.5) highlights the fact that the field reflected from I_2 and the field injected into the laser from the external cavity

39
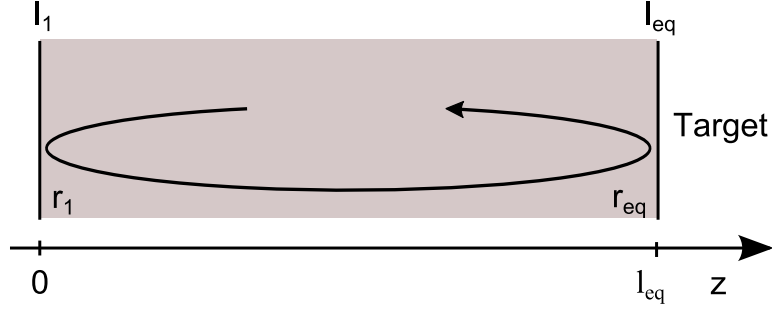
Figure II.3: Equivalent cavity model.

can be combined into a single term. This allows the laser facet I_2 and the target I_3 to be combined into a single equivalent mirror I_{eq} as shown in Fig. II.3. The equivalent interface has a reflection coefficient r_{eq} defined by [169]:

$$r_{eq} = ||r_{eq}||e^{j\Phi_{eq}} = r_2\left[1 + \zeta e^{-2jk_{ext}l_{ext}}\right] \qquad (II.12)$$

With

$$||r_{eq}|| = r_2\left[1 + \zeta\cos(2k_{ext}l_{ext})\right] \qquad (II.13)$$
$$\Phi_{eq} \sim -\zeta\sin(2k_{ext}l_{ext}) \qquad (II.14)$$

For a laser in the presence of an external target, the lasing condition becomes:

$$r_1 r_{eq} e^{-2jk_F l_c} e^{\gamma_F l_c} = 1 \qquad (II.15)$$

By rearranging equation (II.15) from the similar equation for the standalone laser (II.5):

$$\frac{(II.15)}{(II.5)} \Leftrightarrow \frac{r_{eq}}{r_2}e^{-(\gamma_F - \gamma_0)l_c}e^{-j(\Phi_F - \Phi_0)} = 1 \qquad (II.16)$$

With

$$\Phi_F = 2jk_F l_c \qquad (II.17)$$
$$\Phi_0 = 2jk_0 l_c \qquad (II.18)$$

Yielding,

$$\left[||\frac{r_{eq}}{r_2}||e^{-(\gamma_F - \gamma_0)l_c}\right]e^{-j(\Phi_F - \Phi_0 - \Phi_{eq})} = 1 \qquad (II.19)$$

The threshold gain can be found by equalizing the real part of Eq. (II.19).

40

$$g_{thF} - g_{th0} = -\frac{\zeta}{l_c} \cos\left(2k_{\text{ext}}l_{\text{ext}}\right) \qquad \text{(II.20)}$$

Likewise, the change in the round-trip phase due to optical feedback $\Delta\Phi$ is calculated:

$$
\begin{aligned}
\Delta\Phi &= 2l_c(k_F - k_0) + \zeta \sin\left(2k_{\text{ext}}l_{\text{ext}}\right) \\
&= \frac{4\pi l_c}{c}\left(n_F\nu_F - n_0\nu_0\right) + \zeta \sin\left(2k_{\text{ext}}l_{\text{ext}}\right) \qquad \text{(II.21)}
\end{aligned}
$$

By definition, $n_F\nu_F - n_0\nu_0 = \Delta(n\nu) = \nu_0\Delta n + n_F\Delta\nu$,
The change in the effective index n may be expressed as:

$$\Delta n = \frac{\partial n}{\partial g}(g - g_0) + \frac{\partial n}{\partial \nu}(\nu - \nu_0) \qquad \text{(II.22)}$$

Considering the linewidth enhancement factor $\alpha = \frac{-4\pi\nu_0}{c}\frac{\partial n}{\partial g}$ [170], Eq. (II.22) can be rewritten using (II.20):

$$
\begin{aligned}
\Delta(n.\nu) &= \nu_0\left[\frac{-\alpha c}{4\pi\nu_0}(g_F - g_0) + \frac{\partial n}{\partial \nu}(\nu_F - \nu_0)\right] + n_F(\nu_F - \nu_0) \\
&= (\nu_F - \nu_0)\left[\nu_0\frac{\partial n}{\partial \nu} + n_F\right] - \frac{\alpha c}{4\pi\nu_0}(g_F - g_0) \\
&= (\nu_F - \nu_0)\overline{n_0} + \frac{\alpha c}{4\pi l}\zeta \cos\left(2k_{\text{ext}}l_{\text{ext}}\right) \qquad \text{(II.23)}
\end{aligned}
$$

The term $\overline{n_0} = \nu_0\frac{\partial n}{\partial \nu} + n_F$ stands for the effective group refractive index, which takes into account the dispersion of the refractive index and is used to evaluate the spacing between adjacent emission frequencies [171].

These modifications affect (II.21), leading to:

$$\Delta\Phi = \nu_F - \nu_0 + \zeta\frac{c}{4\pi l\overline{n_0}}\sqrt{1 + \alpha^2}\sin\left(2k_{\text{ext}}l_{\text{ext}} + \arctan(\alpha)\right) \qquad \text{(II.24)}$$

Let C be defined by:

$$C = \zeta\frac{\tau_d}{\tau_l}\sqrt{1 + \alpha^2} \qquad \text{(II.25)}$$

where $\tau_d = \frac{2l_{\text{ext}}}{c}$ is the time of flight in the external cavity, $\tau_l = \frac{2l\overline{n_0}}{c}$ the time of flight in the laser cavity.

C is the feedback parameter, which describes the strength of the changes due to optical feedback in changing the intrinsic behaviour of the laser [172]. Since the round-trip phase within the laser cavity must be equal to an integer

41
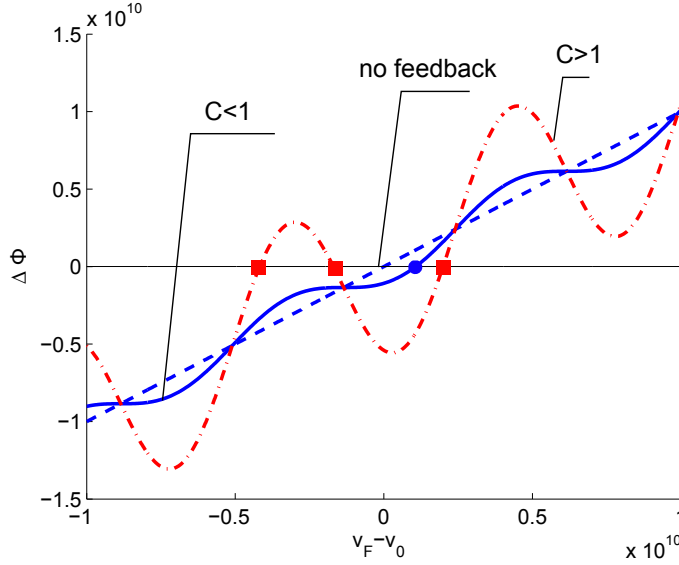
Figure II.4: Solution of Eq. II.26 for $C < 1$ (solid line) and $C > 1$ (dot-dashed line). The square marker represents the only solution for $C < 1$ and circles markers indicate that multiple solutions exist for $C > 1$

multiple of 2π, the emission frequencies are obtained from Eq. (II.24) for $\Delta\Phi = 0$ (or multiples of 2π). The phase condition of a laser under feedback can be written:

$$\nu_F - \nu_0 = \frac{C}{2\pi\tau_d} \sin\left(2\pi\nu_F\tau_d + \arctan(\alpha)\right) \qquad \text{(II.26)}$$

Fig. II.4 shows the round-trip phase change $\Delta\Phi$ as a function of $\nu_F - \nu_0$. Possible emission frequencies, where the phase condition is satisfied, are characterized by $\Delta\Phi = 0$. Without feedback, as represented by the dashed curve, $\Delta\Phi$ varies linearly with $\nu_F - \nu_0$. As long as C is small, $\Delta\Phi$ increases with frequency yielding to a single zero for $\Delta\Phi$, and therefore a single emission frequency. For larger C, several external cavity modes around the emission frequency ν_0 may satisfy the phase equation.

II.2.2.b   Modulation of the laser output power

We now focus on semi-conductor laser diodes (LD). For a description of the optical feedback effect on the optical power, the rate equation of the LD should be considered. The Lang-Kobayashi equations describe the dynamics of a single mode LD under optical feedback [164]:

$$\frac{dE(t)}{dt} = \frac{1}{2}\left[G_n\left(N(t)-N_0\right)-\frac{1}{\tau_p}\right]E(t)$$
$$+\frac{\zeta}{\tau_l}E(t-\tau_d)\cos\left[\omega_0\tau_d+\Phi(t)-\Phi(t-\tau_d)\right] \quad \text{(II.27)}$$

$$\frac{d\Phi(t)}{dt} = \frac{1}{2}\alpha G_n\left(N(t)-N_{\text{th}}\right)$$
$$-\frac{\zeta}{\tau_l}\frac{E(t-\tau_d)}{E(t)}\sin\left[\omega_0\tau_d+\Phi(t)-\Phi(t-\tau_d)\right] \quad \text{(II.28)}$$

$$\frac{dN(t)}{dt} = G_{\text{gen}}-\frac{N(t)}{\tau_e}-G_n\left[N(t)-N_0\right]E^2(t) \quad \text{(II.29)}$$

The parameters involved in theses equations are described in Table II.1.

$E(t)$	Envelop of the electric field, normalized so that E^2 corresponds to the photon density S (m^{-3})
$\Phi(t)$	Electric field phase
ω_0	Angular frequency of the LD without feedback ($\omega_0 = 2\pi\nu_0$)
G_n	Modal gain coefficient
$N(t)$	Spatially averaged carrier density
N_0	Carrier density at transparency
N_{th}	Carrier density at threshold
τ_p	Photon lifetime within the cavity
τ_e	Carrier lifetime
τ_l	LD cavity round-trip time
τ_d	External cavity round-trip time
G_{gen}	Electric pumping coefficient, defined by $G_{\text{gen}} = \frac{J\eta}{qd}$ with J the injection current density, η the internal quantum efficiency, d the active layer thickness and q the elementary charge.
α	Linewidth enhancement factor [170]
ζ	Fraction of the back-reflected field that couple with the lasing mode (Eq. (II.25))

Table II.1: Description of parameter used in Eq. (II.27)

Stationary solutions of the Lang-Kobayashi equations allow to write an approximated expression of the optical power of a LD under optical feedback.

The left part of the set of equations (II.27) becomes:

$$\frac{dE(t)}{dt} = \frac{dN(t)}{dt} = 0 \quad \text{(II.30)}$$
$$\frac{d\Phi(t)}{dt} = 2\pi\left(\nu_F-\nu_0\right) \quad \text{(II.31)}$$

The field equation without feedback is:

$$\frac{dE(t)}{dt} = \frac{1}{2}\left[G_n\left(N(t) - N_0\right) - \frac{1}{\tau_p}\right]E(t) \qquad \text{(II.32)}$$

From the stationary solution of this equation, it can be deduced that:

$$\frac{1}{\tau_p} = G_n\left(N_{\text{th}} - N_0\right) \qquad \text{(II.33)}$$

Furthermore, the electric field with delay $E(t - \tau_d)$ can be seen as a small variation of the electric field without delay $E(t)$, and therefore can be written:

$$E(t - \tau_d) = E(t) - \tau_d\frac{dE(t)}{dt} = E(t) \qquad \text{(II.34)}$$

Rewriting the first dynamical equation highlights the fact that optical feedback induces carrier density modulation inside the LD cavity, N_F indicating the presence of optical feedback:

$$N_F(\tau) = N_{\text{th}} - \frac{2\zeta}{G_n\tau_l}\cos(2\pi\nu_F\tau_d) \qquad \text{(II.35)}$$

Doing the same manipulation with the phase equation yields:

$$\nu_F - \nu_0 = \frac{\zeta}{2\pi\tau_l}\left[\alpha\cos(2\pi\nu_F\tau_d) + \sin(2\pi\nu_F\tau_d)\right] \qquad \text{(II.36)}$$

The zero round trip phase condition demonstrated previously is retrieved.

To determine the shape of the emitted optical feedback of a LD modulated by the optical feedback, Eq. (II.35) is substituted into the carrier density equation, obtaining:

$$\begin{aligned}
P \propto E_F^2(\tau) &= \frac{G_{\text{gen}} - N_F(\tau_d)/\tau_e}{G_n\left[N_F(\tau_d) - N_0\right]} \\[2mm]
&= \left(\frac{\tau_p}{\tau_e}\right)\frac{G_{\text{gen}}\tau_e - N_{\text{th}} + \frac{2\zeta}{G_n\tau_l}\cos\left[2\pi\nu_F\tau_d\right]}{1 - \frac{2\zeta\tau_p}{\tau_l}\cos\left[2\pi\nu_F\tau_d\right]} \qquad \text{(II.37)}
\end{aligned}$$

where E_F indicates that the solution is calculated in the presence of feedback. This expression can be linearized, as $\zeta \ll \tau_l/2\tau_p$ for most of the sensing applications where OFI is employed, yielding:

$$\begin{aligned}
P \propto E_F^2(\tau) &\approx \left(\frac{\tau_p}{\tau_e}\right)\left(G_{\text{gen}}\tau_e - N_{\text{th}} + \frac{2\zeta}{G_n\tau_l}\cos\left[2\pi\nu_F\tau_d\right]\right)\left(1 + \frac{2\zeta\tau_p}{\tau_l}\cos\left[2\pi\nu_F\tau_d\right]\right) \\[2mm]
&\approx \left(\frac{\tau_p}{\tau_e}\right)\left(G_{\text{gen}}\tau_e - N_{\text{th}}\right)\left(1 + \frac{2\zeta\tau_p}{\tau_l}\cos\left[2\pi\nu_F\tau_d\right]\right) \qquad \text{(II.38)}
\end{aligned}$$
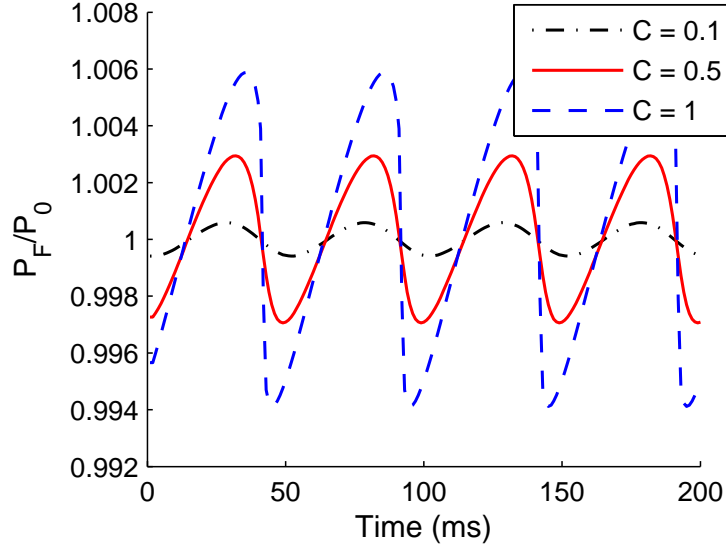
Figure II.5: OFI signal for $C = 0.1$ (dotted-dashed curve), $C = 0.5$ (solid curve) and $C = 1$ (dashed curve). The emitted optical power modulation is proportional to the coupling factor, i.e. to the fraction of back-reflected field that couples with the lasing mode

As the power emitted in the absence of feedback is given by:

$$P_0 \propto E_0^2 = \tau_p \left(G_{\text{gen}} \tau_e - N_{\text{th}} / \tau_e \right) \tag{II.39}$$

We can write the expression of the optical emitted power of a LD under feedback as:

$$\boxed{P_F = P_0 \left[1 + m \cos(2\pi \nu_F \tau_d) \right]} \tag{II.40}$$

With m the modulation index defined by:

$$m = C \frac{2 \tau_p c}{L \sqrt{(1 + \alpha^2)}} \tag{II.41}$$

The OFI signal is plotted for three values of C on Fig. II.5. The emitted optical power modulation is proportional to m, so by definition is also proportional to C. An enhanced description of the influence of C on the shape of the output power is detailed in [173].

II.2.2.c   Effect on the laser diode voltage

In practice, the laser output power is measured using the internal monitor photodiode, but the laser junction voltage is affected by optical feedback.

The change in laser junction voltage ΔV can be related to the coupling coefficient of the external cavity and therefore to the level of feedback and the location of the target [174, 175]:

$$\Delta V = \frac{-4kTN_F\zeta}{g_F q N_0 \tau_l} \cos(2\pi\nu_F\tau_d) \qquad (II.42)$$

Where k is the Boltzmann constant, q the elementary charge and T the temperature.

According to Eq. II.40, output power varies proportionally with the change in target location while Eq. II.42 exhibits an inverse relationship. The two quantities are out of phase, and an increase in laser power coincides with a decrease in laser junction voltage. However, the performance of voltage sensing is lower in term of signal-to-noise ratio to that of conventional photocurrent sensing scheme [176], but the the simplicity of the voltage-based sensor shows clear practical advantage.

II.3 Practical application of OFI: Velocimetry

In parallel to the first experimental observations, it appeared that the optical feedback effect could be used for sensing applications, such as displacement measurements [174, 177–194] and laser range finding [195–210].

Optical feedback for measuring velocities has been first demonstrated by Rudd et al. with a He-Ne Laser [211]. In 1986, Shinohara et al. [212] demonstrated the same principle on a semiconductor laser, proving that the traditional Doppler configuration can be reproduced using the optical feedback effect of the laser Diode. In their experiment, light scattered from a rotating target is shifted in frequency by the Doppler effect. The light reflected by the target mixes with the initial light, causing optical interferences inside the laser cavity. By analyzing in the frequency domain the signal from the control photodiode of the LD or directly from the laser junction voltage, the velocity of the target can be calculated. Similarly to the displacement measurement, the asymmetry of the photodetected current for moderate feedback allows recovery of the motion direction [178].

The physical interpretation of this velocity measurement was probably more straightforward compared to signal analysis for distance or displacement measurement, because the signal can be directly interpreted as being the result of interferences within the LD cavity. The experimental set-up is schematically described in Fig. II.6. For a target moving at constant velocity V_T along the optical axis, the OFI signal can be written:
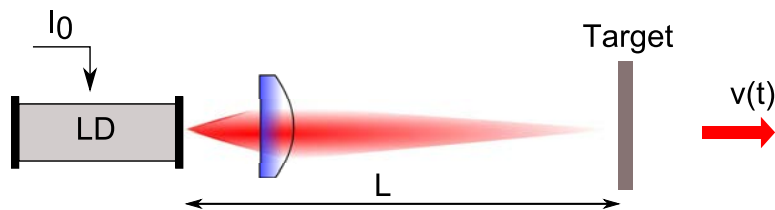
Figure II.6: Schematic arrangement for a OFI velocimeter. The LD is driven by a constant current, and the target is moving along the optical axis.

$$P_F = P_0 \left[1 + \cos\left(2\pi \frac{2(L + V_T t)}{c} \right) \right] \tag{II.43}$$

L being the distance between the target and the LD. A target moving toward or forward the LD can be interpreted as a change in the external cavity length.

In time domain, the fringe period corresponds to a target displacement of $\lambda/2$, and the number of fringes occurring during a known observation time is used to calculate the velocity value. The photodetected current can also be analyzed in the frequency domain and a well-defined peak appears. The peak frequency f_D is related to the target velocity V_T with the following relationship:

$$f_D = \frac{2V_T}{\lambda} \tag{II.44}$$

Where λ is the LD wavelength.

Velocimeters using optical feedback on semiconductor laser diode has been also massively studied [181, 196, 197, 213–223].

In interferometric systems, the illumination and collection beams spatially overlap. Assuming that the laser operates in the fundamental Gaussian mode, the measurement volume centred around the focal point, is defined as the volume within which the optical field has a magnitude higher than $1/e^2$ of the field peak value [224]. Thus, when a laser beam is focused on a target moving monotically along the optical axis (towards or away from the laser), the sensing efficiency is limited as soon as the target position exits the sensing volume. In practical applications, as for example rotating or translating targets, the length of the external cavity (i.e. the distance between the target and laser) is fixed, and Eq. (II.43) does not describe accurately this configuration.
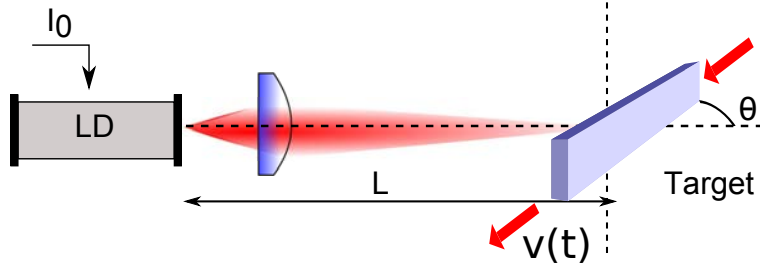
Figure II.7: LD beaming onto a translating target, the distance to the target being fixed

II.4 Optical Feedback velocimetry: a modified compound cavity model

For most of the OFI sensing applications, the three-mirrors cavity (or "compound cavity") model is accurate enough, and describes well the output optical power of a LD suffering from optical feedback.

The expression of P_F demonstrated in Eq. II.40 is:

$$P_F = P_0 \left[1 + m \cos(2\pi\nu_F\tau_d)\right] \qquad \text{(II.45)}$$

According to Eq. II.40, the optical power is modulated when one of these two cases occurs:

- The **length of the equivalent cavity** is modified (displacement or velocity measurement) $(\tau_d(t) \Rightarrow P_F(t))$

- The **optical frequency** is modified (absolute distance measurement) $(\nu_F(t) \Rightarrow P_F(t))$

However, when a LD driven by a DC current is beaming on a translating target at a fixed distance of the laser, the OFI signal exhibits a well defined Doppler peak in the frequency domain f_D, related to the target velocity component in the direction of the laser emission V_A:

$$f_D = \frac{2\,\overrightarrow{k} \cdot \overrightarrow{V_T}}{\lambda} = \frac{2V_T \cos(\theta)}{\lambda} = \frac{2V_A}{\lambda} \qquad \text{(II.46)}$$

where $\overrightarrow{k}$ represents the incident beam direction vector, and θ the angle between the axis of the incident beam and the velocity vector.

In this case, neither the distance to the target nor the laser frequency is modulated.

Therefore, to correctly model the case of rotating or translating targets, we proposed to consider the Doppler shifted light in the expression of the effective reflection coefficient of the equivalent Fabry-Perot cavity (Fig. II.3).

II.4.1 A new expression of the equivalent reflection coefficient

In the initial calculation of the effective reflection coefficient (subsection II.2.2), the exponential factors $e^{j\omega t}$ were not present because they are implicit and common to all terms. However, since the light scattered from the rotating target is shifted in frequency by the Doppler effect, these exponential factors play a major role to take into account the Doppler effect due to V_A in the OFI equations.

By definition, r_{eq} is the ratio of the reflected electric field E_r to the incident electric field E_i on the equivalent interface I_{eq} (Eq. (II.12)).

Let consider:

$$E_i = E_0 \exp j\omega t, \tag{II.47}$$

where E_0 is the incident wave amplitude, and ω the angular frequency of the laser emission.

The variations of ω is slow with respect to the time-of-flight in the external cavity, so ω is considered in a first approximation to be time-independent (i.e. $\omega(t) = \omega(t - \tau_d) = \omega$).

The reflected electric field E_r can be described by the addition of the electric field reflected on the LD front facet E_{r1} and the electric field reflected on the target E_{r2}:

$$
\begin{align}
E_r &= E_{r1} + E_{r2} \tag{II.48} \\
E_{r1} &= r_2 E_i \tag{II.49} \\
E_{r2} &= (1 - r_2^2) r_3 E_0 \exp\left(j \frac{c - V_A}{c + V_A} \omega t + j\Phi_{r2} \right). \tag{II.50}
\end{align}
$$

The expression of the electric field reflected on the target E_{r2} is affected by the Doppler effect, insofar as the angular frequency of the laser emission is shifted by an amount of $\frac{-2V_A}{c+V_A}$. Φ_{r2} represents the phase difference due to the travel of the wave through the external cavity:

$$\Phi_{r2} = 2\pi\nu_F \left(1 + \frac{c - V_A}{c + V_A} \right) \frac{\tau_d}{2} \tag{II.51}$$

where the first term represents the phase difference due to the forward propagating and the second due to the backward propagating wave.

Leading to the following expression:

$$r_{\text{eq}} = \frac{E_{r1} + E_{r2}}{E_i} = r_2 \left[1 + (1 - r_2^2)\frac{r_3}{r_2} \exp j\left(\omega_D t + \Phi_D\right) \right] \qquad \text{(II.52)}$$

With

$$\omega_D = 2\pi\nu_F \frac{-2V_A}{c + V_A} = 2\pi f_D \qquad \text{(II.53)}$$

$$\Phi_D = 2\pi\nu_F \left(1 + \frac{c - V_A}{c + V_A} \right) \frac{\tau_d}{2} = \Phi_{r2} \qquad \text{(II.54)}$$

From Eq. (II.19) and Eq. (III.4), we deduce the emission frequency of the LD under feedback ν_F in function with the optical emission frequency in the free running state ν_0, including the Doppler effect:

$$\nu_F = \nu_0 - \frac{C}{2\pi\tau_d} \sin\left(\omega_D t + \Phi_D + \arctan\alpha\right) \qquad \text{(II.55)}$$

Yielding to the following changes in the expression of the LD optical output power under feedback P_F in function with the optical output power in free running state P_0:

$$P_F = P_0 \left[1 + m\cos\left(\omega_D t + \Phi_D\right) \right] \qquad \text{(II.56)}$$

One can notice that when the target velocity V_T approaches 0, the classical expression of the LD output power demonstrated in the standard model based on rate equations can be retrieved [164]. Furthermore, when the angle θ equals 90°, the target is moving away or towards the laser, and it corresponds to the travelling target configuration demonstrated in subsection II.3.

II.4.2 OFI applied to velocimetry: theoretical analysis

The model describing the output power for an ideal translating target has been simulated and the results are plotted in Fig. II.8. The target and LD simulation parameters are given in Table II.2. Here, the coupling parameter C is 0.3 (weak feedback regime). The OFI signal exhibits a Doppler peak at 17.1 kHz which correspond to the contribution of the target velocity component on the optical axis. Because the signal is not perfectly sinusoidal, some harmonics can be observed. The waveform shows asymmetric sawtooth-like fringes.
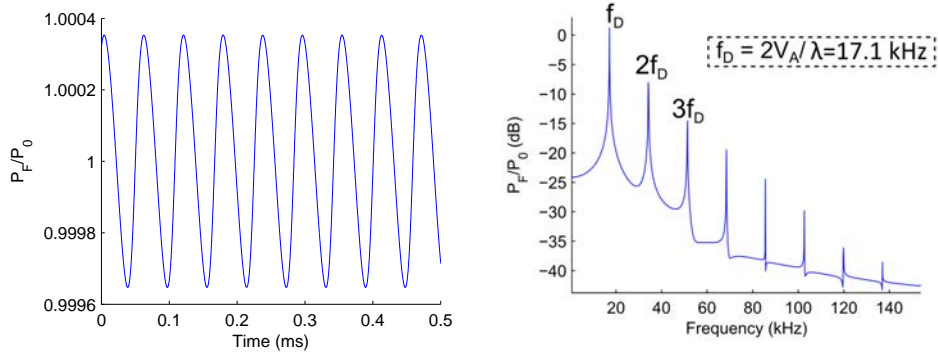
Figure II.8: Simulation of the LD emitted power (Eq. (II.56)) using simulation parameters defined in Table II.2. Left: time domain, Right: frequency domain. The frequency peak corresponds to the theoretical Doppler frequency.

Parameter name	Value
LD wavelength	$\lambda = 850$ nm
Linewidth enhancement factor	$\alpha = 5$
Photon lifetime	$\tau_p = 10^{-12}$ s
LD cavity length	$l = 10$ μm
External cavity length	$L = 10$ cm
Velocity of the target	$V_T = 4$ cm.s^{-1}
Angle between optical axis and velocity direction	$\theta = 80°$

Table II.2: Simulation parameters

51
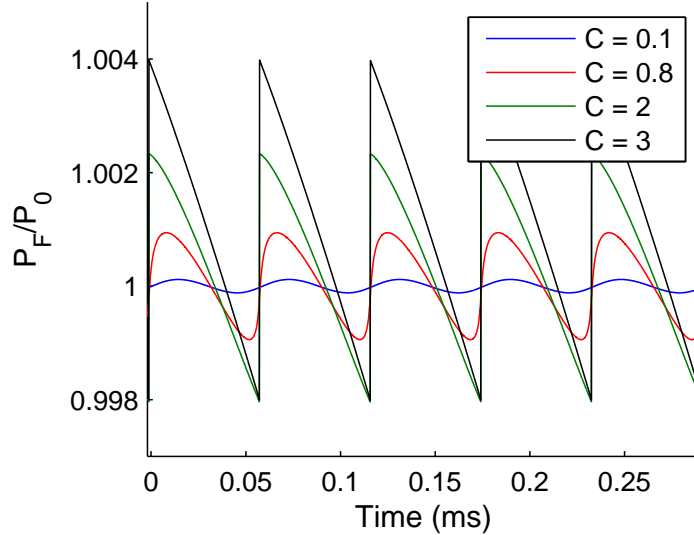
Figure II.9: Simulated emitted power variations for $C = [0.1, \ 0.8, \ 2, \ 3]$.

Moreover, the changes in the output power when the coupling factor C varies are described in Fig. II.9. The output power shape is almost sinusoidal for small C values, and shows asymmetry and hysteresis behavior for $C > 1$.

Finally, an example of waveforms representing velocities of opposite directions is shown in Fig. II.10. Figure II.4.2 illustrates the beat signal waveform obtained for a target moving with a velocity component approaching the laser, and Fig. II.4.2 shows the opposite case. It can be clearly seen that the inclination of the sawtooth-like waveform reverses as the target changes its translation direction.

The classical expression of the optical power of a LD under feedback is retrieved. The cause of the disturbance observed in the reflected electric field is usually described as a change in the external cavity length. However, it is in our opinion more consistent to describe it in term of Doppler effect undergone by the electric field when being reflected on a moving target. This interpretation is more convenient and straightforward to describe OFI when the LD is beaming on particles suspended in a liquid, which is the purpose of this thesis.

II.4.3 Model application: Doppler velocity distribution

In the modified compound cavity model for velocity, every photon scattered from the target was assumed to have the same Doppler shift. In practice, different photons may have a different Doppler shift, because of the finite
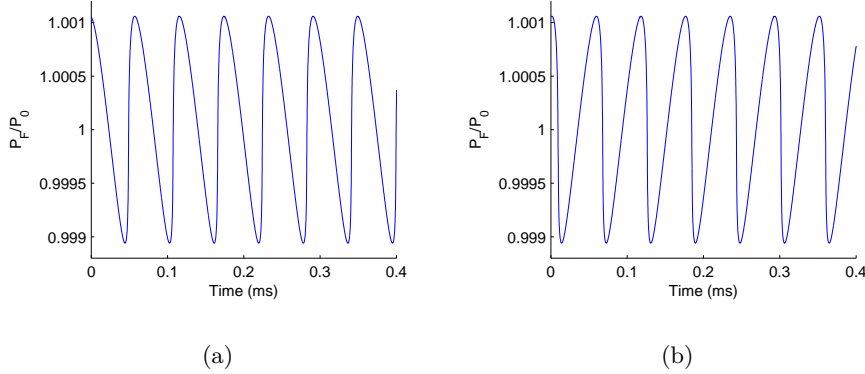
Figure II.10: Output power waveform for $C = 0.9$, when the target is translating (a)"away" $(V_A > 0)$ and (b) "towards" $(V_A < 0)$.

spot size of the laser. It is the case when measuring the velocity of rotating targets. This leads to a distribution of Doppler frequencies in the FFT spectrum of the output power.

To take into account the physical dimension of the laser spot on the target, we also need to consider the power distribution of the laser over the spot area. In our model, we have considered only the simplest case of a single-mode laser emitting a synthetic Gaussian mode. As most of the laser diodes used in the various setup described in this thesis were vertical-cavity surface-emitting lasers (VCSEL) with single mode and circular Gaussian emission, this restricted model is sufficient.

To illustrate the effect of a distribution of Doppler shifts on the laser power, we performed a simulation of a discrete distribution of Doppler shifts for a rotating target (Fig.II.11). The sensing volume is illuminated with a Gaussian function and the velocity distribution follows $v_i = (R + r_i)\Omega$. The signal in time domain exhibits an envelope shape, which is a result of the incoherent superposition of the different Doppler waveforms (Fig. II.4.3). In the frequency domain, there is a distribution of peaks around the Doppler frequency expected for a punctual spot situated at the center of the actual spot. (Fig. II.4.3). Therefore, a velocity distribution leads to an enlargement of the full-width at half-maximum (FWHM) of the frequency peak and a decrease of its amplitude.
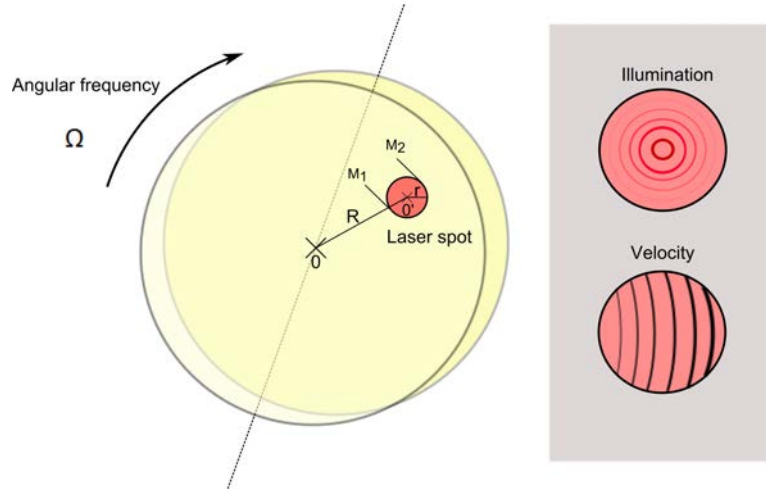
Figure II.11: Illustration of the velocity and reflection coefficient distribution when the laser's spot size is taken into account.

Parameter name	Value
LD wavelength	$\lambda = 850$ nm
Linewidth enhancement factor	$\alpha = 5$
Photon lifetime	$\tau_p = 10^{-12}$ s
LD cavity length	$l = 10\mu$m
External cavity length	$L = 10$ cm
Velocity of the target	$V_T = 4$ mm.s^{-1}
Angle between optical axis and velocity direction	$\theta = 80°$
Coupling factor	$C = 0.2$
spot size radius	$R = 500\mu$m

Table II.3: Simulation parameters: target in translation
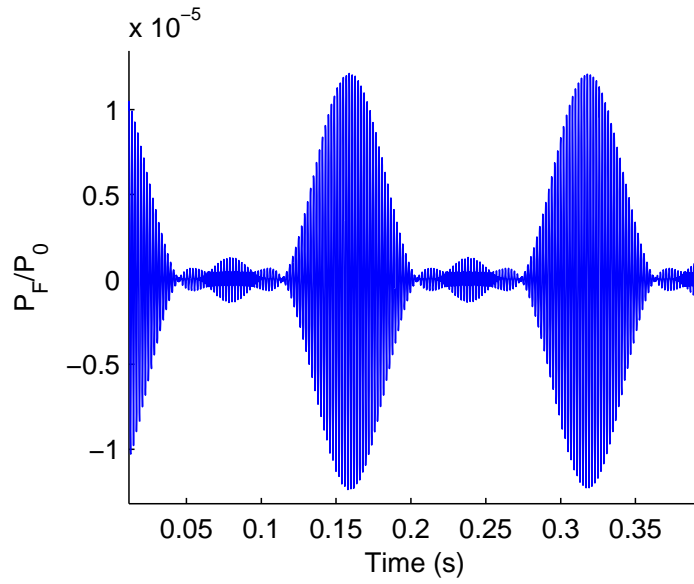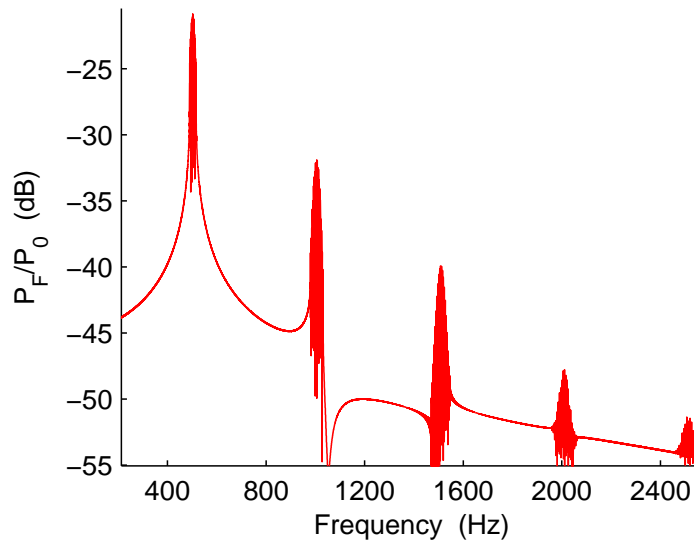
Figure II.12: Output power waveform for a distribution of velocity. (a) Time domain signal (b) Frequency domain

II.5   Direction discrimination

OFI was used to measure velocities when the light is backscattered by a fixed object moving with a component "towards" or "away" from the direction of the laser beam. Thus, OFI signal exhibits a Doppler shift in frequency domain that can be measured by the FFT method to calculate the velocity of a target [212, 223]. However, the OFI spectrum do not provide information about the direction of displacement of the target, because the Doppler signal gives only the absolute value of the difference in frequency between the incident and scattered wave.

Let look in detail at the case of a translating target as shown in Fig. II.7. Depending on the sens of rotation, the projection of the velocity vector on the optical axis is either positive or negative.

The effect of the optical feedback on the LD emitted power is simulated using Eq. (II.56) with the parameters in Table II.3.
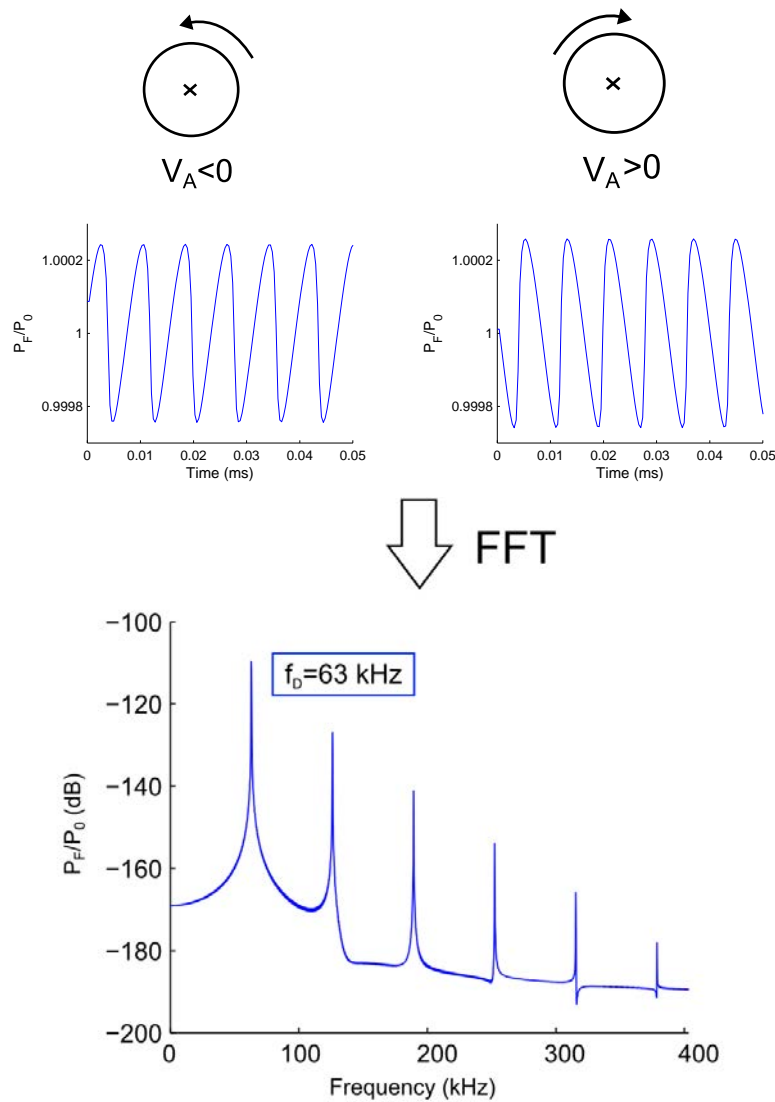
Figure II.13: Top: the OFI emitted power waveform is a function of the target's sense of rotation. Bottom: In frequency domain, both Doppler peaks are superimposed, keeping from direct direction discrimination

The output optical power is plotted in time and frequency domain. In the top of Fig. II.13, the target velocity component is in the opposite direction than the optical axis, i.e. the Doppler shift is positive, whereas in the left part of the figure, velocity component is in the same direction than the optical axis, i.e. the Doppler shift is negative ($f_D = -\frac{2V_A}{\lambda}$).

In time domain, the inclination of the sawtooth-like waveform reverses with the sense of rotation [178], and the translation direction can be recog-

nized. In theory, this technique is reliable and simple to setup. In practice, observing the time-domain signal requires a very high sample rate, so that the waveform can be exploited. Moreover, some effects affect the signal, keeping the signal processing from being straightforward:

- The distribution of Doppler frequencies (finite spot size) modulates the signal envelop (section II.4.3).

- The roughness of most of the surfaces leads to Speckle effect [225].

- For weak coupling factor, the waveform is almost symmetrical, keeping from waveform recognition (section II.4.2).

II.5.1 Model application: LD driving current modulation

The frequency modulation of a laser diode is particularly simple, since the diode frequency is dependent on the driving current. De Groot et al. [196] used this principle on a backscattered LD. The current modulation function was a triangular waveform, as in conventional range finder. However, instead of inspecting the time-domain signal, they demonstrated that in frequency domain, a frequency peak, which varies linearly with the distance to the target appears.

Later, Gui et al. modulated a single longitudinal-mode VCSEL by a dynamic triangular current, and demonstrated that the frequency of the OFI signal during the rising part of the triangular modulation differed from that during the falling part [226]. Furthermore, they pointed out that the two frequencies are reversed as the velocity direction is reversed because positive Doppler shift turns to negative, or vice versa.

To explain these experimental observations, we consider a LD, whose driving current is modulated by a sawtooth wave. The modulating function can be written: $I_{\mathrm{mod}} = I_0 \left(1 + \beta_I t\right)$ where β_I denotes the current modulation coefficient in s^{-1}. It induces a modulation of the laser emission frequency, yielding $\nu_{\mathrm{Fmod}} = \nu_F \left(1 + \beta_\nu t\right)$ (Fig. II.14). Most of the laser diodes exhibit a linear relationship between bias current and optical frequency, thus β_ν is linearly related to β_I.

Like in section II.4.1, the incident electric field can be written:

$$E_{\mathrm{im}} = E_0 \exp j\omega(t)t, \tag{II.57}$$

However, in this case, the laser pulsation $\omega(t) = 2\pi\nu_{\mathrm{Fmod}}(t)$ is time-dependent when the current is modulated.
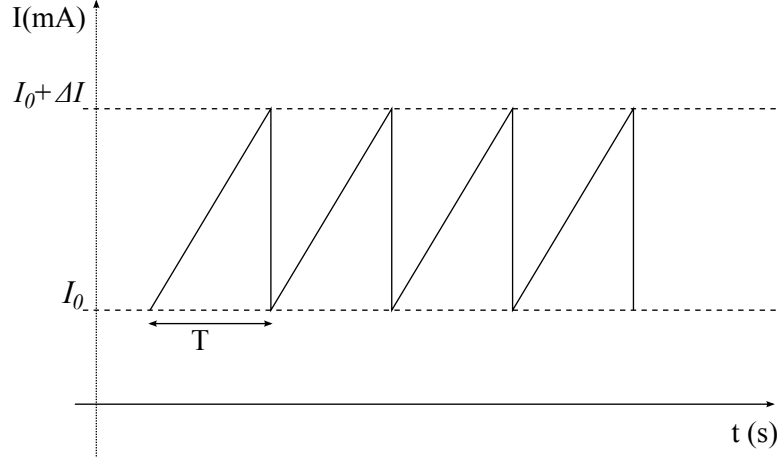
Figure II.14: Modulated driving current, $I_{\mathrm{mod}} = I_0\left(1 + \beta_I t\right)$, $t < T$

The reflected field is shifted in time compared with the incident field, insofar as the wave is travelling during an external cavity round-trip (τ_d) before mixing within the laser cavity.

$$
\begin{align}
E_{\mathrm{r}} &= E_{r1m} + E_{r2m} \tag{II.58}\\
E_{r1m} &= r_2 E_{\mathrm{im}} \tag{II.59}\\
E_{r2m} &= (1 - r_2^2) r_3 E_0 \exp\left(j\frac{c - V_A}{c + V_A}\omega(t - \tau_d)t + j\Phi_{r2m}\right) \tag{II.60}
\end{align}
$$

Not only the Doppler effect affects the expression of the electric field reflected on the target E_{r2m}, but also the optical frequency modulation.

Φ_{r2m} represents the phase difference due to the travel of the wave through the external cavity:

$$
\begin{align}
\Phi_{r2m} &= \int_0^{\frac{\tau_d}{2}} \omega(t - \tau_d)dt + \int_{\frac{\tau_d}{2}}^{\tau_d} \frac{c - V_A}{c + V_A}\omega(t - \tau_d)dt \tag{II.61}\\
&= 2\pi\nu_F \frac{\tau_d}{2}\left[\left(1 - \frac{3\beta_\nu\tau_d}{4}\right) + \frac{c - V_A}{c + V_A}\left(1 - \frac{\beta_\nu\tau_d}{4}\right)\right] \tag{II.62}
\end{align}
$$

where the first term represents the phase difference due to the forward propagating and the second due to the backward propagating wave.

Leading to the following expression:

$$
r_{\mathrm{eq}m} = r_2\left[1 + (1 - r_2^2)\frac{r_3}{r_2}\exp j\left(\omega_M t + \Gamma_M t^2 + \Phi_{r2m}\right)\right] \tag{II.63}
$$

59

With

$$\omega_M = 2\pi\nu_F \left[\frac{-2V_A}{c+V_A} - \beta_\nu\tau_d\frac{c-V_A}{c+V_A} \right] = 2\pi f_{\text{mod}} \qquad \text{(II.64)}$$

$$\Gamma_M = 2\pi\nu_F \frac{-2V_A}{c+V_A}\beta_\nu \qquad \text{(II.65)}$$

The emission frequency expression under modulation is introduced in Eq. II.56, leading to a new expression of the emitted optical power:

$$P_F(t) = P_0 \left[1 + m\cos\left(2\pi\nu_F \left[\left(\frac{-2V_A}{c+V_A} - \beta_\nu\tau_d\frac{c-V_A}{c+V_A} \right) t + \Gamma_M t^2 + \Phi_M \right] \right) \right]$$
$$\text{(II.66)}$$

The coefficient of t describes the angular frequency of the sensor, whereas the coefficient of t^2 add a time dependency to this frequency shift, leading to Doppler peak broadening. If the modulation function has a time-period short enough so that the broadening induced by Γ_M does not affect the frequency peak resolution, the error induced by the term Γ_M is neglectable. In this condition, the frequency peak induced by modulation f_{mod} can be approximated by:

$$\boxed{f_{\text{mod}} = -2\nu_F\frac{V_A}{c+V_A} - 2\nu_F\frac{\beta_\nu L}{c+V_A} = f_{\text{D}} + f_{\text{shift}}} \qquad \text{(II.67)}$$

Where f_{D} represents the Doppler frequency as described in Eq. III.5, and f_{shift} represents the additional frequency shift induced by the driving current modulation. f_{shift} is directly proportional to the distance to the target L, and to the modulation coefficient β_ν.

The effect of optical feedback on a LD under current modulation is simulated with Matlab using the parameters in Table II.4.

Parameter name	Value
LD wavelength	$\lambda = 850$ nm
Linewidth enhancement factor	$\alpha = 5$
Photon lifetime	$\tau_p = 10^{-12}$ s
LD cavity length	$l = 10$ μm
External cavity length	$L = 15$ cm
Velocity of the target	$V_T = 0.15$ m.s^{-1}
Angle between optical axis and velocity direction	$\theta = 80°$
Coupling factor	$C = 0.8$
Modulation coefficient	$\beta_\nu = -0.07$ s^{-1}

Table II.4: Simulation parameters: Direction discrimination

Simulation results for the emitted power affected by the optical feedback when the injection current is modulated are presented in Fig. II.15. In Fig. II.5.1, the target velocity component in the direction of the laser is negative. The frequency peak when the LD current is not modulated is supposed to be at 63 kHz. When the current is modulated by a sawtooth-like waveform, ($\beta_\nu = -0.07$), the peak position is shifted to 88.5 kHz. Symmetrically, when the target velocity component in the direction of the laser is positive, the frequency peak shifts to 37.8 kHz (Fig. II.5.1).

By modulating the driving current of a laser diode suffering from optical feedback, it is possible to discriminate without ambiguity the translation direction of a moving target by analyzing the shift of the frequency peak in the FFT spectrum. These theoretical results show good agreement with Gui experimental observations.

For a LD under current modulation, the frequency peak shifts also with distance (Eq. II.67). By calculating the difference between f_D and f_{mod}, the distance between the target and the laser can be estimated.

A simple illustration of this effect is presented in Fig. II.16, where the fundamental peak shifts towards higher frequencies when the distance between the laser and the target increases. This results have been obtained using the simulation parameters from table II.4.

Our theoretical model corroborates the experimental observations presented by De Groot et al., insofar as the shift of the frequency peak shows a linear relationship with the target distance.

II.5.2 Experimental set-up for velocity direction discrimination

To validate the simulation results, the following experimental setup has been designed (Fig. II.17). It was based on a commercial Lasermate VCSEL (VCT-F85A32-IS-V2) beaming onto a rotating disc. The VCSEL presents a single transverse mode emission at 850 nm. The bias current was 3 mA, leading to an available output power of 1 mW. The device included a monitor photodiode and the VCSEL in the same TO-CAN package.

The LD was driven by a sawtooth-wave signal, with a slope β_I controlled by a function generator. The sensitivity of the lasing wavelength against driving current has been measured experimentally to be $\beta_\nu = -k\beta_I$, where $k = 0.0014$ (Fig. II.18).

The OFI signal was obtained through photodiode current variations and amplified using a 10^5 V/A transimpedance amplifier. The target was a 10 cm
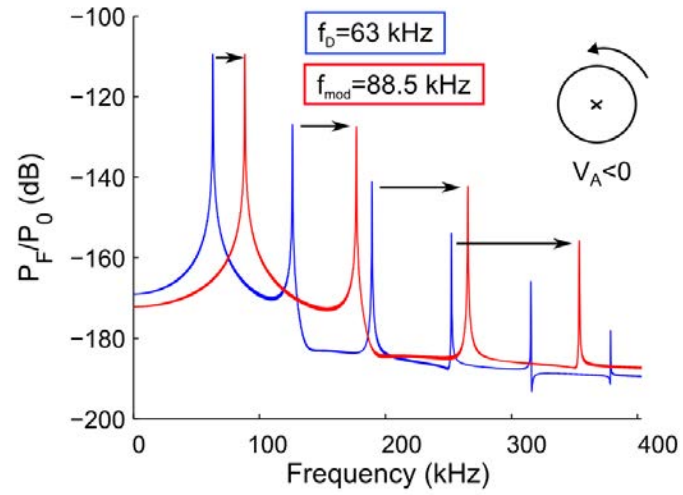
(a)
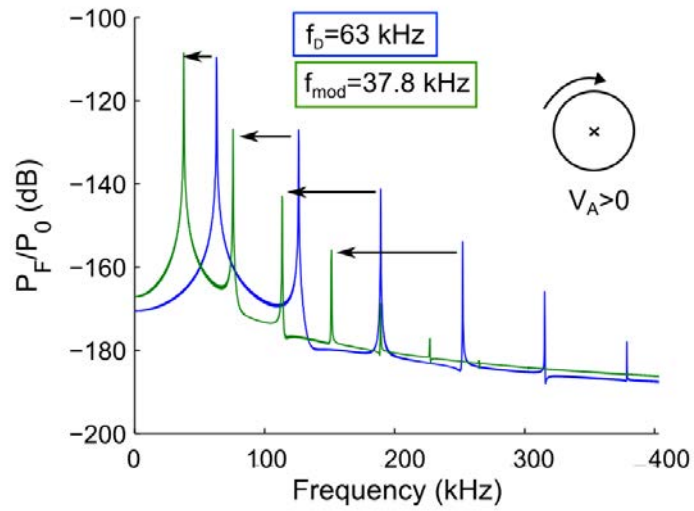
(b)

Figure II.15: Output power waveform for a LD under modulation ($\beta_\nu = -0.07 \text{ s}^{-1}$) (a) $V_A < 0$, the Doppler peak shift towards higher frequencies (b) $V_A > 0$, the Doppler peak shift towards higher frequencies.
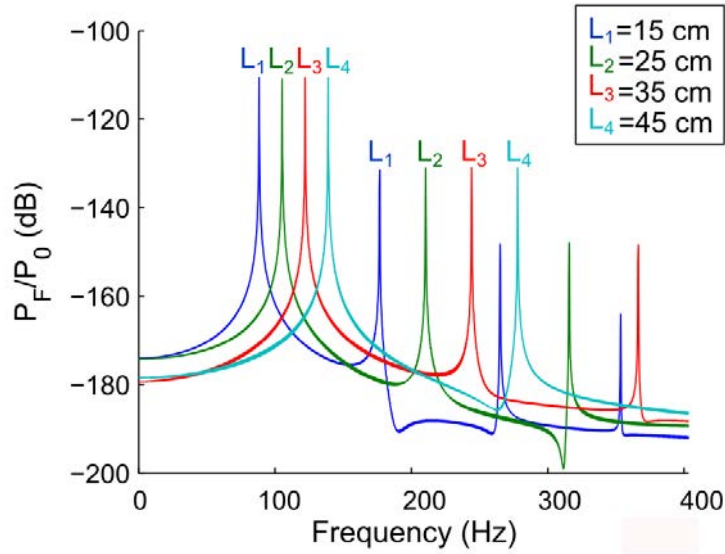
Figure II.16: Frequency peak induced by OFI when the LD current is modulated ($\beta_\nu = -0.07\ s^{-1}$) for various distances $L = [0.15\ 0.25\ 0.30\ 0.45]$ m.
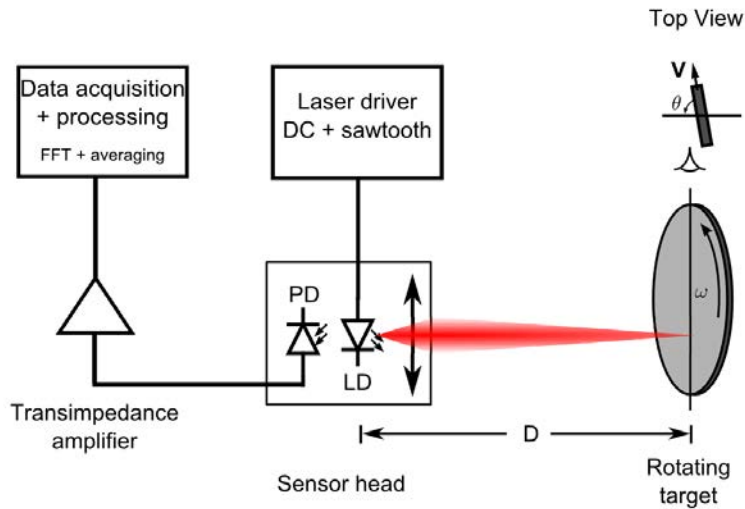
Figure II.17: Scheme of the laser Doppler velocimetry set-up on a rotating target

metallic disk covered by blank paper, rotating at a controlled velocity up to 150 rpm and tilted at an angle of $80°$ from the propagation axis.
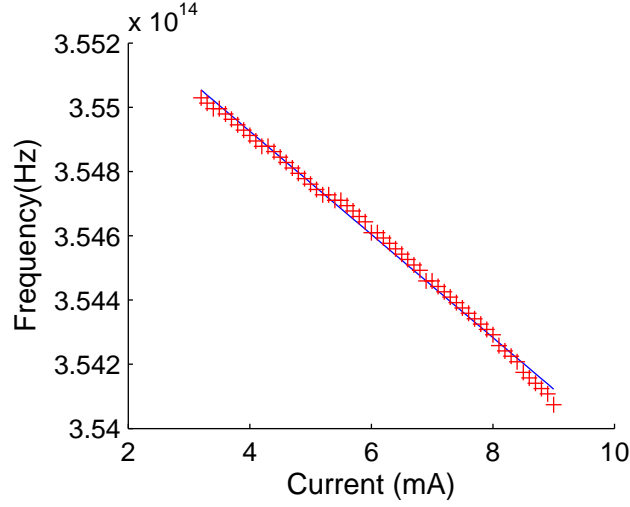
Figure II.18: Experimental characterization: shift in wavelength as a function of driving current

II.5.2.a   Direction discrimination: Experimental results

Using the experimental set-up described above, the velocity vector sign was changed by inverting the rotation of the target, while the driving current I_{mod} was modulated by a periodic sawtooth-wave function (frequency 1 kHz, amplitude 93 μA, $\beta_\nu = -0.043\ s^{-1}$). The target was rotating at 65 rpm, and was at 35 cm from the laser.

The results, plotted in Fig. II.19, show clearly a shift of the Doppler frequency peak that depends on the velocity vector direction. To corroborate the theoretical model, simulated results are plotted on the same figure, using the same experimental parameters. For an expected Doppler frequency of 171 kHz without modulation (central peak), the frequency peak shifts by 43 kHz when the target turns clockwise and -41 kHz when anticlockwise. One can notice that the asymmetry in the shifts values can be explained as the factor $\frac{1}{c+V_T}$ changes slightly with the sign of the target velocity V_T.

Thus, in this configuration, the frequency peak is shifted towards lower frequency when the Doppler frequency without modulation is negative ($V_A > 0$) or higher frequency when the Doppler frequency without modulation is positive ($V_A < 0$).

II.5.2.b   Distance estimation

In addition, target distances were experimentally measured from 0.15 m to 0.5 m and OFI spectra were acquired. The target rotated at 65 rpm, and
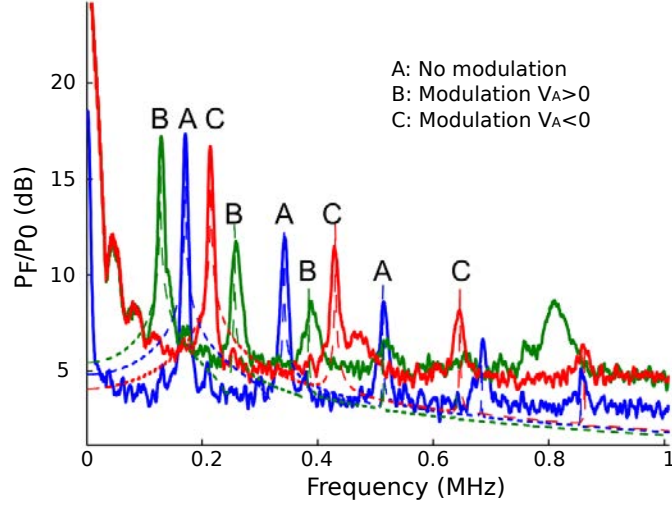
Figure II.19: Experimental (solid curve) and simulated (dashed curve) emitted power in spectral domain without modulation (A), with current modulation and anticlockwise rotation (B), with current modulation and clockwise rotation (C).

the sawtooth modulating current had an amplitude of 80 μA at a frequency of 1 kHz ($\beta_\nu = -0.037\ s^{-1}$). The experimental results (Fig. II.5.2.b) showed as expected a linear relationship between L and the frequency peak. From Eq. II.67, distances were recalculated based upon the experimental data and Fig. II.5.2.b compares the measured and calculated distance values.

The mean-square error on distance measurement, which is around 4.3 % is not surprising, considering that the parameters β_ν and ν_F have been determined experimentally, and are source of inaccuracies. Furthermore, additional errors can be attributed to the uncertainty in the evaluation of the distance between the laser and the target, and to the spectral resolution while calculating the frequency peak.

We have demonstrated that coherent ranging may be performed in a simple backscatter-modulated laser diode with a simple signal processing method.

II.5.2.c   Influence of the modulation strength

To illustrate the impact of the modulation strength on OFI signal, β_ν was set from 0.03 to 0.150 s^{-1}, the target rotating at constant velocity (65 rpm)

65
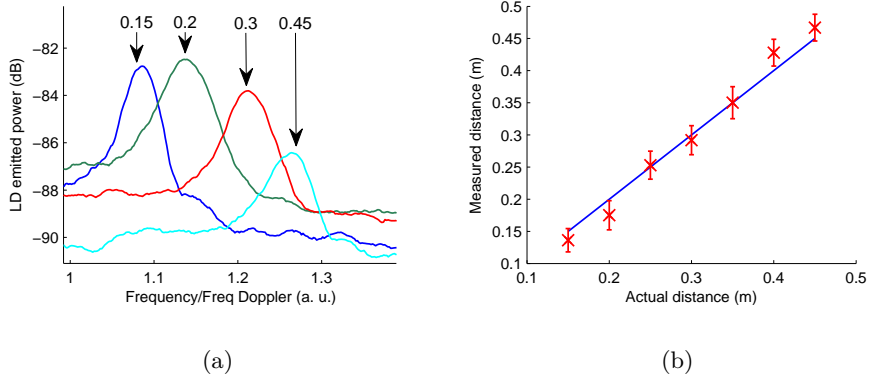
Figure II.20: (a) Normalized frequency peak for $\beta_\nu = -0.037\ s^{-1}$ and various distances $L = [0.15\ 0.2\ 0.3\ 0.45]$ m. (b) Actual distance against measured distance (solid curve) and error bars on 120 measurements (marks).
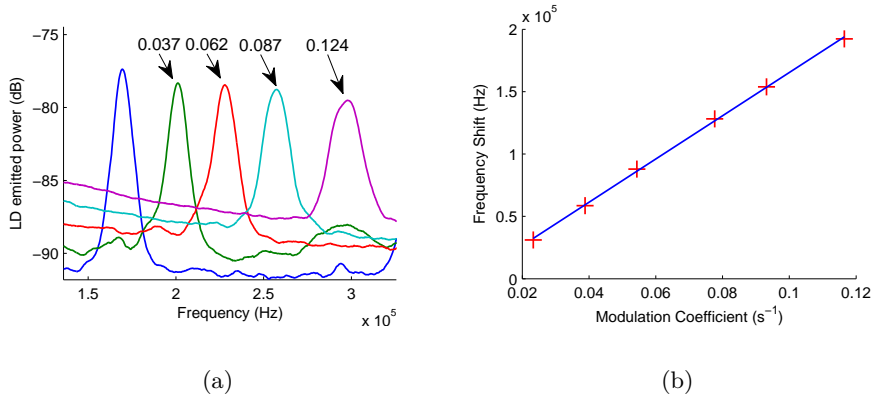
Figure II.21: (a) Doppler peak (lower frequency peak) and frequency modulated peaks for various β_ν: $[0.037\ 0.062\ 0.087\ 0.124]\ s^{-1}$. (b) Linear relationship between the modulation coefficient and the frequency modulated peak.
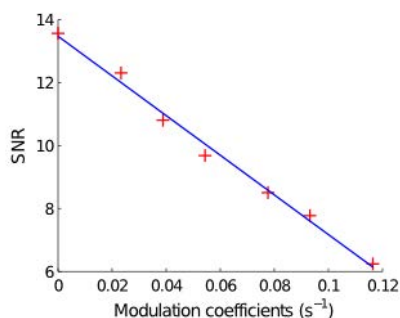
Figure II.22: Signal-to-noise ratio against modulation factor (β_{mod}). Calculated SNR (marks), Polynomial function fit (straight line)

and being at a constant distance (15 cm). Fig. II.5.2.c and Fig. II.5.2.c show the linear evolution of the frequency shift against β_ν.

Moreover, the LD current can be modulated by a sawtooth waveform with a positive or negative slope, leading to several possible configurations. Consequently, the modulation function slope and amplitude can theoretically be optimized regarding the sensors applications, and therefore provide a very high dynamic usable range.

For example, if the target is rotating slowly, the OFI spectrum exhibits a Doppler peak in low frequency domain. The noise induced by the LD is usually of $1/f^\alpha$-type [169], and can overlap between the signal. Consequently, it might be difficult to measure the exact position of the Doppler peak, affecting the sensor accuracy. To counter this problem, the modulation slope and sign can be chosen to shift artificially the Doppler peak towards the higher frequencies, in order to leave the frequency band affected by LD noise. In the opposite case where a target is moving very fast, the Doppler peak might be in the limit of bandwidth allowed by the sensor's surrounding electronics (amplifier, acquisition card). By modulating the current, the frequency peak can be shifted back towards the usable frequency range.

In theory, β_ν can be adjusted regarding the experimental configuration, in order to maintain the Doppler peak in the usable frequency range. This technique could enable to measure extreme velocities, and provide reliable measurement when the angle between the laser diode and the target is close to 90 ° due to restrictive environment.

However, experimentally, a rise of β_{mod} leads to a decrease of the signal-to-noise ratio (SNR) as depicted in Fig. II.22. A loss in SNR can induce measurement errors, and in extreme cases, a total loss of the signal. It

is required to find a compromise between modulation strength and sensors properties.

Chapter III

Optical Feedback Interferometry for fluid flow measurement

III.1 Introduction: Optical feedback interferometry for fluidics applications

Optical Feedback Velocimetry (OFI) have been widely explored for metrological applications on non-cooperative/diffusive (rough surface), retro-reflective (corner-reflector, reflective paper) or reflective (mirror) targets. It has been demonstrated that the strength and shape of the OFI signal is highly dependent on the surface reflectivity and roughness. Particles embedded in a liquid phase can be considered as another group of surface roughness, that differs from the conventional solid target in the following aspects (Fig. III.1):

- The refractive index and reflectivity is not constant in the sensing volume (liquid-solid colloidal suspension)

- The sensing volume is three-dimensional

- The liquid-solid colloid suspension can deposit, aggregate, and deform (i.e the velocity of a liquid can be different from the velocity of particles contained in the liquid)

- The incident beam may interact successively with several particles flowing at different velocities before re-entering the laser cavity

- Small particles can suffer from Brownian motion

Therefore, the influence of the particle type, size, and concentration as well as the three-dimensional sensing volume on the OFI signal are studied, in order to develop a complete sensor for a whole range of fluidic applications.

In this chapter, the characteristic of the light reinjected into the laser cavity when beaming onto particles in aqueous phase is studied. Then, a simple model predicting the aspect of OFI signal using our modified compound cavity model developed for solid targets in Chapter II is proposed. An experimental flowmeter is designed, and the choice of each component is justified. Finally, some basic experimental work is performed (i) to verify the good agreement of the model with theory, (ii) to verify the relevance of our design choices and (iii) to characterize the performance of the sensor for various microfluidics applications.

III.2 Light interaction with a single particle

Individual particles have been measured with light for many years. The determination of the scattered light of the particle and the measurement of the amount of light extinction caused by the particle presence have been
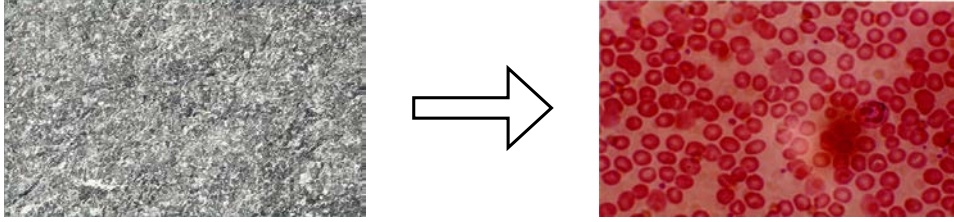
Figure III.1: Illustration of the difference between a conventional rough target and particles embedded in a fluid. Left: Rough stone. Right: Blood

exhaustively studied by Hulst [227] and Bohren [228].

For fluidic applications, the OFI signal is a combination of the incident light and the collected light backscattered by a particle in the direction of the laser. Considering in a first approximation that particles are perfect spheres, the amount of backscattered light depends on the particle size, on the particle refractive index and on the laser wavelength.

Let consider an ideal spherical particle, illuminated by a laser beam. Its scattering behavior can be characterized by the ratio α_p of its radius r_p and the laser wavelength λ [228]:

$$\alpha_p = \frac{2\pi r_p}{\lambda} \tag{III.1}$$

Regarding the value of α_p, the following scattering behavior may apply:

- $\alpha_p < 0.3$: **Rayleigh scattering** theory applies to small particles regarding the wavelength. For example, for an OFI set-up where the laser is a VCSEL emitting at 665 nm, the typical particle diameter for Rayleigh scattering is around 30 nm (ink particle: $r_p \sim 50$ nm, DNA molecule: $r_p \sim 2.5$ nm, proteins: $r_p \sim$1-100 nm). The intensity of the scattered light increases with the particle size, and varies inversely with the laser's wavelength [227] (Fig. III.2) .

- $0.3 < \alpha_p < 30$: **Mie scattering** theory apply for particle sizes comparable to the wavelength of light. For example, for our OFI set-up, the typical particle diameter for Mie scattering is around 1 μm (milk particles: 0.1 μm $< r_p < 3$μm, red blood cells: $r_p \sim 10$ μm, cells: 10 μm $< r_p < 100$μm). The scattered intensity is proportional to the particle radius (Fig. III.2).

- $\alpha_p > 30$: **Geometrical optics** $\rightarrow$ Case of the translating target

Traditional Mie and Rayleigh scattering theories are restricted to spherical, homogeneous, isotropic and non-magnetic particles in a non absorbing medium. However, as most of the practical applications do not meet
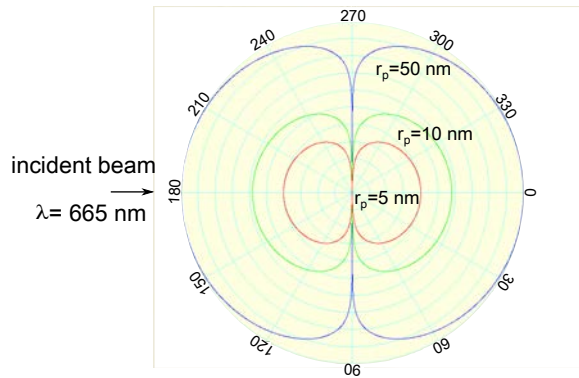
(a)
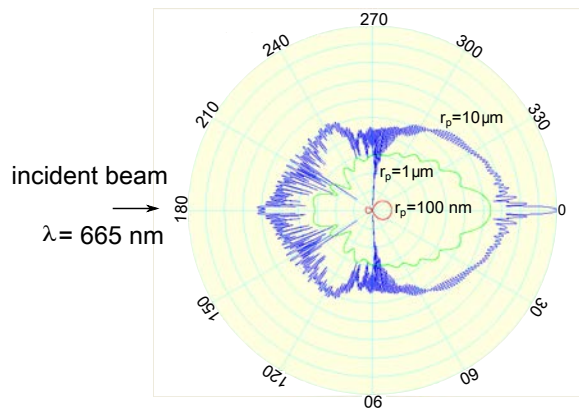
(b)

Figure III.2: (a) Rayleigh scattering: Scattered intensity for various particles radius (r_p= [5, 10, 50] nm). (b) Mie scattering: Scattered intensity for various particles radius (r_p=[0.1, 1, 10] μm). Both figures have been obtained using the software *Mieplot* ©

these conditions, there is much interest in advanced scattering theories. Extensions of theses theory for non-spherical particles (ellipsoids, spheroids, cylinders) have been studied by Mishchenko [229–231]. Scattering by inhomogeneous particles may be computed by volume discrete methods. These theories are also restricted to plane waves, but extension to Gaussian beams have been proposed by Gouesbet [232–234] and Taylor [235].

III.3 Group of particles: Single scattering behavior

III.3.1 Single scattering regime

In most fluidic applications, a single incident beam illuminates a group of particles travelling at different velocities. **Single** or **independent** scattering may occur, where the particles are sufficiently far from each other. Thus, the Doppler shift that affects each photon is due to the scattering of only one particle that can be considered as a localized scattering center. In this section, a theoretical model based on our compound cavity model developed for rough targets in Chapter II is applied to OFI flowmetry.

Some theoretical studies have been carried out to determine the maximum volume concentration for single scattering hypothesis validity [236], i.e. that particle suspensions do not show the effects of near-particle interactions. Quirantes et al. demonstrated that single scattering is mostly dependent on the particle size and separation (i.e. concentration). Single scattering is achieved for an interparticle distance equal to four times the particles radii [237].

III.3.2 Single scattering model

To predict the shape of the OFI signal when flow rate is measured, a model of the OFI sensor operating in single scattering regime is presented in Fig. III.3. This model is based on a new expression of the equivalent reflection coefficient r_{eq}, that take into account each particle contribution to OFI signal.

Let consider in a first approximation, a group of i independent particles, defined by their respective velocity V_i and reflection coefficient $r_{ext i}$, as depicted in Fig. III.3. r_{3i} represents the amount of light that is reflected by the particle in the direction of the laser, and can be calculated using Rayleigh or Mie scattering theories. For standard particles embedded in a fluid, we suppose that $r_{3i} \ll 1$, as each particle reflects a very small amount of the incident light, and only a part of it, noted $r_{ext i}$, couples with the incident light in the LD cavity. Thus, the OFI flowmeter operates in very
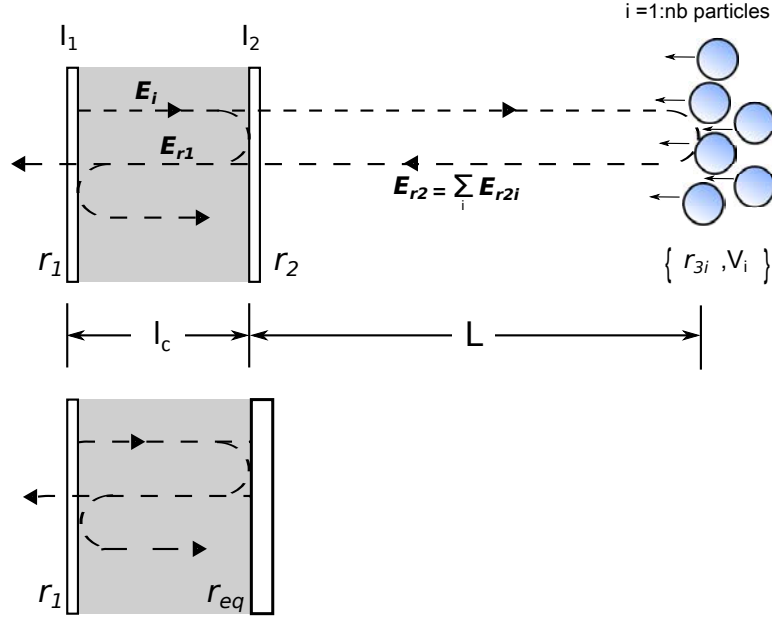
Figure III.3: Schematic arrangement of a laser diode beaming on a group of particles: extension of the compound cavity model.

weak regime ($C \ll 1$).

By the same token as the establishment of the expression of r_{eq} in chapter II, the ratio of the reflected electric field E_r to the incident electric field E_i on the equivalent interface I_{eq} is calculated:

$$E_i = E_0 \exp j\omega t \tag{III.2}$$

$$E_r = r_2 E_i + (1 - r_2^2) \sum_i r_{\text{ext}i} E_0 \exp\left(j\frac{c - V_i}{c + V_i}\omega t + j\Phi_{r2i}\right) \tag{III.3}$$

With $\Phi_{r2i} = 2\pi\nu_F \left(1 + \frac{c - V_i}{c + V_i}\right) \frac{\tau_d}{2}$

Leading to the complex expression of r_{eq}:

$$r_{\text{eq}} = \frac{E_{r1} + (1 - r_2^2) \sum_i r_{\text{ext}i} E_0 \exp\left(j\frac{c - V_i}{c + V_i}\omega t + j\Phi_{r2i}\right)}{E_i}$$

$$= r_2 \left[1 + (1 - r_2^2) \sum_i \frac{r_{\text{ext}i}}{r_2} \exp j\left(\omega_i t + \Phi_i\right)\right] \tag{III.4}$$

With

$$\omega_i = 2\pi\nu_F \frac{-2V_i}{c + V_i} \tag{III.5}$$

74

$$\Phi_i = 2\pi\nu_F \left(1 + \frac{c - V_i}{c + V_i}\right) \frac{\tau_d}{2} \tag{III.6}$$

The complex expression of (III.4) is developed to identify the modulus and argument of r_{eq}, that will be reintroduced in the OFI compound cavity model. To simplify the mathematics development, let $\frac{(1-r_2^2)}{r_2} r_{\text{ext}i}$ be ζ_i.

$$
\begin{aligned}
\|r_{eq}\| &= \sqrt{Re(\text{eq})^2 + \text{Im(eq)}^2} \\
&= r_2\sqrt{\left(1 + \sum_i \zeta_i \cos(\omega_i t + \Phi_i)\right)^2 + \left(\sum_i \zeta_i \sin(\omega_i t + \Phi_i)\right)^2} \\
&= r_2\sqrt{1 + 2\sum_i \zeta_i \cos(\omega_i t + \Phi_i) + \left(\sum_i \zeta_i \cos(\omega_i t + \Phi_i)\right)^2} \tag{III.7} \\
&+ \overline{\left(\sum_i \zeta_i \sin(\omega_i t + \Phi_i)\right)^2} \tag{III.8}
\end{aligned}
$$

Knowing that $\left(\sum_i x_i\right)^2 = \left(\sum_i x_i\right)\left(\sum_j x_j\right) = \sum_i x_i^2 + 2\sum_{i<j} x_i x_j$ and using trigonometric formula, $\|r_{eq}\|$ becomes:

$$
\begin{aligned}
\|r_{eq}\| &= r_2\sqrt{1 + 2\sum_i \zeta_i \cos(\omega_i t + \Phi_i) + \sum_i \zeta_i^2} \\
&+ \overline{2\sum_{i<j} \zeta_i \zeta_j \cos((\omega_i - \omega_j)t + \Phi_i - \Phi_j)} \tag{III.9}
\end{aligned}
$$

Assuming that the sensing volume is small and the velocity of the different particles are close enough to write $\omega_i \sim \omega_j$ and $\Phi_i \sim \Phi_j$, yieldings:

$$\|r_{eq}\| \sim r_2\sqrt{1 + 2\sum_i \zeta_i \cos(\omega_i t + \Phi_i) + \sum_i \zeta_i^2} \tag{III.10}$$

Knowing that $\zeta_i^2 << 1$, we can write:

$$\|r_{eq}\| \sim r_2\sqrt{1 + 2\sum_i \zeta_i \cos(\omega_i t + \Phi_i)} \tag{III.11}$$

With the same development, the expression of Φ_{eq} is established:

$$
\begin{aligned}
\Phi_{eq} &= \arctan\left(\frac{Im(r_{eq})}{Re(r_{eq})}\right) \\
&\sim \sum_i \zeta_i \sin(\omega_i t + \Phi_i) \tag{III.12}
\end{aligned}
$$

We deduce the emission frequency of the LD under feedback ν_F in function with the optical emission frequency in the free running state ν_0, including the Doppler effect induced by particles:

$$\nu_F = \nu_0 - \sum_i \frac{C_i}{2\pi\tau_d} \sin\left(\omega_i t + \Phi_i + \arctan\alpha\right) \qquad \text{(III.13)}$$

Yielding to the following changes in the expression of the LD optical output power under feedback P_F in function with the optical output power in free running state P_0:

$$P_F = P_0 \left[1 + \sum_i m_i \cos\left(\omega_i t + \Phi_i\right)\right] \qquad \text{(III.14)}$$

Where C_i and m_i are respectively the OFI coefficient and modulation index calculated from each contribution. In frequency domain, the OFI signal exhibits a range of Doppler frequencies $F_{\text{Di}} = \omega_i/2\pi$, which magnitude is determined by m_i.
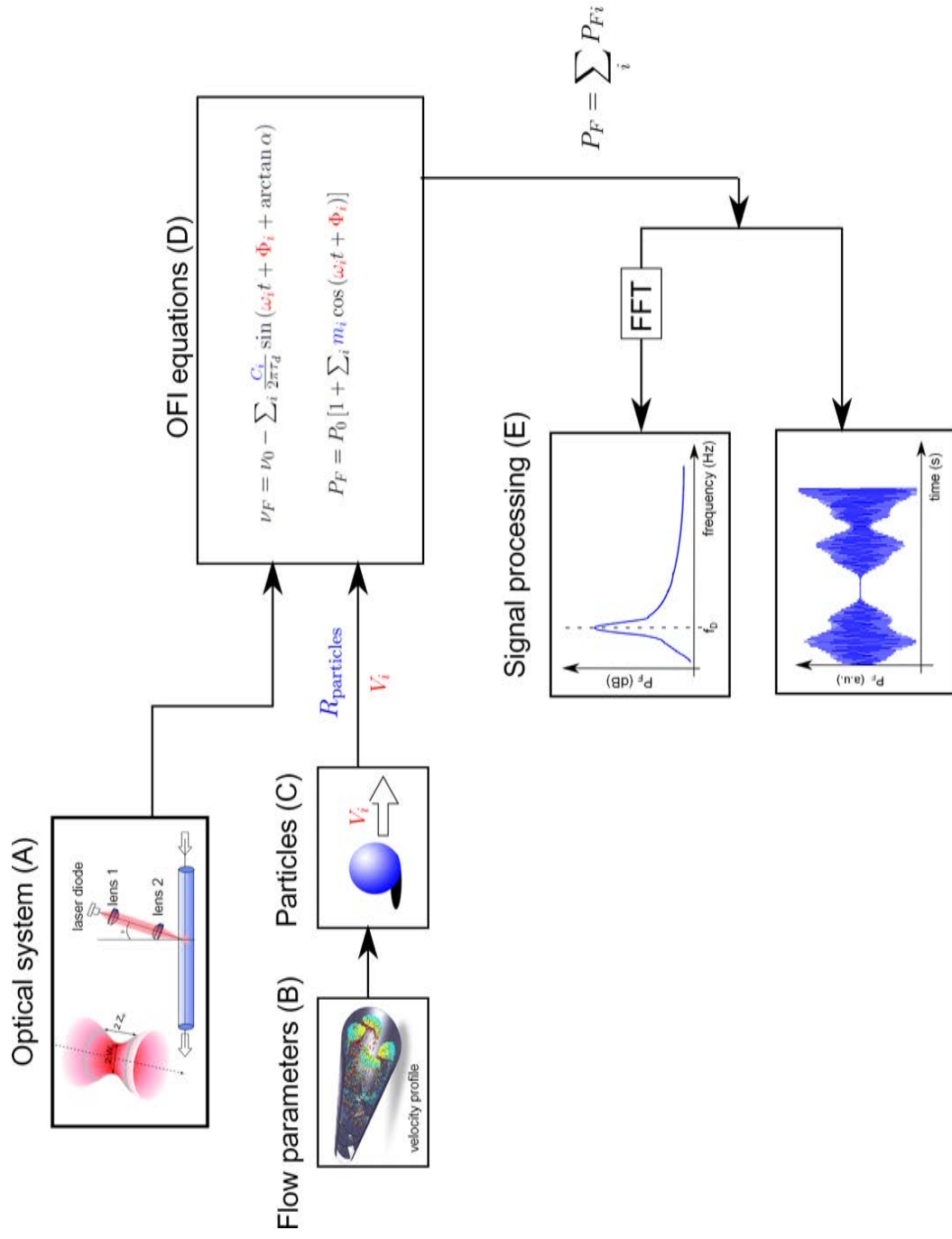
Figure III.4: Schematic arrangement of the OFI flowmeter operating in single scattering regime. The function of each block is detailed in the text

This simplified model has been implemented using Matlab (Fig. III.4), and can be used to study the influence of the particles concentration, reflectivity and velocity distribution. Therefore, the OFI signal for fluidic applications can be predicted.

The single scattering model is succinctly described as follows:

(A) **Optical system** The laser wavelength, the incident Gaussian beam parameters and the magnification system are defined in this block. The theoretical sensing volume is specified, and can be coupled with the flow parameters to specify the part of the flow that is illuminated.

(B) **Flow parameters** The geometry and size of the channel is described, so that the theoretical velocity distribution can be calculated.

(C) **Particles** Before being introduced in the OFI system, each particle is described by its reflection coefficient ($R_{\mathrm{particles}}$), its velocity (V_i) and its illumination (i.e. if it is located in the center of the Gaussian beam, or near the edge). The size, concentration and position of the particles determine the number of contributions that will be summed to contribute to the OFI signal.

(D) **OFI equations** The solver calculates the change in frequency ν_F and in optical power P_F for a laser diode beaming onto a flowchannel, giving rise to the theoretical time-domain OFI signal.

(E) **Signal processing** A FFT is performed on the time-domain signal, providing a frequency distribution, that is fitted with a Gaussian function.

III.3.3 Model application: a Newtonian liquid flowing through a pipe in the laminar regime

As a model application, the simple case of a Newtonian liquid flowing through a circular flowchannel is considered. For a laminar flow, the velocity profile in a circular channel is parabolic, with the velocity increasing from zero at the wall (no slip boundary condition) to a maximum value at the center. The velocity distribution is plotted in Fig. III.5 and follows the Hagen-Poiseuille law [73]:

$$V(r) = V_{\mathrm{max}} \left(1 - \frac{r^2}{R^2} \right) \tag{III.15}$$

Where V_{max} is the velocity in the center of the channel, R the radius of the flowchannel, and r is the radial position. In the center of the channel, $r{=}0$, whereas $r{=}R$ at the channel's walls.
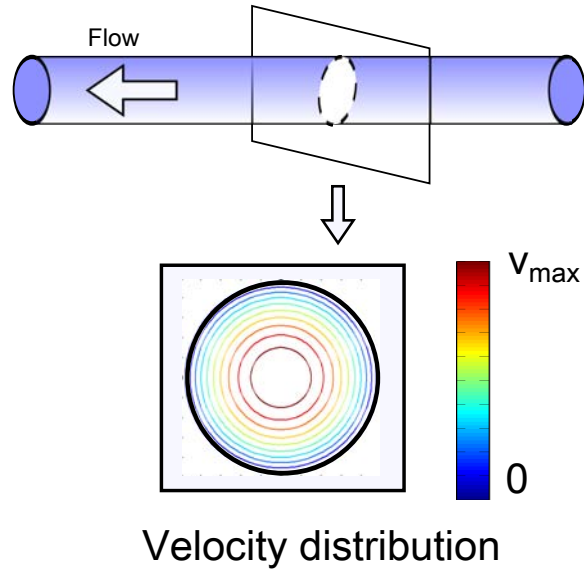
Figure III.5: For a laminar flow, the velocity distribution in a circular channel is governed by Eq. III.15. The profile is parabolic; the velocity is maximal in the center and zero at the walls.

Parameter name	value
LD wavelength	$\lambda = 665$ nm
Linewidth enhancement factor	$\alpha=5$
LD cavity length	$l_c=10$ μm
External cavity length	$L = 10$ cm
Maximum velocity	$v_{max} = 6$ mm/s
Flowchannel radius	R = 500 μm
Angle between optical axis and flow direction	$\theta = 75°$
Refractive index	n = 1.33

Table III.1: Simulation parameters: influence of the spot size on the Doppler peak position
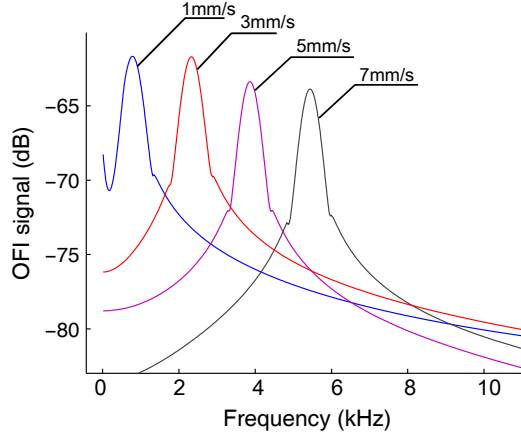
Figure III.6: Simulated OFI spectrum for various measured velocities $V_{\max}$ [1, 3, 5, 7] mm/s. The sensing volume is small compared to the flowchannel's radius. The Doppler peak is proportional to the velocity value

The parameters described in Table III.1 have been used to calculate the theoretical OFI signal in frequency domain. The LD spot diameter has been set to 50 μm, and its intensity follows a Gaussian distribution centered on the center of the flowchannel. With this configuration, we simulate how the maximum velocity of the flow profile can be measured. The program has been run for several values of $V_{\max}$: [1, 3, 5, 7] mm/s. Thus, the corresponding theoretical Doppler frequencies values are respectively [1, 3.1, 5.2, 7.2] kHz, and can be calculated using:

$$f_D = \frac{2V_{\max}ncos(\theta)}{\lambda} \tag{III.16}$$

Where n is the refractive index of the surrounded liquid, θ the angle between the laser and the flow direction and λ the laser wavelength.

The results are presented in Fig. III.6. It can be observed that the frequency spectrum exhibits a Gaussian peak, which center position f_D is proportional to $V_{\max}$. In addition, the calculated frequencies match exactly the theoretical values.

III.3.4 Influence of the spot size on the OFI spectrum

A simulation was performed for several spot radii, based on the simulation parameters described in Table III.1. The spot radius varies between 50 μm and 500 μm. The particles are supposed to be identical, so that they have the same size and refractive index. The simulation principle is illustrated in Fig. III.3.4, and the results are plotted in Fig. III.3.4.

(a)   (b)
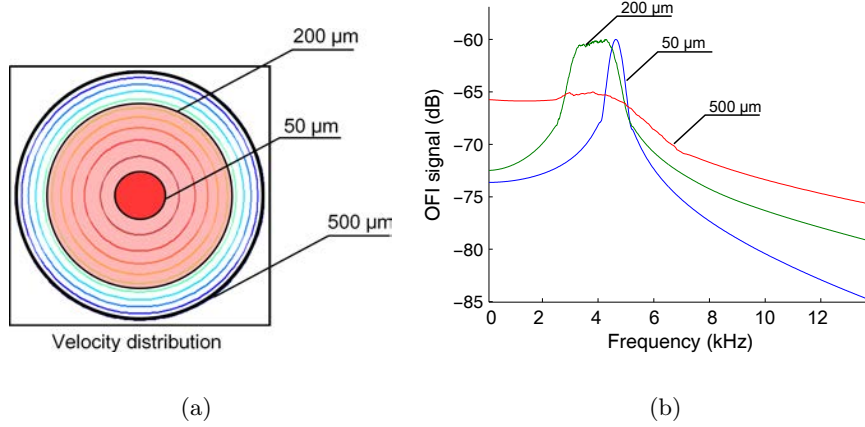
Figure III.7: Theoretical OFI spectra for various spot sizes.

The OFI signal in OFI flowmetry does not always exhibit a Gaussian shape. The OFI spectrum can be seen as a frequency distribution, which is directly related to the velocity distribution of the particles in the sensing volume, and to the illumination function of the incident beam. As long as the sensing volume is small compare to the flowchannel section, the signal shape is Gaussian, and the information is extracted by fitting the Doppler peak with a Gaussian function. When the sensing volume size becomes significant compare to the size of the flowchannel, a well-defined peak cannot be recognized in the spectrum, and the OFI signal exhibits a flat profile, as depicted in Fig. III.3.4.

III.4   OFI experimental set-up

To investigate the effects which has been observed theoretically, we designed a complete OFI sensor dedicated to microfluidic applications. As a second step, we reproduce experimentally the experimental configuration simulated using the coumpound cavity model for OFI flowmetry.

III.4.1   Theoretical sensing volume in OFI flowmetry

The most important experimental parameter in OFI flowmetry is the sensing volume, that determine the properties of the measured signal, and consequently the precision of the sensor. Before choosing the set-up components, it is necessary to define the notion of sensing volume in OFI flowmetry, and to identify the parameter that have an influence on it.
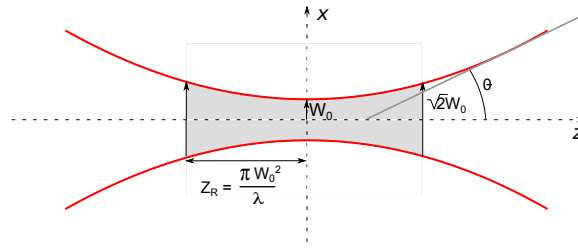
Figure III.8: Schematic arrangement of a Gaussian beam

III.4.1.a   Gaussian beam

The output beam of a laser, when travelling in free space (or a homogeneous medium) is almost pure TEM (transverse electric and magnetic), and can be approximated as a Gaussian beam [238]. At all cross sections along the laser beam, the light intensity has a Gaussian distribution, and the width of the beam $2W(z)$ is usually defined by the edge-intensity being $1/e^2 = 13\%$ of the center intensity.

We consider a Gaussian beam travelling along the z axis, that coincides with its axis of symmetry as depicted in Fig. III.8. Laser beam propagation can be described using:

$$W(z) = W_0\sqrt{1 + \left(\frac{z - Z_0}{Z_R}\right)^2} \qquad \text{(III.17)}$$

with

$$Z_R = \frac{\pi W_0^2}{\lambda} \qquad \text{(III.18)}$$

Where $W(z)$ is the beam radius, that will be at a minimum value W_0 at one place along the beam axis, named the beam waist. Z_0 is the location of the beam waist, Z_R the Rayleigh length, and λ the laser wavelength.

At a distance from the waist equal to the Rayleigh length Z_R, the width $W(z)$ of the beam is:

$$W(\pm Z_R) = W_0\sqrt{2} \qquad \text{(III.19)}$$

The distance b between these two points is called the depth of focus of the beam, and is equal to $2Z_R$.

The Gaussian beam can be fully characterized by measuring the waist or the divergence of the beam θ_D that is given by:
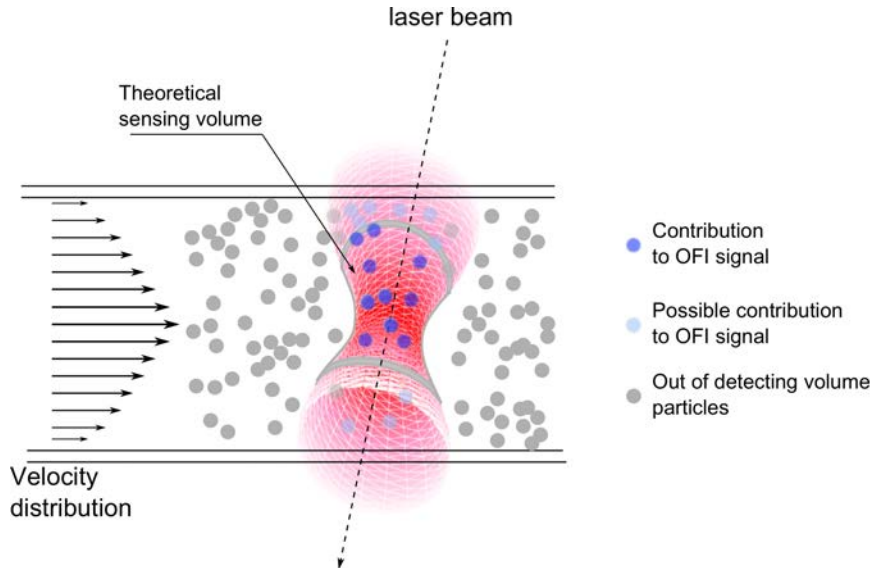
Figure III.9: Schematic diagram of OFI applied to flow measurement. The laser beam is focused inside the flow channel, and is reflected by the particles travelling in the sensing volume. Some particles out-of-focus may also contribute to the OFI signal.

$$\theta_D \simeq \frac{\lambda}{\pi W_0} \qquad \text{(III.20)}$$

The geometry and behavior of the laser beam are governed by this set of simple of beam parameters, which are employed to make the boundaries of the theoretical OFI three-dimensional sensing volume.

III.4.2   Estimation of the OFI sensing volume

To estimate the theoretical position and size of the sensing volume, the whole optical sensor has been modelled using the ray transfer matrix analysis for Gaussian beam [239]. Each optical part is described by a transfer matrix, and tracing the propagation of the Gaussian beam through the optical system can be performed by multiplying this matrix with a vector representing the incident beam. The LD beam is assumed to be a perfect Gaussian beam, and the thin lens approximation to be valid. (See Appendix C).

In OFI systems the illumination and collection beams spatially overlap. Assuming that the laser operates in the fundamental Gaussian mode, the measurement volume centered around the beam focus, can be defined in the first approximation as the volume within which the optical intensity has a

magnitude higher than $1/e^2$ of the intensity peak value [224]. This theoretical sensing volume is depicted in Fig. IV.4.3, and is hourglass shaped. The radius varies from W_0 (thinnest section) to $\sqrt{(2)}W_0$ (largest section).

In theory, only the particles travelling in this sensing volume should contribute to the OFI signal. However, in real experimental conditions, several parameters affect the definition of the measurement volume.

First, the propagation of the light beam through non-planar interfaces such as air/PDMS or PDMS/liquid interfaces leads to distortion and diffraction. Furthermore, the propagation through the liquid attenuates the light beam. Consequently, the particles situated before the beam waist are more detected than the one situated after it, deeper in the liquid. In summary, the previous definition of the measurement volume is valid if at any point of the defined volume, the quantity of backscattered light reinjected in the laser is sufficient enough to be detected. If this condition is not matched, the measurement volume is a volume included in the theoretical volume and centered at Z_0.

To conclude, the measurement volume definition depends on the noise induced by the sensor, the optical link budget, and the density and reflectivity of the particles. Throughout this chapter it is understood that the calculated measurement volume is only an estimate of the effective detection volume.

III.4.3   Light source

III.4.3.a   Choice of a LD: Vertical-cavity surface-emitting laser (VCSEL)

The LD employed for OFI flowmetry requires a good sensitivity, a small beam divergence, a high integration density and a low cost. Furthermore, for possible medical applications, low power and appropriated skin penetration depth are also important parameters. Wavelength between 600 nm and 900 nm can be employed for subcutaneous blood flow sensing [240].

The VCSEL, as per its structure, has a smaller cavity length which can support only longitudinal mode of operation. The small volume of the active region also leads to lower threshold current, which reduces the electrical requirements of the driving electronics. Another advantage of VCSELs is the ability to fabricate a circularly symmetric semiconductor structure. Edge-emitting lasers typically emit light through a non-symmetrical aperture which leads to an elliptical and strongly divergent laser beam. This is a major disadvantage when attempting to couple light into optical fibers

or with free-space optics, since these components have round mode profiles and a large amount of power can be lost. The semiconductor structure of a VCSEL naturally lends itself to a circularly symmetric beam shape with very low astigmatism, and as the OFI signal is highly dependent on the sensing volume, circular and narrow laser beams are of great interest for microfluidics applications. Furthermore, light emission is perpendicular to the semi-conductor wafer surface, allowing the device to be directly tested on the wafer. This leads to a low-cost manufacturing method, unlike the edge emitting lasers that need to be extracted from the wafer and packaged before testing.

Also, the direction of the light emission allows designing VCSEL arrays which are attractive solutions for low-cost OFI flowmeters that can be integrated into parallel arrays, to acquire a whole map of velocities in one measurement [148].

III.4.3.b Light source characterization

(a)   (b)
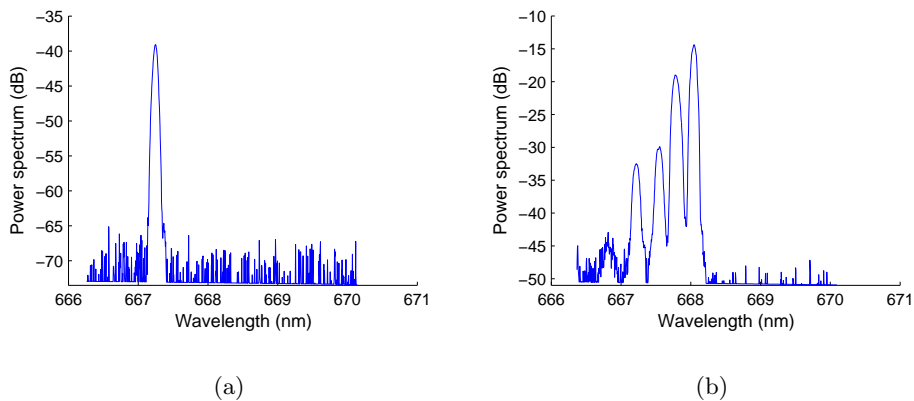
Figure III.10: Emission spectrum of the Firecomms RV M66ST at an injection current of (a)1.8 mA and (b) 4 mA. The VCSEL was found to exhibits a multimode transverse behavior for an injection current higher than 2 mA, leading to a decrease of the OFI sensitivity and of the spatial resolution.

The VCSEL employed throughout this experimental work was a commercial VCSEL (Firecomms, model RVM665T) lasing at 667 nm with a threshold current, I_{th}, of 0.8 mA. The emission spectra of this VCSEL for an injection current of 1.8 mA and 4 mA have been characterized using a custom experimental test-bench and are shown in Fig. III.4.3.b and Fig. III.4.3.b respectively. The light-current characteristics are depicted in Fig. III.4.3.b.

85
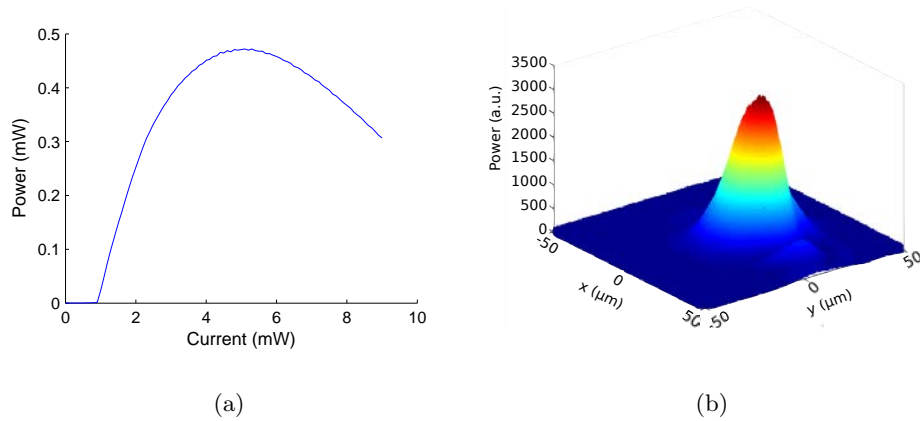
Figure III.11: (a) Light-current characteristic at 25°C and (b) beam waist measurement of the Firecomms RVM665T driven by a bias current of 1.8 mA using a beamprofiler

The beam waist output has been measured to be 12.2 μm using a beamprofiler (Fig. III.4.3.b). This laser was found to have a single transverse mode emission for current below 2 mA, where its sensitivity to optical feedback is higher and where its spatial resolution is expected to be better. This laser has been chosen because it was found to exhibit good optical feedback sensitivity and stability with respect to other VCSEL tested. In all experiments the VCSEL was operated at a constant current of 1.8 mA to avoid multimode behaviour.

Although this particular VCSEL provided better results for our specific set-up, other VCSELs can be employed for OFI flowmetry, in order to investigate other wavelengths and beam waist sizes.

III.4.4 Laser junction voltage vs acquisition through monitoring photodiode

In OFI configuration, it is possible to acquire the signal in two different ways. Most of the OFI sensing systems employ a photodiode (PD) to monitor the self-mixing effect that occurs within the LD. This sensing technique is predominantly used due to its robustness and reliability in single channel sensing systems (Fig. III.12).

However, using directly the change in laser diode junction voltage provides some advantages including reduction in manufacturing and component cost due to absence of the PD in the laser package. On the other hand, the
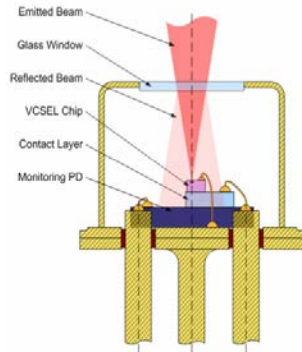
Figure III.12: Cross section of a VCSEL with its monitoring photodiode.

Notation	focal length (mm)	NA
C220TME-B	11	0.25
C230TME-B	4.51	0.54
C240TME-B	8	0.5
C260TME-B	15.29	0.16

Table III.2: Lens characteristics supplied by Thorlabs

SNR associated with the voltage detection scheme is smaller than that of the PD scheme. It implies that the maximum speed that can be measured with voltage detection will be less than the photodiode. However, the bandwidth of the photodiode is generally limited as it is generally used for average power monitoring, which suggests that the voltage detection system will be able to measure greater flow rates for a well designed optical system.

III.4.5   Set-up description

The proposed OFI flowmeter prototype is described in Fig. III.13 and can be succintely described as follow:

The light beam emitted by the LD is guided through an optical system in the flowchannel. The optical system can consist in zero, one or two lenses, depending on the applications (rapid scan of large areas, precise velocity profiles in microchannels...), and set the size and shape of the sensing volume. The lenses employed ifor our optical systems have been chosen among those presented in Table III.2. To monitor the position of the sensing volume in the channel, the sensor head (LD and optical system) is mounted on a goniometer, itself fixed on a 3-D motorized linear stage. Using Labview, the position of the sensor head, (i.e. the sensing volume) can be set in three dimensions, with a resolution of 0.4 μm. The light is then refracted by the seedings embedded in the liquid flowing in the flowchannel, and a small portion reenters the LD's cavity. The LD's junction voltage, which is

87

disturbed by the parasitic light, is then acquired, amplified and fed into an analog-digital converter. This OFI signal is finally acquired in Labview, and can be analyzed using various signal processing methods by the user.

In this setup, some components are common to all experiments (circuitry, data acquisition cards etc...) whereas some elements depend on the experiments (flowchannel, liquid and seeding, flow control system, laser diode, optical system...). Table III.3 summarizes all the components constituting the OFI sensor. Throughout this thesis, it is understood that if an experimental parameter is not described at the beginning of an experiment, the generic component have been employed.
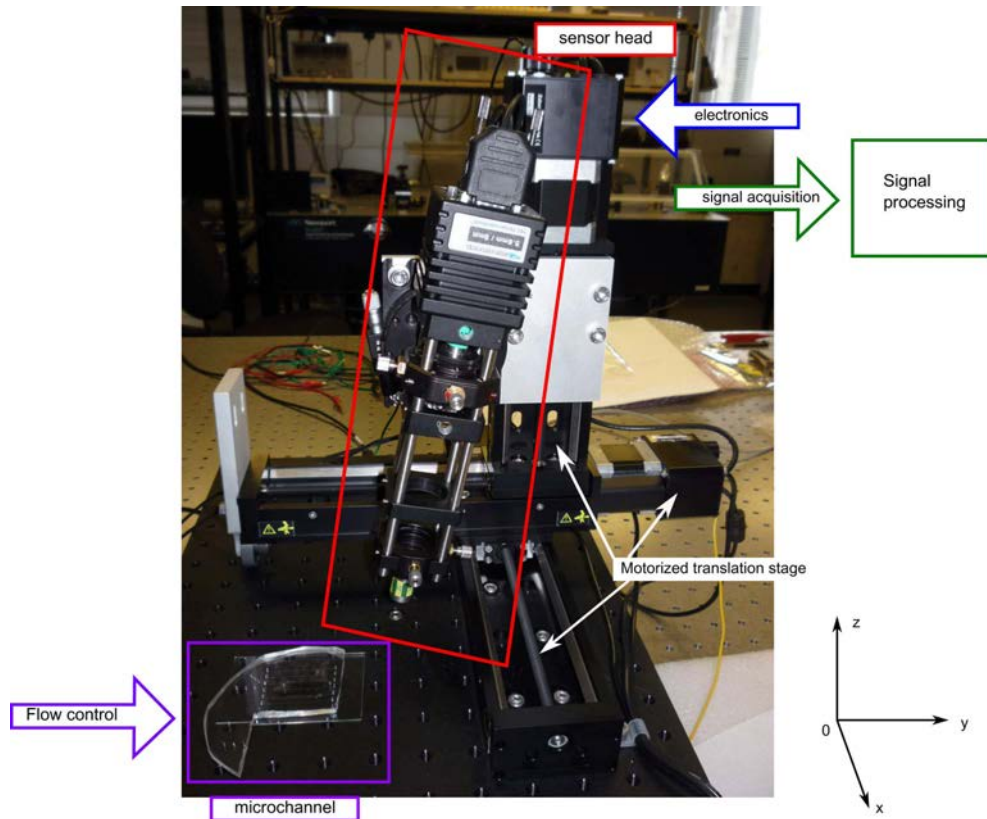
(a)
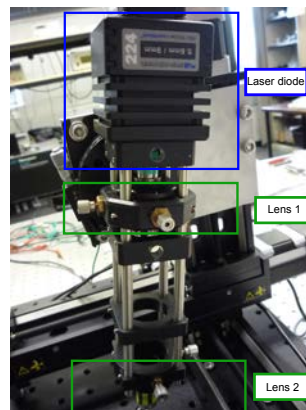
(b)

Figure III.13: (a) OFI flowmeter experimental set-up (b) OFI sensor head (here in two lenses configuration)

Name	Description	Common element Y/N
Optics		
LD	Red or Infrared VCSEL	Y- Firecomms RVM665T @ 667 nm [1]
Lens 1	Impose the size, shape and position of the sensing volume	N
Lens 2 (optional)	Impose the size, shape and position of the sensing volume	N
Electronics [2]		
Laser driver	Deliver DC or time varying current 0-50mA	Y
Low noise amplifier	Amplify voltage signal, Gain can be adjusted by user	Y
Differential amplifier	Get rid of ground loops	Y
Mechanics		
3D linear motorized stages	Position the sensing volume in the channel	Y- Zaber (T-LSB150A-KT03) spatial resolution: 0.4 μm maximum scanning speed: 58 mm/s
Signal processing		
Data acquisition card	Signal acquisition	Y-16-bits DAQ National Instruments
Fluidics		
Syringe pump	Deliver steady state or periodic flow rate	Y-HARVARD Apparatus PHD 22/2000 [1]
Syringe	Control fluid distribution	Y- SGC Glass syringe, 10 mL [1]
Tubing	Junction between the syringe and the needles	Y- 500 μ internal diameter, Teflon [1]
Needles	Junction between the tubing and the flowchannel I/O	Y- 23g needle [1]
Flowchannel	Transport liquids	N
Seeding	Tracers	N

Table III.3: OFI sensor components description - Hardware

[1] Except for the flow profile measurement in macrochannel, see Section IV.1

[2] The circuitry has been designed and built by YL Lim and R. Kliese from UQ, see [241] for further details
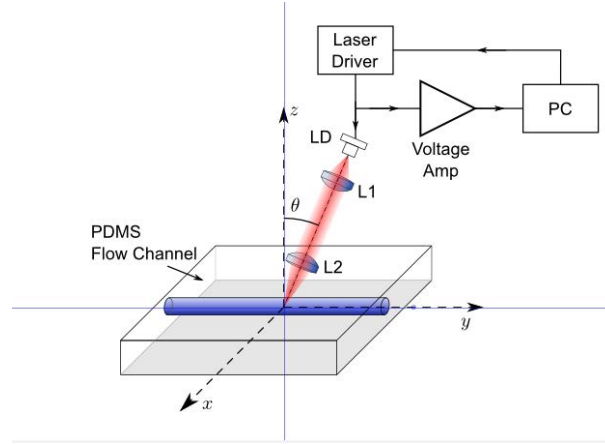
Figure III.14: Block diagram of the OFI flowmeter

III.5   Macrochannel in single scattering regime

In OFI flowmetry, a flowchannel is considered as macro when it is large enough, so that the estimated sensing volume is at least 10 times smaller than the flowchannel typical size. For such channels, and for a liquid where the particle concentration is low enough that multiple scattering can be ignored, a peak appears in the frequency spectrum corresponding to the mean Doppler frequency of the moving particles within the sensing volume.

The position of this Doppler peak is linked to the velocity using:

$$f_{\text{Doppler}} = \frac{2nV_{\text{flow}}\cos(\theta)}{\lambda} \qquad \text{(III.21)}$$

where θ is the angle the target velocity vector makes with respect to the propagation axis of the laser beam, λ is the laser wavelength in free-space and n the refractive index of the surrounding medium.

III.5.1   Impact of flow rate

Velocity measurement were performed using a microfluidic channel with circular cross-section of inner diameter 320 μm, fabricated using Polydimethylsiloxane (PDMS) with the refractive index of 1.4 (Appendix D).

This circular flowchannel was filled with a liquid that guarantee single scattering regime (2 % of milk, 98 % of water). The flow rate Q was controlled using a syringe pump (HARVARD apparatus PHD 2000 Infusion). The laser was angled at 80° with respect to the flow direction. The refractive index of the liquid under test is 1.33. The laser bias current was of 1.8 mA. A dual lens system was employed, (lens 1: C260 and lens 2: C240

Figure III.15: OFI signal in frequency domain measured at the middle of the channel and the corresponding fitting curve (Eq. (III.22)).

Parameter	Numerical values
Flowchannel	circular cross-section (diameter = 320 μm)
Liquid	Milk-water (2%-98%)
Refractive index	1.35
Lens 1	C260-TEMB (f=15.26 mm)
Lens 2	C240-TEMB (f = 8 mm)
θ	75°
LD driving current	1.8 mA
LD wavelength	667 nm

Table III.4: Parameters used for OFI measurement in single scattering regime

(a)

(b)

Figure III.16: (a) OFI signal in the frequency domain for several flow rates (0, 10, 20, 30, 40 and 50 µL.min^{-1}) (b) Plot of the Doppler frequency as a function of velocity in the center of the tube $V_{\max} = 2Q/S$.

see Table III.2), and the estimated sensing volume has been calculated to be $7.16 \cdot 10^5$ μm^3 (Table III.4)

The laser beam focus was moved to the middle of the channel and the position was then further adjusted to where the OFI signal exhibited the highest frequency (Fig. III.15), so that the measured velocity V_{flow} is actually V_{max} that is linked to the flow rate (controlled by the syinge pump) through Poiseuille's law ($V_{\text{max}} = \frac{2Q}{S}$).

Doppler spectra were recorded at different fluid flow rates Q from 0 to 50 μL.min^{-1}. As shown in Fig. III.5.1, the Doppler spectrum shifts and widens with the flow rate. In addition, the peak exhibits a well defined Gaussian shape.

III.5.2 Signal processing

To calculate accurately the measured velocity V_{max}, the average Doppler frequency within the sensing volume was extracted from the OFI signal spectrum using the following fitting function:

$$af^{-b} + c + d \exp \frac{-\left(f - f_{\text{peak}}\right)^2}{h} \qquad (\text{III.22})$$

where a, b and c are the fitting parameters depending only on the experimental set-up. Thus, a and b in the first term are the parameters used for fitting the Flicker noise, and parameter c in the second term is used for fitting the broadband noise in the spectrum. In the last term of the fitting function, d corresponds to the strength of the Doppler peak. The parameter h is related to the FWHM of the peak, knowing that FWHM$\approx 2.354h$. The parameters d, h and f_{peak} depend on the electro-optical system design, as well as on the reflectivity and the number density of particles, the fluid velocity, and the velocity distribution within the detection volume. The parameter f_{peak} represents the fluid velocity at the measurement point.

The frequency of the Doppler peak as a function of V_{max} is shown in Fig. IV.3.1.b. The flow rate Q is directly proportional to the Doppler peak. The angle between the flow direction and the optical beam can be estimated from the slope of this curve using Eq III.21, and has been calculated to be 80.25 °. The behavior of the sensor concords with the model described in Section III.3

III.5.2.a   Error measurement and repeatability in single scattering regime

The purpose of the OFI sensor is to provide reliable measurements. Therefore, we investigated the performance of the sensor in the following configurations:
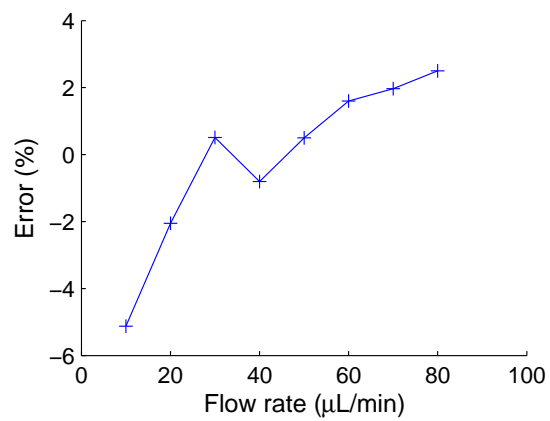
Figure III.17: Mean measurement errors to the theoretical values.
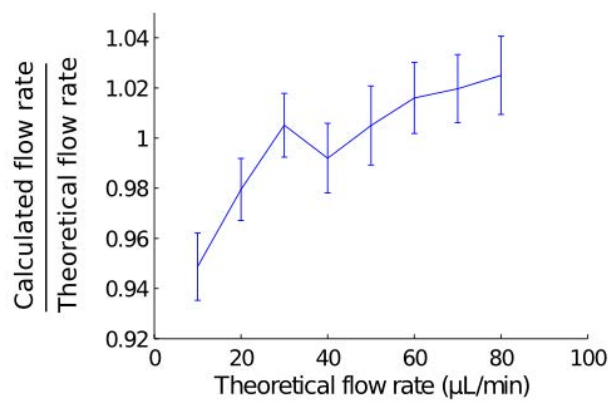
Figure III.18: Theoretical and calculated pumping rate in single scattering regime, standard deviation for 8 consecutive scans.

- **Accuracy:** The theoretical and measured velocities are compared for several flow rates.

- **Reliability:** 8 consecutive OFI signals were acquired at a constant flow rate, and the calculated velocities are compared.

The OFI flowmeter operated under the same conditions as in Subsection III.5.1, described in Table III.4.

Accuracy: The difference between the experimental and the theoretical velocities is plotted in Fig. III.17. The relative error for each measurement point was less than 2 %. The highest error is observed for high pumping rates ($Q > 60$ µL/min), and can be explained by difficulties in identifying the position of the Doppler peak's maximum. For theses pumping rate, the spectrum widens and its amplitude decreases, affecting the signal-to-noise ratio. Therefore, a small perturbation due to noise in the Gaussian's shape can lead to wrong fitting parameters.

Repeatability: To estimate the repeatability of the measurement, the standard deviation over 8 consecutive scans was calculated for each measurement point. The results are displayed in Fig. III.18. In addition to the increase of the error observed in the previous paragraph, the sensor shows a compromised repeatability for high flow rates. The discrepancy observed at high particle velocities can be also explained by difficulties in extracting the Gaussian peak from the broadband noise. Notwithstanding the two last points (with a discrepancy of 3.1 % and 4.2%), the relative error for each measurement point was less than 2.5 %.

III.5.3 Limits

On its current implementation, the OFI sensor for fluidics applications is efficient in a certain range of velocities.

III.5.3.a Lower limit

The measurement of low velocities is mostly limited by the low-frequency noise induced by the laser diode. The lowest Doppler peak that could be extracted from the noise curve was located near 100 Hz. For a laser emitting at 667 nm, an aqueous liquid phase (n=1.33), and an angle between the laser and the flow direction θ of 70 °, the minimum measured velocity would be 70 µm/s, according to Eq. (III.21). Using a high θ will reduce this limit, but at the same time the SNR, as less light is reflected for large angles (Mie theory). Kliese et al. [150] proposed to use a blue laser ($\lambda = 405$ nm) to measure velocities below 30 µm/s. The LD injection current can also be
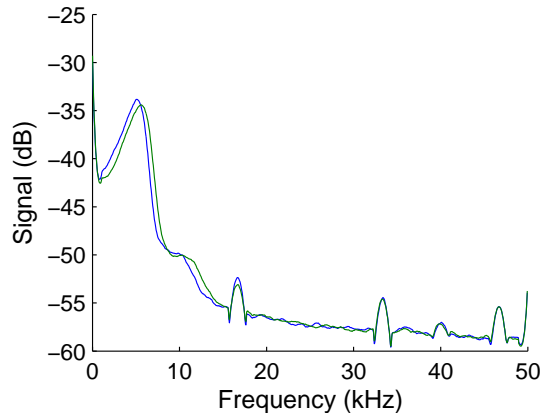
Figure III.19: OFI spectra for fluid velocity of 7.4 mm/s and 8.2 mm/s

modulated using a sawtooth-like function, as described in Section II.5, in order to shift artificially the Doppler peak towards higher frequencies.

III.5.3.b   Upper limit

The measurement of high velocities is limited by the amplifier bandwidth (600 kHz). For a laser emitting at 667 nm, an aqueous liquid phase (n=1.33), and an angle between the laser and the flow direction θ of 85 °, the maximum theoretical velocity would be 1.7 m/s. In experimental conditions, velocities up to 0.8 m/s can be accurately measured.

III.5.3.c   Velocity resolution

The velocity resolution is limited by the width of the Doppler spectrum that should be narrow enough so that two Doppler peaks can be discriminated one from another. Consequently, the resolution strongly depends on the measured velocity, the size of the channel with respect to the measurement volume, and the efficiency of the optical set-up to provide a narrow and circular beam. In single scattering regime and under the experimental configuration described in Subsection III.5.1, we could differentiated two velocities with a precision of 0.8 mm/s. Two spectra exhibiting a Doppler peak located respectively at 5127 Hz and 5664 Hz are plotted in Fig. III.19. The measured velocity are respectively 7.4 mm/s and 8.2 mm/s. OFI sensor provides a good velocity precision, that can be meliorate by adjusting the experimental set-up (optical system, LD model, LD wavelength) to decrease the Doppler peak width.
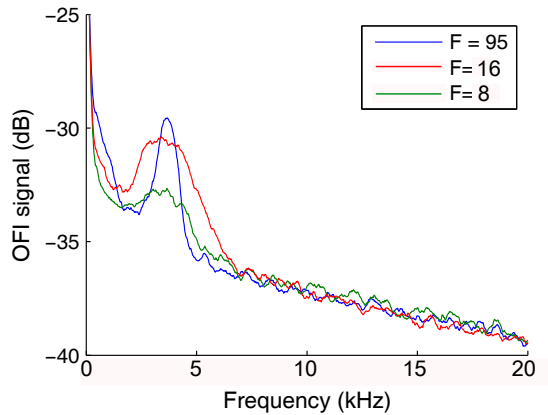
Figure III.20: OFI spectra for various optical set-ups (single lens scheme).

III.6   Sensing volume effect

III.6.1   Dual-lens optical set-up

For microfluidics applications, the sensing volume requires to be precisely controlled. It has been observed that a narrow Gaussian-shaped sensing volume provides good results for local velocity measurement.

The OFI flowmeter described in Fig. III.4.5 is built in such a way that the optical set-up is easily interchangeable. Changing the optical system leads to two effects:

- The sensing volume size changes. Consequently, the widening of the Doppler peak observed for some configuration can be due to the sampling of broader velocity distributions.

- Increasing the numerical aperture (NA) or decreasing the focal length (f_c) of the second length allows it to capture more light, affecting also the shape of the Doppler peak. The F-number concept puts these two together to allow a quick comparison of optics, and is defined by $F = f_c/\text{NA}$ for parallax approximation.

To decorrelate these two effects, we measured the velocity distribution in a large flowchannel (detailed in Section IV.2). Knowing that the three optical set-ups tested provide sensing volume on the order of tens of micrometer, and that the smallest dimension of the flowchannel is 3 cm, it can be assumed that the variation of velocity sampled by the sensing volume can be considered neglectable.

To investigate the influence of the numerical aperture and the focal length of the optical set-up on OFI signal, several lenses described in Table III.2 were mounted in dual-lens configuration. In this configuration, the first lens is close to the LD output facet, whereas the second lens is the one that focus the laser beam into the fluid. OFI signals were acquired for various second lenses (C240, f_c=8 mm, C230, f_c=4.51 mm and C260, f_c=15.29 mm), the first lens was a C240. Theother experimental conditions are those described in section IV.2.

We acquired the OFI spectrum at a constant flow rate (Q=20 μL/min) for every optical configuration, and the results are presented in Fig. III.20. It can be observed that the magnitude of the Doppler peak, as well as the FWHM vary with the optical configuration. This can be explained by the fact that a small F-number collects more light than a large one. Assuming that the spectral width of the distribution about the Doppler peak is dependent on the range of angles that are coupled into the laser or the equivalent F-number of the optical set-up, it can be deduced that a lower F-number leads to a narrower Doppler frequency distribution and a higher SNR. However, this investigation requieres further study with dedicated experimental set-up.

Despite our efforts, this experimental protocol led to several difficulties. The laser beam had to be focused at the same location for every optical configuration, in order to sample the same velocity distributions, and the experimental conditions have to be consistent throughout the entire measurement session. To minimize the effect of a change in the velocity value on the OFI spectrum's shape, the sensing volume position was adjusted in the center of the flowchannel (highest velocity) by scanning the flowchannel two dimensions, until the Doppler peak was located at the highest frequency.

III.6.2 Single-lens optical set-up

In microfluidics applications, the flowchannel typical size can reach the micrometer range, leading to a sensing volume larger than the flowchannel itself. The same phenomenon can be observed when the optical system enlarges the sensing volume (single lens or lensless configuration). In such case, the whole range of velocities distributed in the channel is measured. The single-lens sensing scheme can be really interesting though, as it reduces drastically the cost and the complexity of the sensor.

For that purpose, smaller squared flowchannels 100 x100 μm have been manufactured in PDMS (See Appendix D), and have been filled with milk diluted in water (2 %). The other parameters are described in Table III.5.The assembled optical head was characterized with a beam profiler, and the spot

Parameter	Numerical values
Flowchannel	square cross-section (100 μmx100 μm)
Liquid	Milk-water (2%-98%)
Refractive index	1.34
Lens 1	C240 (f=8 mm)
θ	75°
LD driving current	1.8 mA
LD wavelength	667 nm

Table III.5: Parameters used for OFI measurement in single scattering regime, and single lens configuration

diameter in focus was measured to be 32.26 μm. The total distance between the LD output facet and the flowchannel was set at 10 cm. The magnification of the lens (C240-TMEB, $f_c = 8$ mm) was 10.5, leading to a theoretical output beam diameter of 339 μm, providing a poor spatial resolution.

Fig. III.6.2 is a plot of Doppler spectra recorded for flow rates Q varying from 0 to 10 μL.min^{-1}. The Gaussian peak presented in the previous paragraph cannot be recognized any more, and the fitting function described in Eq. (III.22) cannot be implemented. The signal shape is crenel-like, because all velocities from 0 (wall velocity) to $V_{\max}$ are represented in the frequency spectrum.

However, it can be observed that the maximum frequency of the spectrum is directly proportional to the flow rate of the liquid in the tube. Also, the signal level decreases when the flow rate of the liquid increases. This is due to the fact that the same amount of light is coupled into the laser for different flow rates, the OFI signal being distributed over a wide frequency range.

In such case, the Doppler frequency within the sensing volume is extracted from the OFI signal spectrum using the following fitting function (Fig. III.22):

$$af^{-b} + c + \frac{d}{exp(\frac{f-e}{g} + 1)} \qquad (III.23)$$

where a, b and c are the fitting parameters depending only on the experimental set-up. Thus, a and b in the first term are the parameters used for fitting the Flicker noise, and parameter c in the second term is used for fitting the broadband noise in the spectrum. In the last term of the fitting function, d corresponds to the horizontal straight line magnitude, the decreasing slope of the OFI spectrum being represented by e/g. The cut-off frequency, which is the frequency associated with the magnitude 3 dB lower
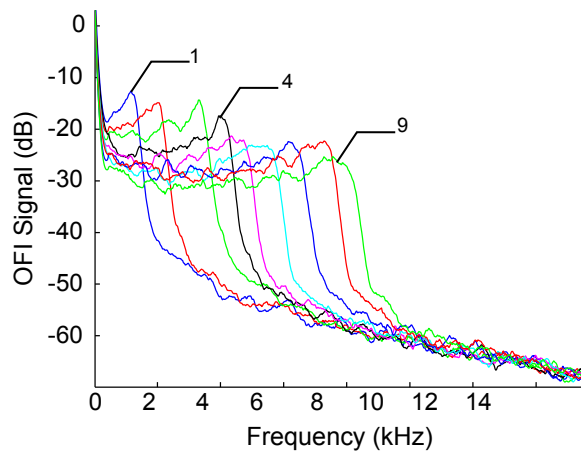
(a)
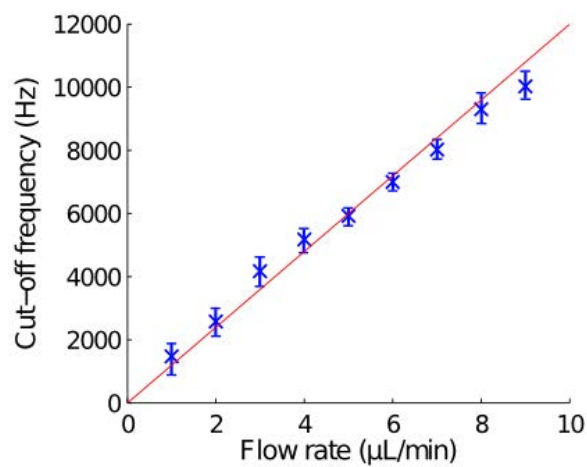
(b)

Figure III.21: (a) OFI Doppler spectra for several flow rates ([0:1:9] µL.min^{-1}) (b) Plot of the cut-off (-3 dB) frequency as a function of the maximum flow velocity calculated from the flow rate Q. The cut-off frequency shows a linear relationship with the pumping rate.
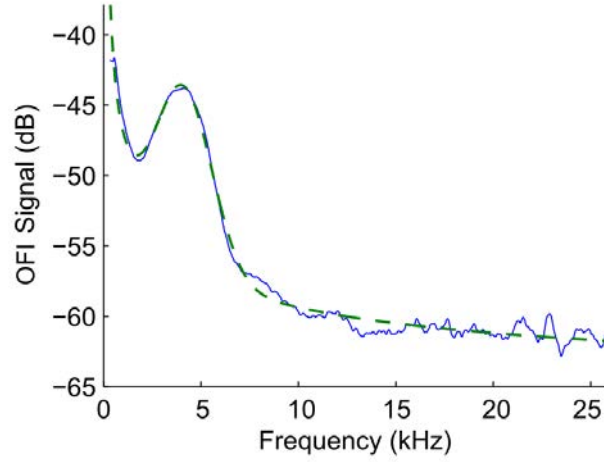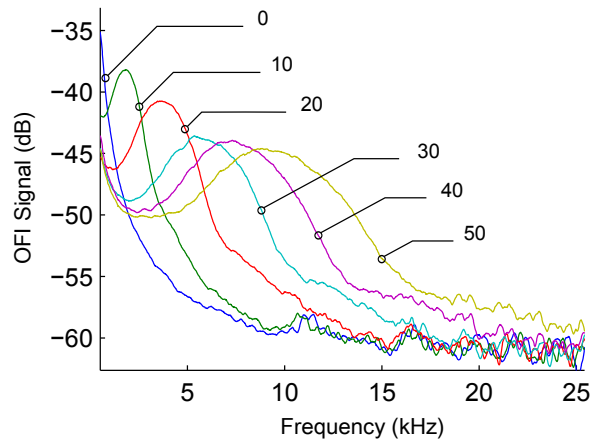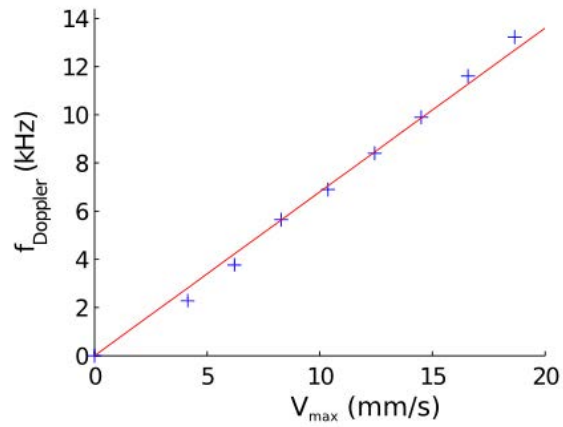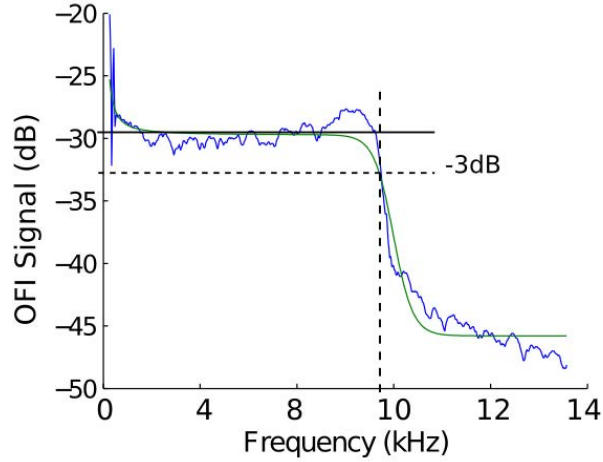
Figure III.22: OFI signal in frequency domain measured in the entire channel and the corresponding fitting curve (Eq. (III.25)). The mean frequency in the sensing volume is calculated by extracting the cut-off frequency of the signal

than the plateau, is linked to the maximum velocity in the flowchannel using Eq. (III.21).

To recover a linear relationship between the flow rate Q and the OFI signal, the average Doppler frequency within the sensing volume was extracted from the OFI signal spectrum using Eq. (III.23), and the 3 dB cut-off frequency was calculated (Fig. III.6.2). The standard deviation over 6 measurements has been calculated, and was found lower than 8 %. As a matter of fact, the measurement session was less repeatable than in dual-lens configuration, as the fitting function may not be appropriated enough to the signal shape. A small perturbation in the signal's shape can lead to wrong fitting. Nevertheless, performing a calibration of the sensor and averaging numerous measurements can reduces this error. Although this configuration is not optimum for microfluidics applications, it enables to evaluate quickly velocities changes.

III.7   Effect of particle density

III.7.1   Lower particles density reached

A great advantage of OFI over other sensing techniques may lie in its extreme sensitivity, as a very small amount of particles travelling in the sensing volume generates a detectable signal. For the OFI configuration described
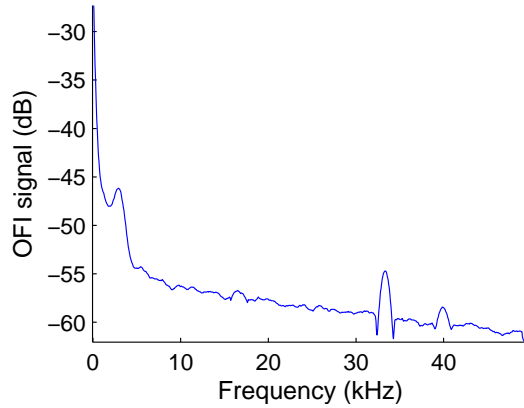
Figure III.23: OFI spectrum measured for a particle density of approx. 26 g/L. As a matter of comparison, undiluted milk leads to SNR higher than 30 dB.

in Table III.5.1, we could acquire a measurable signal for a milk particle concentration of 0.2 %. Knowing that milk contains approximately 130 g/L of fat particles, the minimum detected particle density for this size of particle, and for our specific set-up, is 26 g/L. The OFI spectrum for such a small quantity of particle is depicted in Fig. III.23. This limit depends on the particle refractive index and cross section, and on the noise induced by the circuitry and the LD. Although no further investigation has been performed, and that these results are applicable to a specific configuration, it paves the way for the design of dedicated sensor to detect very small amount of particles in aqueous phase. As a matter of fact, sensitive and rapid detection of small particles in a fluid flow is needed for many applications, such as the production of pharmaceuticals and semiconductor equipment, conservation of water quality, and marine science.

III.7.2 Effect of an increase of particles density

As demonstrated theoretically in section III.2, the density, the size and the particle refractive index contribute to the magnitude of the Doppler peak. We measured the OFI signal in single scattering regime for various concentration of milk particles diluted in water, flowing at a constant flow rate (Q=40 µL/min). The results are plotted in Fig. III.24. It can be observed that the signal increases with the particles concentration, as more light is backscattered, and therefore reinject in the LD cavity. Based on this result, one can think that fluids with a higher particle density will benefit of a much better accuracy and reliability due to the higher SNR. However, with particle concentration increase the OFI spectrum changes drastically because of the presence of isolated multiple scattering events, thus affecting the signal
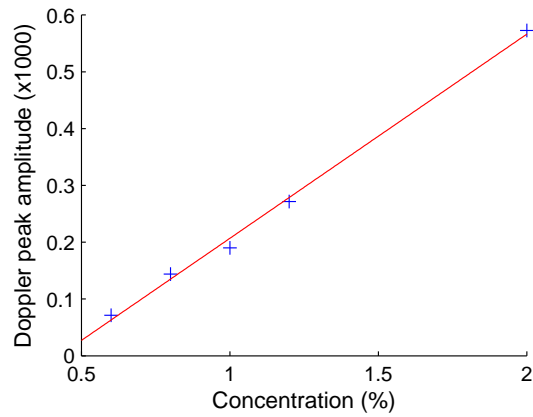
Figure III.24: OFI efficiency as a function of the particle concentration in single scattering regime.
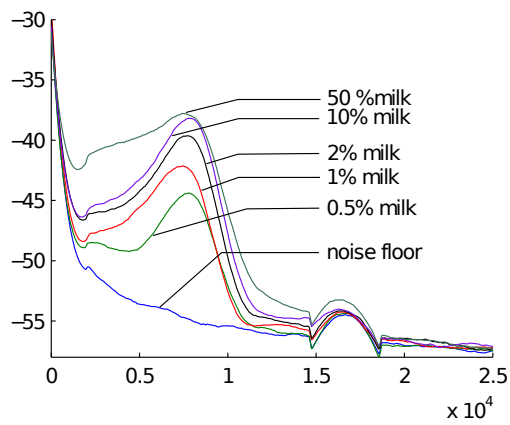
Figure III.25: OFI spectra for various milk to water ratio. The magnitude of the Doppler peak increases with particle concentration

104

processing (Fig. III.25).

For microfluidics applications, we employed particle concentration between 1% and 10% to guarantee single scattering regime and sufficient OFI efficiency.

III.7.3 Extraction of the flow rate with high particle density fluids

When the density of scatterers is high, the probability that a photon will be scattered multiple times is high and the regime is called "multiple scattering". The signal in pure multiple scattering regime can be easily identified. The spectrum does not show a single frequency peak but a monotically decreasing frequency distribution because each photon interacts with several particles, thus undergoing several Doppler shift [141,143]. In addition, when the particle density is high, the light is quickly absorbed while travelling in the liquid. Consequently, as light penetrates more deeply into a liquid, the amount of scattered light returning to the laser will decrease, and the frequency contribution coming from deep areas will be attenuated. Despite the fact that Monte Carlo methods [242–244] or analytical models [245–247] have been developed to describe scattering by multiple particles for LDV, this phenomenon remains complex in OFI flowmetry.

Based on the analysis of Bonner and Nossal [247] for the traditional LDV applied to multiple scattering in liquids, the following problems may be encountered in OFI applied to turbid liquids:

- The location and number of scattering events is unknown

- Only a very small portion of the light incident will penetrate very deeply and return to the surface, the sensing information is mostly the surface velocity.

- The idea of Gaussian beam, laser spot and focus are not valid any more. Therefore, the spot size and position cannot be monitored as easily as for single scattering regime.

- The scattering angles and the average path length in the liquid are unknown.

- The OFI spectrum for multiple scattering represents a statistic distribution of what happen in the unknown sensing volume, thus there is no analytical formula that link one parameter of the spectrum to the average velocity in the spectrum.
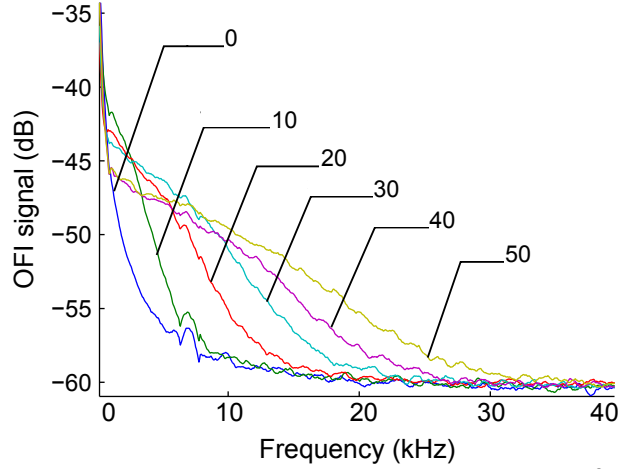
Figure III.26: OFI spectra in multiple scattering regime for flow rates of [0, 10, 20, 30, 40, and 50] µL/min

Parameter	Numerical values
Flowchannel	circular cross-section (diameter = 320 µm)
Liquid	Milk
Refractive index	1.45
Lens 1	C240 (f=8 mm)
Lens 2	C240 (f =8 mm)
θ	75°
LD driving current	1.8 mA
LD wavelength	667 nm

Table III.6: Parameters used for OFI measurement in multiple scattering regime

Multiple scattering regime signal processing is not straightforward. For in-vitro microfluidics applications, single scattering regime can be guaranteed by controlling the seeding concentration. However, for most in vivo applications, the density of particles is high enough so that multiple scattering cannot be ignored any more. For further informations, signal processing in multiple scattering regime has been studied by several research groups [133, 141, 143, 242].

III.7.3.a   Experimental arrangement for multiple scattering regime

OFI signals in multiple scattering regime were acquired using the experimental set-up described in Section III.3, under the conditions described in Table III.6. To obtain multiple scattering behaviour, the flowchannel was

filled with non-diluted milk (Regilait). As for single scattering regime, the signal was sampled at the center of the circular flowchannel, where the local velocity is supposed to be maximal. The position of the laser beam focus and angle θ were adjusted to maximize the SNR and minimize the specular reflection of the tube wall. Doppler spectra were recorded at different fluid flow rates Q from 0 to 90 µL.min^{-1} and are plotted in Fig III.26.

We proposed here three methods to extract a relationship between the OFI spectrum and the flow rate Q, imposed by the syringe pump.

III.7.3.b   Method 1: Broadening of the OFI spectrum

The first signal processing method to be implemented is a numerical estimation of the half-width half-maximum (HWHM) of the semi-log OFI spectrum.

The power spectrum was fitted using the following function F_1:

$$F_1(f) = af^{-b} + c + \frac{d}{1 + \frac{f^2}{f_0^2}} \qquad \text{(III.24)}$$

Where a, b and c are the parameters described in Eq. (III.22), and the frequency constant of the fitted curve, f_0, is used to quantify the broadening of the spectra. An example of fitting using this method is presented in Fig. III.7.3.b.

This method has then been applied to the spectra from Fig. III.26, and the parameter f_0 is plotted as a function of Q in Fig. III.7.3.b. The distribution broadens as the flow increases and can be well described by F_1 with a semi-logarithmic scale. The parameter f_0 varies proportionately with the flow rate. The standard deviation over 6 consecutive measurements has been calculated to be 8.7%.

Nevertheless, this algorithm shows two major drawbacks: First, it requires a complex elaboration for the computation of the regression curve, which could be difficult to be implemented in a low-cost embedded system. Moreover, this method is too sensitive to small fluctuations and noise in the low-frequency range, where the signal amplitude is maximal; a signal fluctuation in this spectral region can induce a strong error in the automatic regression curve estimation. However, this method shows a very good linear relationship between the pumping rate and the parameter f_0.
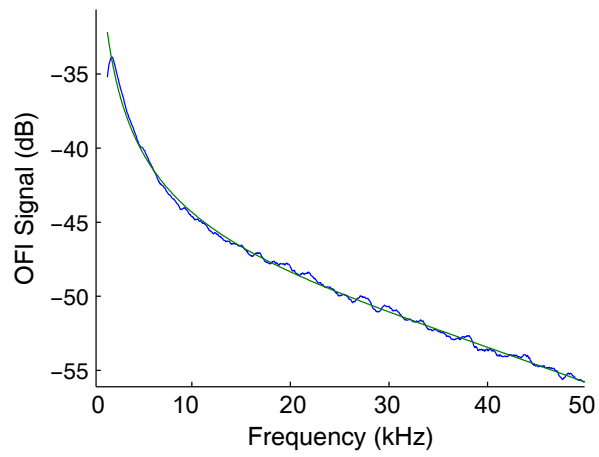
(a)
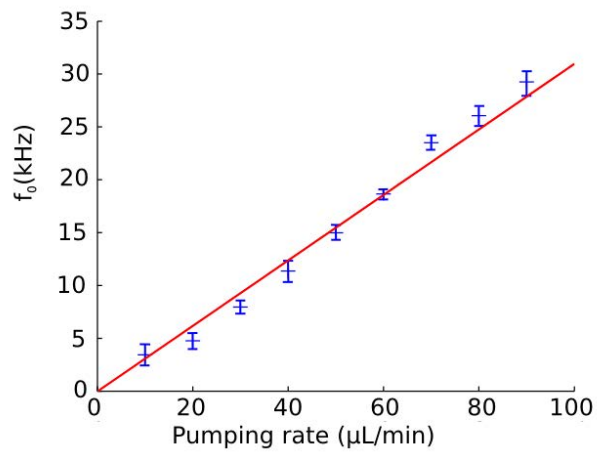
(b)

Figure III.27: (a) OFI spectrum in multiple scattering and its corresponding fitting curve (b) Plot of the fitting parameter f_0 as a function of the pumping rate Q

108
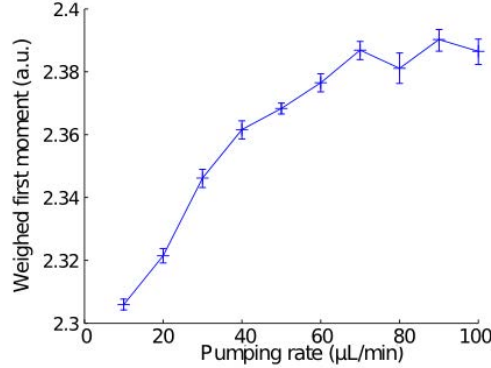
Figure III.28: Plot of the first weighed moment as a function of the pumping rate Q.

III.7.3.c   Method 2: Statistical moments

The measured Doppler spectrum can also be considered as a probability density function of the velocity distribution for the particles suspended in the fluid. Bonner and Nossal [247] proved that the first weighted moment of the spectral power density S(f) is linearly proportional to the average velocity of all moving particles in the optical sample volume.

$$\overline{f} = \frac{\int_{-\infty}^{\infty} fS(f)df}{\int_{-\infty}^{\infty} S(f)df} \tag{III.25}$$

The numerator which is the first unweighed moment of the spectral power density is assumed to be proportional to the flow in the optical sample volume. The denominator is proportional to the total amount of Doppler-shifted light.

This method has then been applied to the spectra from Fig. III.26, and the estimated parameter $\overline{f}$ is plotted as a function of Q in Fig. III.28. For low velocities, $\overline{f}$ varies linearly with the pumping rate, but the proportionality is lost for higher pumping rate. This can be due to the presence of electronic noise in higher frequency that may interfere with the OFI spectrum at high flow rate. Furthermore, over 6 consecutives measurement, the average standard deviation have be calculated to 11.2%, that is much higher than for single scattering regime.

This algorithm is simpler and very rapid compared to the fitting method, because it requires only two sums on the previously calculated FFT spectrum. The power spectrum, however, does not represent exactly the veloc-

ity distribution of the particles, because the contribution of each particle is weighted by the level of its back-injected optical power. Furthermore, the noise fluctuations induced by the electronics lead to wrong calculations. To get rid of this problem, a simple solution consists in proceed in two steps. First, the OFI spectrum is fitted using Eq. (III.24), then Eq. (III.25) is applied. Although this solution is time and memory consuming, proceeding in two steps minimize the inaccuracies due to noise fluctuations, and provides a better accuracy than the method 2 used on its own.

III.7.3.d   Method 3

An alternative signal processing method is based on the hypothesis that frequency contributions can provide from two scattering processes: a pseudo first order backscattering process, where incident photons have been backscattered a single time from the focus point area, and a multiple scattering process, where photons have been scattered from multiple particles. To increase the channel size or the particle density will increase the influence of the second process. However, in microfluifidics, one can assume that the probability of the first process to occur is high enough, so that it possible to calculated a pseudo-single-scattering Doppler frequency that can be linked to the flow rate.

A noise spectrum is first acquired by focusing the sensor on the channel filled with static milk particles. Then, the liquid is pumped and OFI spectra are acquired under the conditions described in Table III.6. The noise power spectrum is subtracted to the OFI spectra, and the resulting curve is fitted using a log-normal distribution:

$$F_2(f) = \frac{1}{\sqrt{(2\pi)}\sigma f} exp(-(\frac{\log(f-\mu)^2}{2\sigma^2})) \qquad \text{(III.26)}$$

Where μ and σ are respectively the mean and standard deviation of the signal.

In addition, the following fitting function can also be employed:

$$F_3(f) = a\sqrt{f-c}\exp(-b(f-c)) \qquad \text{(III.27)}$$

Where a, b and c are parameters adjusted to minimize the error between the OFI signal and the fitting function F_3, using a least-mean square algorithm.

An example of fit using this method is presented in Fig. III.7.3.d. The frequency of the signal's maximum is recorded, and used to describe the evolution of the OFI signal with the flow rate. This maximum position, noted f_{pseudo}, represents the most represented frequency contribution, and depends on the focus point (i.e. the point where the laser intensity is maximum) coupled with the scattering event occurring the most often. In microfluidics, we

110
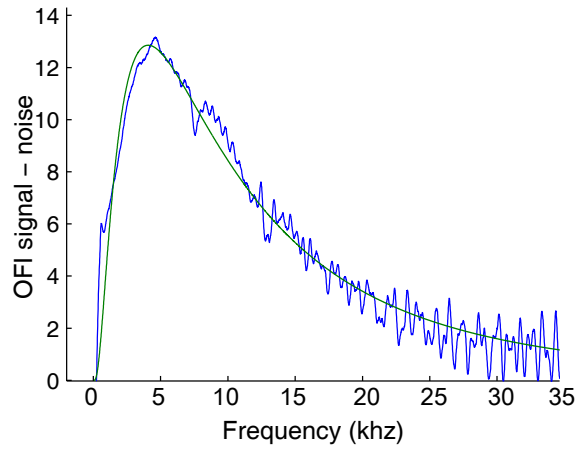
(a)
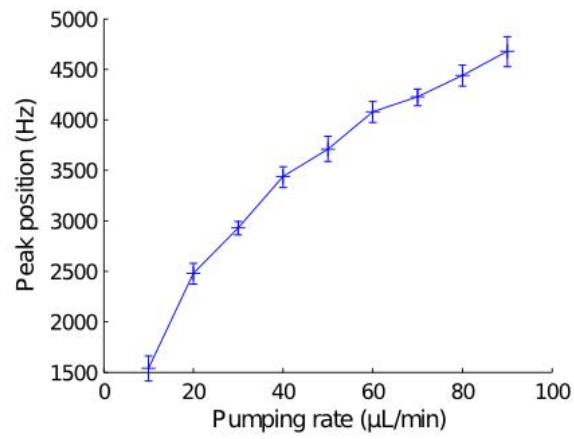
(b)

Figure III.29: (a) Noise curve subtracted to the OFI spectrum in multiple scattering and its corresponding fitting curve using log-normal distribution (b) Plot of the fitting parameter f_{pseudo} as a function of the pumping rate Q

Method	Accuracy	Robustness	Temporal resolution
Method 1	++	-	- -
Method 2	-	+	++
Method 3	++	+	-

Table III.7: Comparison of signal processing methods for flow rate measurement in turbid liquids

believe that the most represented scattering event is a single backscattering event.

This method has then been applied to the spectra from Fig. III.26, and the parameter f_{pseudo} is plotted as a function of Q in Fig. III.7.3.d. f_{pseudo} shows an increasing trend with respect to Q. In addition, over 6 scans, the average standard deviation is 10.1%. The flow dependence of the parameter f_{pseudo} seems to corroborate the idea that this parameter can be used to describe multiple scattering signals in microchannels. The advantages of the pseudo-single-scattering signal processing method is that there is no influence of the electronic and optic noise, as the noise spectrum is subtracted in a first step. The fitting is less time-consuming and relatively robust (i.e. less affected by intensity fluctuations) than the first method. However, this method may not be accurate for large channels, or in strongly scattering tissues.

III.7.3.e Signal processing comparison

Table III.7 compares in a glance the three signal processing methods for multiple scattering flows presented in this section. Obviously, the choice of a signal processing method is specific to the application of the sensor. For rapid tracking of flow changes, as for example blood flow rate monitoring, we may want to use the second method, based on changes in the first weighted moment of the spectral power density. This method provides almost real time quantitative measurement, and does not require any fitting algorithm. Therefore, it can be easily embedded in a small chip to be included in movable OFI sensor for in-vivo applications. However, for precise measurement of flow distribution in microchannel, this method lacks of precision, as any disturbance in the spectrum affects the calculated flow rate. This is especially true for noisy electronic sensors, where the presence of an electronic peak in frequency domain can drastically affect the flow rate measurement. In the worst cases, the magnitude of this parasitic signal can hide small OFI signal variations. The first and the third methods are based on the fit of the OFI spectrum and provide a linear relationship between the flow rate and a fitting parameter. These methods are more accurate, and show a better repeatability. Furthermore, the sensitivity of these methods that

monitor changes in the OFI spectrum shape are higher than the moment method that measure a global variation. Consequently, they are suitable for the measurement of flow velocity distribution in microchannels. The third method is a improved version of the first one, as the noise is taken into account by being subtracted to the OFI signal. Therefore, the fitting algorithm is only applied to the useful signal, reinforcing the signal processing robustness. Moreover, it employs less fitting parameters, leading to a faster signal processing. To put it in a nutshell, the weighted moment method is more indicated for rapid flow rate changes monitoring, whereas for accurately velocity profile reconstruction, one may employ fitting methods with a preference for method 3.

Multiple scattering is still not well understood, and various signal processing methods have been presented in the previous section. An additional idea has been studied for LDV which also suffer from multiple scattering issues. It consists in suppressing the contributions of multiple scattered light. The principle is to acquire from the same focus point two signals from two sensors (or two wavelengths), and to plot the cross-correlation function. As multiple scattering contributions suffer from a random uncorrelated statistical process, only the single scattering contributions should be common to the two signals. This technique has been extensively studied by Schätzel's research group [248].

A compromise has to be found between accuracy and signal processing time. As our purpose is to build a low-cost embedded system, we will have a preference for the weighted moment method that is susceptible to provide almost real-time results. For biomedical applications, where multiple scattering cannot be avoided, a quantitative analysis of the blood flow is sufficient to understand most of the pathologies (burn assessment, blood rate increase etc..). For in-vivo or microfluidics applications, the particles concentration can be optimized to remains in single scattering regime.

III.8   conclusion

The need of accurately measure flow rate in flowchannels is well recognized, and OFI offers a rapid, direct, non-invasive and high-resolution alternative for determining flow rate within flowchannels. In this chapter, OFI three-mirror cavity model have been applied to fluid flow rate measurement, allowing a good understanding of the observed signals. An experimental set-up, based on a commercial semiconductor VCSEL, has been designed to achieve micrometer range spatial resolution. The sensor performances have been studied and validated for single scattering and multiple scattering regime. Finally, the effects of experimental conditions on OFI signal have been in-

vestigated.

Chapter IV

OFI flow profile measurement in microchannels

IV.1 Introduction

In the previous chapter, we demonstrated that OFI offers a simple, rapid and low-cost alternative to measure flow rates in sub-millimeter channels. However, one of the basic components in Hydraulics is the understanding of the velocity distribution in channel, which is of great interest to provide better understanding of fluidic transport, as well as mixing and fluid properties. As a matter of fact, the velocity distribution varies locally and spatially depending on the type of channel (straight, steep, bends, meandering, etc...) and the flow (uniform, non-uniform, laminar, turbulent). Currently, micro particle imaging velocimetry (μ-PIV) is the most advanced technique for obtaining accurate measurement of velocity distribution in sub-millimeter channels [6, 106, 249]. However, this kind of sensing technology is quite complex, time-expensive and bulky. The aim of this chapter is to explore whether OFI can be an interesting alternative for flow profile measurement in microchannels.

IV.2 Flow profile measurement in macrochannels

IV.2.1 Context

To validate the sensor develloped for flow rate measurement, we first measured the velocity distribution in a centimeter-range fowchannel. Under these conditions, the velocity variation over a micrometer area can be considered as negligible, thus minimizing experimental errors. Once the sensor perfomance are validated with this setup, we can try to measure velocity distribution in sub-millimeter channels, where the velocity variation over a micrometer area is large, and where a small misalignement in the sensing volume can lead to large measurement errors.

IV.2.2 Experimental set-up

Fig. IV.2.2 shows the dimensions of a custom made diverging-converging planar flow-channel, which is 3 mm deep and 21 cm long. A microscope cover slip of 160 μm thickness is employed as the top window sealing cover. It has been designed at the ITEE of the University of Queensland. The fluid flow distributions were simulated using fluid parameters of water at room temperature. The simulations were performed using the commercial computational fluid dynamics package, CFD-ACE+ from ESI-Group. The results provide 3-D distribution of the velocity vectors for points within the flow channel on a fine hexahedron structured grid containing 30, 292 and 31 points in the x, y and z directions respectively.

The width of the custom channel changes so that the average velocity increases along the centerline profile, and shows a parabolic velocity distri-
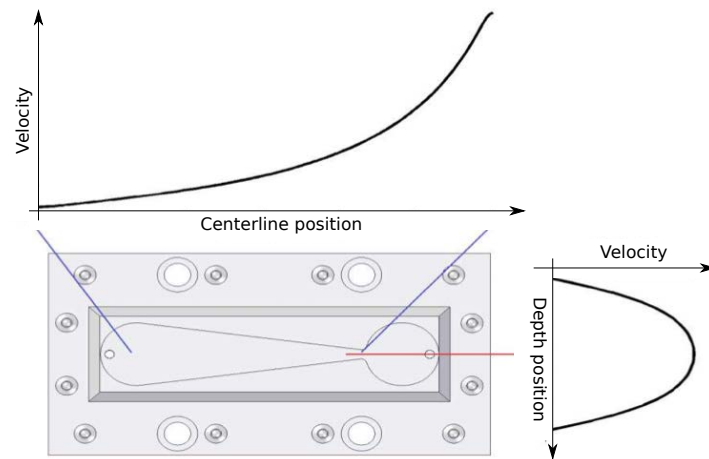
(a)

(b)

Figure IV.1: Macrochannel manufactured at UQ (a) Drawing and theoretical velocity distribution (b) Photography of the custom macrochannel

117
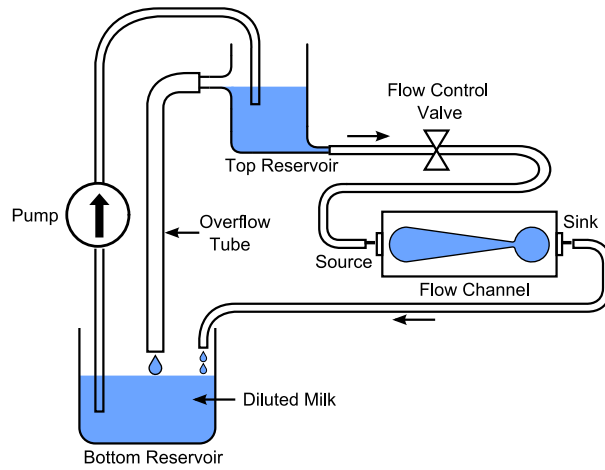
(a)
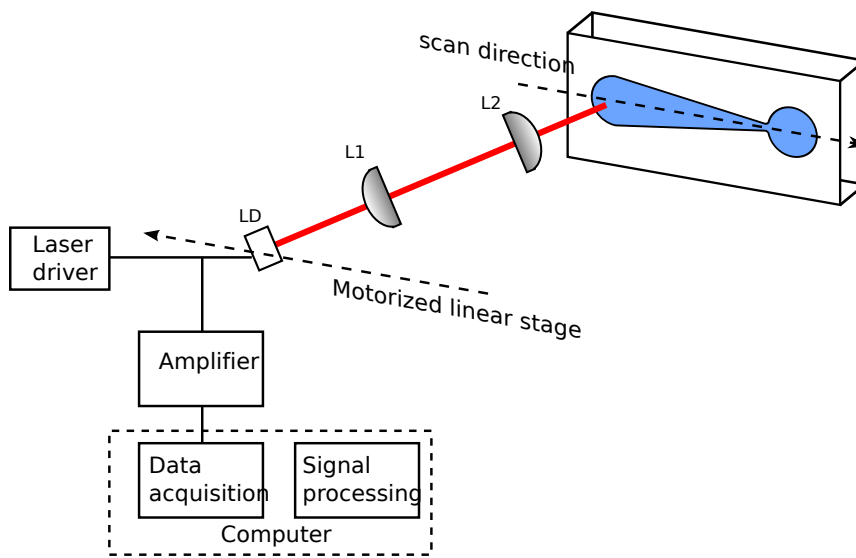
(b)

Figure IV.2: (a) Fluidic arrangement controlling the average flow rate (b) OFI experimental setup

Parameter	Numerical values
Flowchannel	custom (see Fig. IV.2.2)
Liquid	Milk (2 %)- Water (98 %)
Refractive index	1.33
Lens 1	C240 (f=8 mm)
Lens 2	C240 (f=8 mm)
θ	80°
Flow rate	Q=15mL/min
LD	Gigalase 8185-1100
LD driving current	4 mA
LD wavelength	850 nm

Table IV.1: Parameters used for flow profile measurement in macrochannels

bution along the depth profile.

Diluted milk was pumped through this flowchannel using a Waston-Marlow peristaltic pump. To keep the flow rate constant, a fluidic arrangement made of two reservoirs have been designed and is drawn in Fig. IV.2.2). The averaged flow rate ($Q = 15$ mL/min) was determined by measuring the amount of liquid passing through the channel in a given time period.

A multimode VCSEL (EMCORE Corporation, Gigalase 8185-1100) emitting at 850 nm was fixed to a goniometer, used to control the angle of the laser beam with respect to the flow direction. The entire optical head was mounted on a motorized optical rail (Zaber, T-LSR300A-KT03) controlled by LabView. The optical system consists in two lenses, allowing a sharper focus into the flowchannel. The experimental set-up is depicted in Fig. IV.2.2, and the experimental conditions are summed up in Table IV.1.

IV.2.3   Flow profile results

IV.2.3.a   Centerline profile

First, the laser was aligned along the centerline of the flowchannel close to the entrance of the diverging section. Special attention was paid to the beam alignment, so that the flowchannel was exactly parallel to the translation stage. Then, the sensing volume position was adjusted in depth, by focusing the laser beam in the middle of the flowchannel, where the OFI spectrum exhibited the highest Doppler frequency. Finally, the laser beam was moved along the centerline of the channel, by 0.8 mm steps towards the channel exit. Ninety measurement points were acquired using a data acquisition card (National Instruments 16-bit data), and for each point, 36
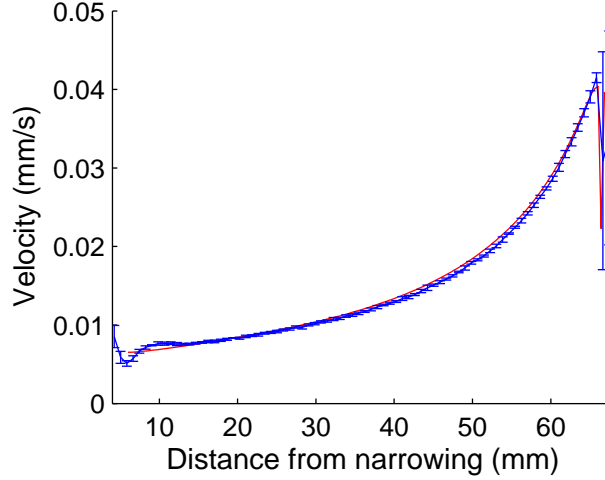
Figure IV.3: Plot of 8 successive profiles and comparison with theory (red curve). The solid blue curve corresponds to the mean velocity at each measurement point, whereas the errorbars illustrate the standard deviation over 8 measurements.

successive spectra were averaged and processed in LabView. Once the FFT performed, the Doppler frequency was extracted from the OFI spectra using Eq. III.22.

The parameter f_{peak} represents the fluid velocity V at the measurement point using Eq (III.21).

We first processed the data using the experimental parameters described in Table IV.1, and noticed that the measured velocities were smaller than the theoretical one. Although the angle θ has been adjusted to 80 °, the measured profile fitted perfectly to the theoretical one using $\theta = 81.9°$. There are several reasons that can induce this large error. First, the average flow rate was manually obtained by measuring the amount of liquid flowing through the channel during three minutes using a graduated beaker. The glassware graduation reading as well as the complicated tubing and flow transport apparatus can lead to inaccuracies. Furthermore, the laser can be tilted and misaligned in the center of the laser mount, causing the optical path to be deviated. In addition, the optical head is angled at θ with respect to the channel's top glass, but the difference of refractive index leads to a deviation of the optical beam in the liquid. Finally, some experimental parameters can fluctuate because of temperature changes (laser wavelength), leading to variations in the measured Doppler frequency. As the flow profile measurement was repeatable (Fig. IV.3), we decided to use $\theta = 81.9°$ to calculate the measured velocity. The results show good agreement with the
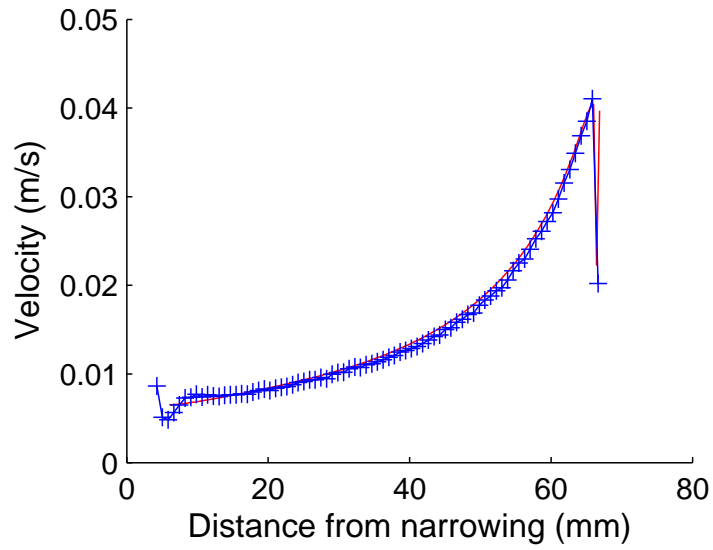
(a)
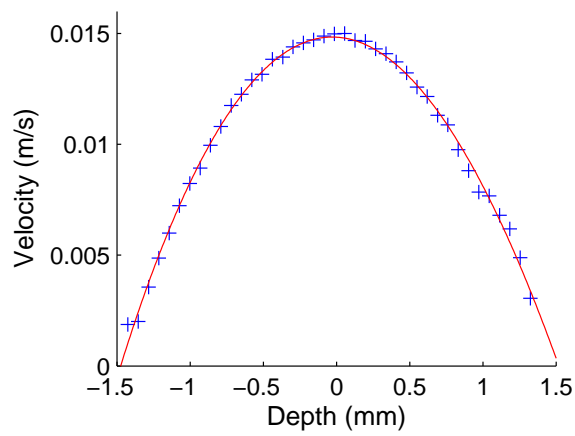
(b)

Figure IV.4: A comparison between theoretical centreline (a) or depth (b) profile and measured profiles (blue markers). The flow rate was controlled at 15 mL/min^{-1}.
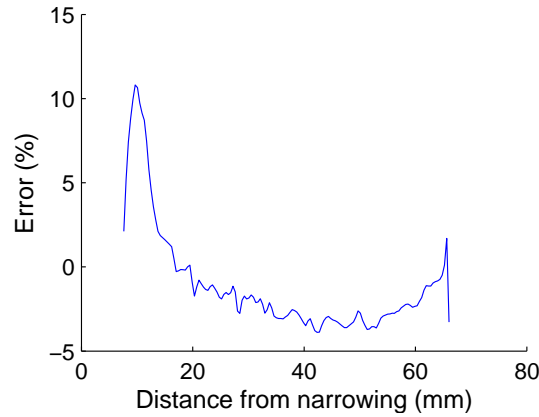
Figure IV.5: The mean measurement error to the theoretical profile as a function of the distance from narrowing

simulated flow profile, and are plotted in Fig. IV.2.3.a.

To determine the sensor's accuracy, the measured velocity was compared to the actual velocity for each measurement point, and the error is plotted in Fig. IV.5. As expected, the error increases near the entrance and the exit. This can be explained by two effects. First, these areas are situated near the tubing connectors, and at these locations, the flow can show a turbulent behaviour. The flow profile is no longer laminar, and the measured velocity changes with time. This is corroborated by the fact that the sensor shows poor repeatability at theses points (Fig. IV.3). Moreover, the measured velocity is either very low (entrance), and therefore the Doppler peak coincides with noise, or very high (exit), and the flattening of the Doppler peak affects the fit algorithm.

IV.2.3.b   Depth profile

To measure the flow velocity profile in depth, Doppler spectra were measured over a grid of values from $-nD/2$ to $nD/2$ where $D = 3$ mm corresponds to the channel depth and $n = 1.33$ to the refractive index of the liquid. For parallax approximation ($\theta < 10°$), the mechanical distance travelled by the mechanical stage in the air corresponds to $1/n$ time the distance travelled by the beam in water. The results are plotted in Fig. IV.2.3.a and show very good agreement all over the displacement range.

IV.2.4 Conclusion

We have demonstrated that OFI can be used to accurately measure flow profile, when the spot size is less than 10 times smaller than the flowchannel size. We have observed that experimental conditions can lead to strong inaccuracies. In order to counter uncertainties due to monitorable parameters for microfluidics applications, we decided to use:

- A syringe pump (PHD 22/2000 Harvard apparatus) instead of a peristaltic pump coupled with a tubing and reservoir system, to accurately control the flow rate. Previously, we were using a peristaltic pump and a system of valve control to set the flow rate, and we were measuring the amount of liquid flowing in a becher during a known amount of time. Using a dedicated pump will increase the precision on flow rate.

- A calibration process to measure to the actual value of λ, n and θ

Once freed from experimental parameters fluctuations, the impact of the sensing volume shape and size can be investigated by measuring flow profile in sub-millimeter channels.

IV.3 Flow profile measurement in microchannels

The sensor as well as the experimental protocol have been successfully validated in a macrochannel. Consequently, the aim of this section is to demonstrate the performance of OFI to measure local velocities in fluids with spatial resolution in the micrometer range and enables reconstruction of a velocity profile inside a microchannel.

IV.3.1 Laminar flow with Newtonian fluids

IV.3.1.a Experimental set-up

Flow profiles in microchannels have been measured under the experimental conditions described in Table IV.2, using the setup in Fig. III.13.

The flowchannel used had a circular cross-section of inner diameter 320 μm. The liquid under test was composed of 98 % water and 2 % milk by mass, in order to guarantee the single scattering regime. By assuming that the particle concentration in our solution is low enough that the parameters of the fluid can be approximated to those for water (μ=0.001 Pa.s, ρ=997 kg/m^3 at 20 °C) and with respect to the flow rates imposed (from 5 to 50 μL/min), the Reynolds number varies from 0.33 to 33 (laminar regime). For a laminar flow, the velocity profile in a circular channel is parabolic, with the velocity increasing from zero at the wall (no slip boundary condition) to a maximum value at the centre equal twice the average velocity Q/S (Poiseuille's law).

Parameter	Numerical values
Flowchannel	circular cross-section (diameter $2R = 320$ μm)
Liquid	Milk (2 %)- Water (98 %)
Refractive index	1.34
Lens 1	C260 (f=15.26 mm)
Lens 2	C240 (f = 8 mm)
θ	80°
LD driving current	1.8 mA
LD wavelength	667 nm

Table IV.2: Parameters used for flow profile measurement in single scattering regime: Newtonian liquid

The assembled optical head (see Chapter III) was characterized with a beam profiler, and the spot diameter in focus was measured to be 32.26 μm. The magnification of the dual-lens optical system was 0.72, leading to a theoretical output beam diameter of 23.22 μm. This results in a sensing volume of 7.16×10^5 μm^3, providing for a sufficient spatial resolution to scan the channel, which has a 320 μm internal diameter. Both lenses are mounted on XY translator for cage system, in order to control precisely the position of the lenses. The entire optical head was mounted on a goniometer, mounted itself on the computer controlled 3-axis motorized translation stage. The focus point was stepped through the channel by the translation stage to obtain the measurement points needed to reconstruct the flow profile.

All the reported Doppler spectra have been obtained as the mean of 64 successively acquired spectra. The acquisition time was lower than 10 ms. Therefore, the sensor response time can be considered as being close to real-time.

IV.3.1.b Calibration process

To minimize uncertainties while calculating the flow profile in microchannels, the value of θ has to be measured precisely. The optical head is mounted on a precise goniometer, and angled manually at 80 ° with respect to the flow direction. However, a small misalignment in the optical system can lead to an effective angle θ different from the one read on the goniometer as observed in section IV.2.3. As the relationship between the measured Doppler frequency and the actual velocity in the sensing volume is a function of $\cos(\theta)$, it affects greatly the OFI flowmeter precision. The calibration protocol was set to minimize the error due to experimental inaccuracies, in such way that all experimental parameters are known and kept constant during the experiment. First, the laser beam focus was moved to the middle of the channel

(a)   (b)
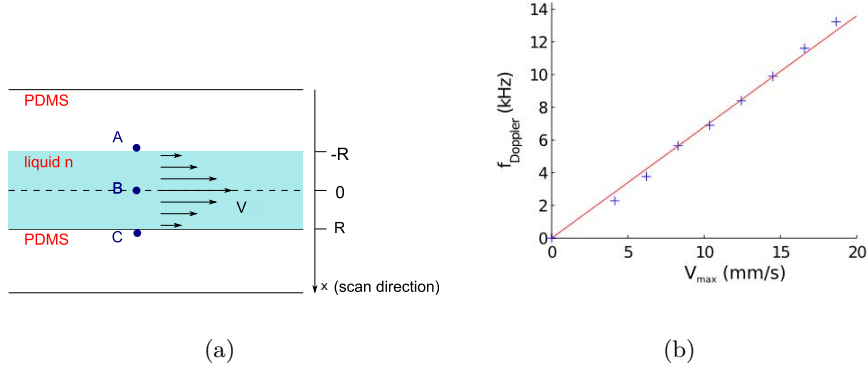
Figure IV.6: (a) Diagram showing the scan configuration with respect to the z-axis of the flow-channel. The angle calibration is calculated at position B, and the velocity profile is measured from A to C. (b) Plot of the Doppler frequency as a function of velocity in the center of the tube $V_{\max} = 2Q/S$. The angle between the flow direction and the optical beam can be estimated from the slope of this relationship, and is 80.25 °

(position B in Fig. IV.3.1.b) and the position was then further adjusted to where the OFI signal exhibited the highest frequency. Then, the average Doppler frequency within the sensing volume was extracted from the OFI signal spectrum using the fitting function (III.22).

Doppler spectra were recorded at different fluid flow rates Q from 0 to 50 µL.min^{-1}. The frequency of the Doppler peak as a function of the maximum velocity $V_{\max} = \frac{2Q}{S}$ measured at the center of the channel is shown in Fig. IV.3.1.b.

The final step of the calibration procedure consists in calculating the incident angle θ from the slope of the fitting in Fig. IV.3.1.b. It was calculated to be 80.25 °, close to the value given by the goniometer stage.

IV.3.1.c   Experimental results

To measure the velocity profile, the laser focus was first moved back to position A in Fig. IV.3.1.b, and the laser scanned across the flow-channel (x direction in Fig. IV.3.1.b) in 10 µm steps toward position C.

The liquid under test was milk diluted in distilled water (1:50), pumped at different flow rates (20, 40 and 60 µL.min^{-1}), which corresponds to a maximum velocity of 8.28, 16.56 and 24.84 mm.s^{-1} respectively. The exper-
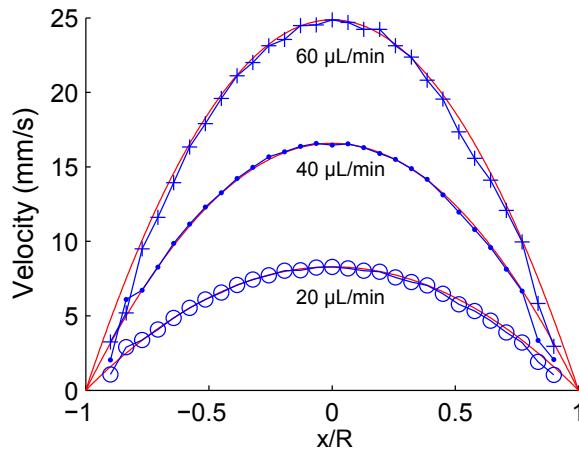
Figure IV.7: A comparison between theoretical profile (solid red curve) and 8 consecutive measured profiles (blue markers) along the centre-line of the flow-channel with a flow rate of 20, 40 and 60 μL/min^{-1}.

imentally reconstructed flow profiles are plotted in Fig. IV.7. The solid curve represents the theoretical parabolic velocity profile described by Poiseuille's law, whereas the blue markers represent the measured velocity at each radial location.

IV.3.1.d   Error measurement and repeatability

To investigate the performance of OFI flowmeter, the milk/water mixture was pumped at 20 μL.min^{-1}, and 8 consecutive spectra were acquired (Fig. IV.9).

The difference between the experimental and the theoretical velocities is plotted in Fig. IV.8. Notwithstanding the first point (with a discrepancy of 3 %), this measurement indicates good agreement with theory. Over the usable range, the relative error for each measurement point was less than 1.8 %. The error near the channel's walls can be attributed to the difficulty in fitting the Gaussian peak close to the low frequency noise induced by the system.

To estimate the repeatability of the measurement, the standard deviation over 8 consecutive scans was calculated for each measurement point (Fig. IV.9). In addition to the higher relative error observed in the previous paragraph, and due to the same causes, the sensor also shows a lower repeatability near the channel's wall.
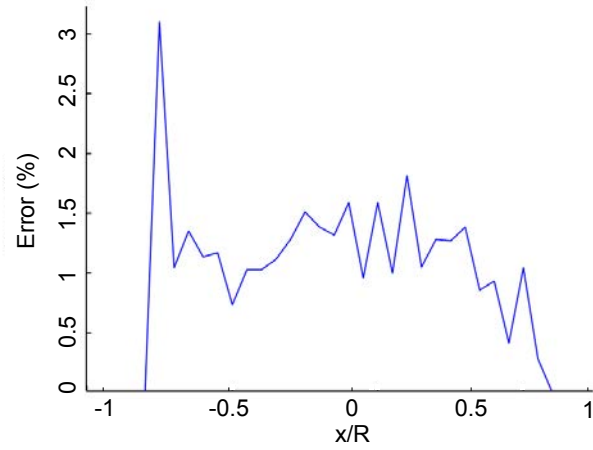
Figure IV.8: The mean measurement error to the theoretical profile in relation to the scanned position within the tube
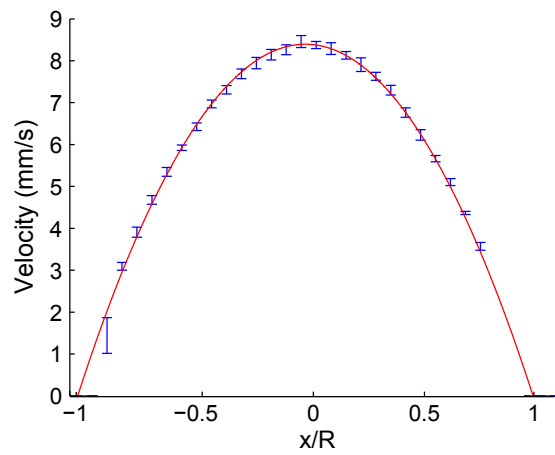
Figure IV.9: A comparison between theoretical profile (solid red curve) and 8 consecutive measured profiles (blue markers) along the centre-line of the flow-channel with a flow rate of 20 $\mu L/min^{-1}$. The liquid is milk (2 %) diluted in water

Glycerol (%weight)	μ @20 °C (mPa/s)	n	R_e @$Q = 50$ μL/min
0	1.005	1.333	3.33
10	1.31	1.344	2.54
20	1.76	1.357	1.9
30	2.50	1.37	1.33
40	3.72	1.384	0.89
50	6	1.398	0.55
60	10.8	1.412	0.3

Table IV.3: Viscosity μ, refractive index n and Reynolds number R_e for various aqueous Glycerol solutions [15]

The minimum spatial resolution of the system depends on the fluid composition and velocity, and could not be accurately measured. The laser spot size has been estimated at 32 μm, but Fig. IV.9 shows that the effective spatial resolution of the sensor is better than 10 μm. These preliminary results demonstrate the feasibility of OFI measurement in microchannels of size well below 320 μm.

IV.3.2 Glycerol liquid phase: effect of the viscosity
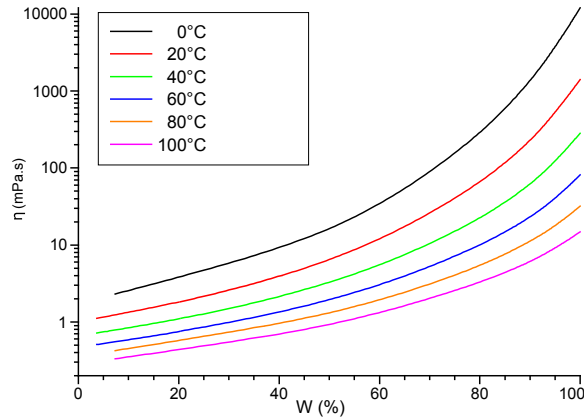
Figure IV.10: Viscosity of Glycerol depending on mass fraction for different temperatures.

To validate the sensor versatility, we investigate its performance while measuring the flow profile of various liquids in the circular flowchannel. The liquids pumped through the flowchannel consisted of various percentages of Glycerol and water. Table IV.3 details for each aqueaous Glycerol solution, its viscosity, refractive index and Reynolds number [15]. These solutions have been chosen because their refractive index can be easily adjusted by changing the Glycerol proportion. Indeed, Glycerol is a Newtonian liquid

Parameter	Numerical values
Flowchannel	circular cross-section (diameter $2R = 320$ μm)
Lens 1	C220 (f=11 mm)
Lens 2	C240 (f=8 mm)
θ	75°
Q	50 μL/min
LD driving current	1.8 mA
LD wavelength	667 nm

Table IV.4: Parameters used for flow profile measurement in single scattering regime: Glycerol liquid phase

whose viscosity varies sharply with concentration and temperature as depicted in Fig. IV.10. The theoretical velocity profile in a circular duct should follow Poiseuille's law. The aim of this study is (i) to prove that changes in viscosity has no impact on flow profile measurement using OFI flowmetry, and (ii) to investigate the sensor performances for various refractive indices.

The experimental parameters are described in Table IV.4. Since Glycerol solutions did not backscatter enough light to provide a measurable OFI signal, artificial seeding were added to the solutions (2 % milk). The mix water/glycerol/milk was pumped at 50 μL/min, and the sensor was calibrated using the protocol described in Section IV.3.1.b. The angle θ was measured to be 75.8 °, and the refractive index n was extracted from theoretical tables [15].

Finally, the laser scanned across the flow-channel (x direction in Fig. IV.3.1.b) with 10 μm steps. The flow profiles for each solution are presented in Fig. IV.11. It can be observed that the change in refractive index and viscosity do not affect the flow profile, which follow Poiseuille's law, as expected. The points situated near the channel's walls show little fluctuation, but it is mostly due to the difficulties in fitting the Gaussian peak located near the low-frequency noise rather than uncertainty due to viscosity changes.

IV.3.3   Laminar flow with non-Newtonian fluids

IV.3.3.a   Experimental conditions

Adding a shear-thinning fluid to the initial milk-water mix leads to a different velocity distribution in microchannels. The aim of this experiment is to prove that different flow profiles can be measured and distinguished from each other using OFI flowmetry.

129
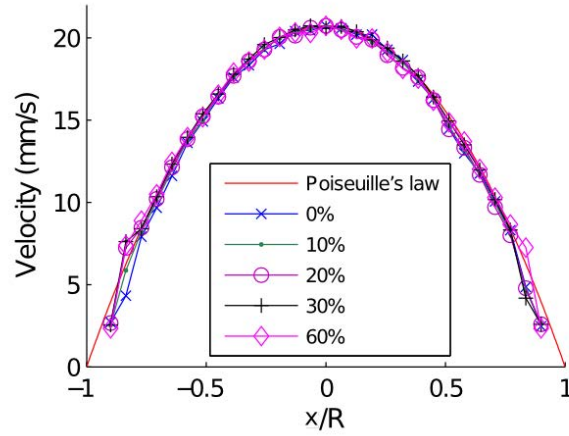
Figure IV.11: A comparison between theoretical profile and measured profiles (markers) for various concentration of Glycerol along the centre-line of the flowchannel with a flow rate of 50 μL/min^{-1}. Percentage of Glycerol (weight): [0, 10, 20, 30, 60]

Flow profile for non-Newtonian liquids have been obtained using the parameters described in Table IV.2, with the exception of the liquid pumped through the flowchannel. Indeed, xanthan gum powder was added in various concentrations to the 2 % milk solution used previously. Xanthan gum, whose viscosity decreases with shear rate, shows a shear-thinning behaviour. The Ostwald-de-Waele law is chosen to model the variation of viscosity μ with shear rate $\dot{\gamma}$ for the xanthan gum based liquid phase:

$$\mu = K \cdot \dot{\gamma}^{m-1} \tag{IV.1}$$

where K is the consistency index and m the flow index. They are determined from experimental rheograms. The analytical solutions for the velocity profile when a purely shear-thinning fluid flows inside a circular channel is given by:

$$V(z) = \frac{Q}{S} \frac{3m+1}{m+1} \left(1 + \left(\frac{z}{R} \right)^{\frac{m+1}{m}} \right) \tag{IV.2}$$

where Q is the pumping flow rate, S the area of the cross-section of the channel, z the distance from the center, and R the radius of the channel. Note that if $m = 1$, the Poiseuille's law is found again.

Within the laminar range, the velocity profile is expected to become flatter in the center as the solution becomes shear-thinning as described by Eq. IV.2.

130

IV.3.3.b Experimental results
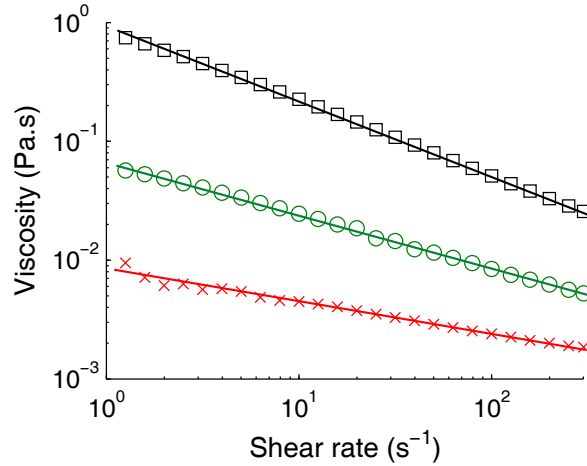
Figure IV.12: Experimental rheograms for various concentrations of xanthan gum (0.25 (cross) 1 (circle) and 3 g/L (square)). The viscosity of each solution as a function of the shear rate applied are plotted in logarithm scale.

Four solutions with different xanthan gum concentrations (0, 0.25, 1, and 3 g/L) were pushed through the flow-channel at a pumping rate of 30 µL.min^{-1}. We measured the relationship between the shear rate and the viscosity for each solution, using a rheometer (TA instruments AR 2000) with a small-angle cone and plate device (Fig.IV.12). The temperature was controlled at 25 °C. The power law exponent m was then extracted from these experimental rheograms using Eq. (IV.1), and found to be 1, 0.73, 0.56, and 0.37 respectively. The theoretical velocity profiles obtained using Eq. (IV.2) with the calculated values of m are compared to the measurement results in Fig. IV.13. The results are comparable to the one obtained for Newtonian liquids. The same order of error is retrieved, such as the increase of error and decrease of repeatability near the channel's walls. It can also be observed that the velocity profile differ from each other when the amount of xanthan gum changes. Thus, the discrimination of different velocity profiles by OFI is demonstrated, and the technology's application to the measurement of some complex flow behaviour is verified.

IV.3.4 Conclusion

An OFI microfluidic flow sensor capable of accurately measuring flow rates and profiles in micrometer-scale channels has been presented. Flow profile reconstruction of a laminar flow in a channel with an internal diameter of 320 µm has been demonstrated. At its current stage, OFI could mea-
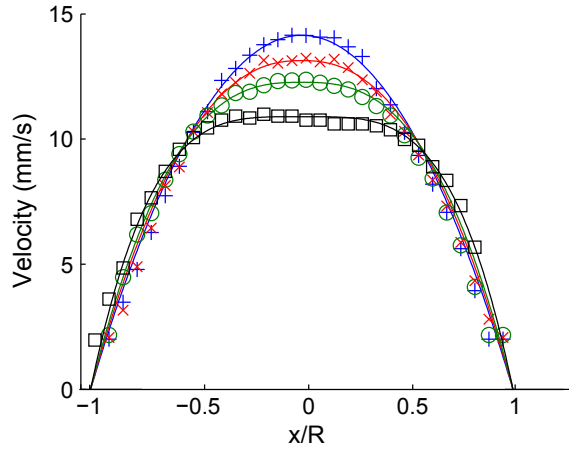
Figure IV.13: Measured (markers) and theoretical (solid line) velocity profile in a 320 μm channel for various solutions of xanthan gum (0 (plus), 0.25 (cross), 1 (circle), and 3 g/L (square)).

sure centerline (y direction in Fig. III.14) and cross-section (x direction in Fig. III.14) flow profiles. The depth measurement (z direction in Fig. III.14) has been investigated in the next section.

Parameter	Numerical values
Flowchannel	circular cross-section (diameter $2R = 320$ μm)
Liquid	Milk (0.5 %)- Water (99.5 %)
Refractive index	1.33
Lens 1	C260 (f=15.26 mm)
Lens 2	C240 (f=8 mm)
θ	80°
Q	20 μL/min
LD driving current	1.8 mA
LD wavelength	667 nm

Table IV.5: Parameters used for flow profile measurement in depth (x direction)
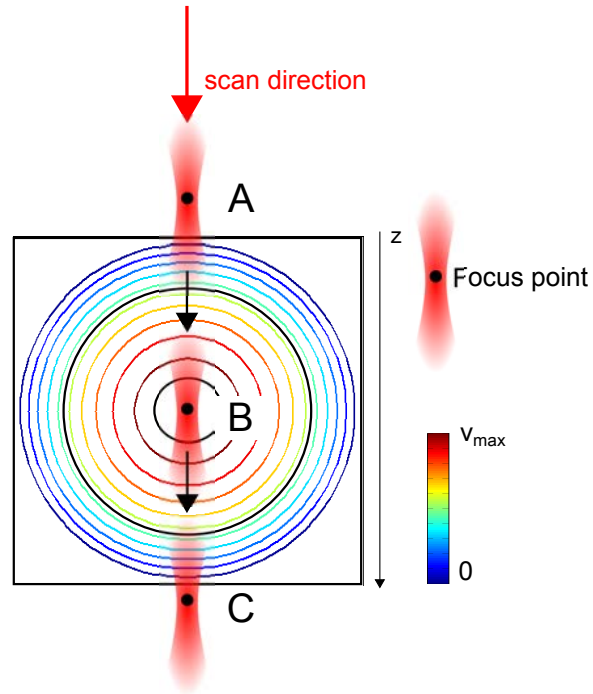
(a)
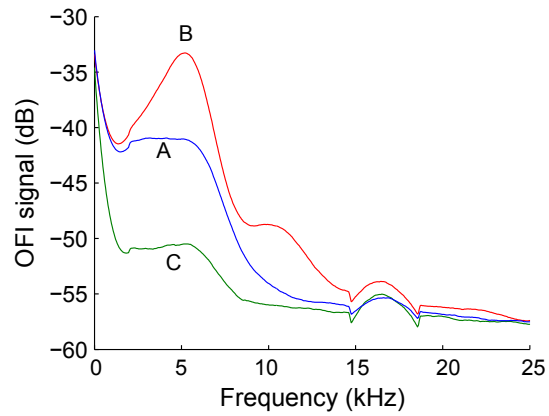
(b)

Figure IV.14: (a) Scheme of a scanning process for depth flow profile measurement (b) OFI spectra acquired at position A, B and C

IV.4   Three-dimensional flow profile in microchannels

IV.4.1   General considerations

Three-dimensional velocity distributions are of great interest for many Lab-on-a-chip applications, where mixing and flow transportation can be realized on multiple layers. To measure the velocity profile in depth, the laser focus was first set at position A in Fig. IV.4.1, and then moved across the flowchannel in 20 µm steps toward position C. In OFI flowmetry, the theoretical sensing volume is asymmetric and shows a larger dimension in the direction of the laser. The depth of focus $2Z_R$ is commonly used to estimate the sensing volume size in depth direction:

$$2Z_R = \frac{2\pi W_0^2}{\lambda} \tag{IV.3}$$

Where W_0 is the theoretical beam waist and λ the laser wavelength.

Under the experimental conditions described in Table IV.5, the depth of focus is calculated to be 2.7 mm. This value is much larger than the flowchannel diameter. The OFI spectrum should always exhibits a flat profile, as all velocities from 0 to V_{max} should be represented in the frequency domain. However, the signal acquired in the middle of the channel (Position B in Fig. IV.4.1 exhibited a Gaussian peak, i.e. no zero velocity is sampled. In Position A and C, the spectrum is flat, indicating that the particles close to the channel's walls are in the actual sensing volume, contributing to OFI signal.

Nevertheless, measuring flow profile in the laser direction led to the following complications:

- The spatial resolution is lower.

- The OFI spectrum does not have the same shape as it is sampled near the channel's walls (flat profile) or in the middle of the channel (Gaussian peak). The signal processing method has to be adapted for each measurement points (see Fig. IV.4.1).

- For high particle density, the measurement points located near position C suffer more from absorption than points located near position A, affecting the SNR.

- When focused in position C, particles situated higher in the optical path can also backscatter light whereas when the laser is focused in position A, only the contributions from the sensing area are observed.

- In turbid liquids, OFI signal can be measured when the laser beam is focused outside the flowchannel, because some particles located at the edge of the sensing volume backscatter enough light to be detected. While measuring flow profiles, on can think that the flowchannel is larger than it is in reality.

To measure the flow profile in depth, we choose a to use a solution with a very low particle concentration (0.5 % milk), so that the parasitic effects listed below were minimized.

IV.4.2   Mechanical distance versus actual distance

While measuring a flow profile at a constant depth, one can assume that the mechanical distance travelled by the laser head, controlled by computer, corresponds to the actual distance travelled in the flowchannel, neglecting the effect of the channel's curvature radius. However, this approximation is not valid for flow profile measurement when the depth is changing, on account of the channel's geometry and the refractive index of PDMS (1.47) and water (1.33). The beam is refracted at the two interfaces, and it is obvious that the actual distance (z_{liquid}) in the liquid differs from the mechanical distance read on the linear stage (z_{air}). To counter this problem, we simulated the optical path of the laser beam using the ray matrix approximation, as described in Appendix C. For an angle between the optical head and the flowchannel $\theta = 80°$, the relationship between z_{air} and z_{liquid} was found equal to:

$$z_{\text{liquid}} \sim \frac{n_{\text{liquid}}}{2 \cos(n_{\text{liquid}}\theta)} z_{\text{air}} \sim 0.67 z_{\text{air}} \tag{IV.4}$$

Where n_{liquid} is the liquid refractive index. In this configuration, moving from 20 μm in the air corresponds to a distance travelled of 13.4 μm in the flowchannel.

IV.4.3   Experimental Results

The experimental set-up described in Chapter III was used to measure the flow profile in the circular microchannel, and the experimental conditions are listed in Table IV.5. The laser was first focused near the channel's top wall (Position A in Fig. IV.4.1), and moved towards the bottom wall by 29.85 μm steps (corresponding to 20 μm in the channel). For each depth, 64 spectra were acquired and averaged. The 3 dB cut-off frequency was then calculated. This scan process has been repeated 5 successive times, and the results are plotted in Fig. IV.15.

Actual and measured velocities show strong congruency during the first half of the tube (A→B), but diverge during the second half of the scan
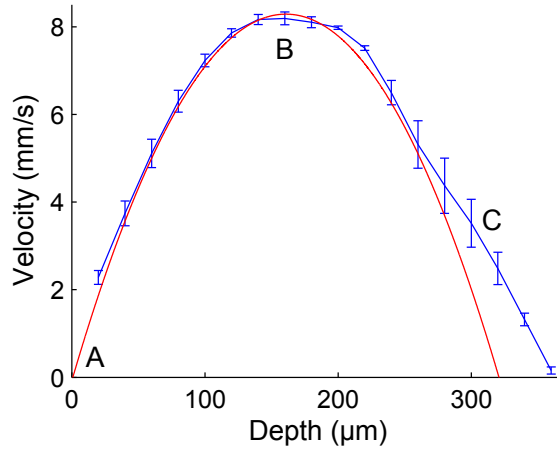
Figure IV.15: Comparison of theoretical (red curve) and measured velocity (blue curve and errorbars) flow profile in depth at a flow rate of Q=20 µL/min

(B→C). Furthermore, the difference between actual and measured velocity increases with depth. Finally, the sensor shows lower repeatability than for flow profile measurement across the channel's section, and repeatability strongly decreases with depth. These results are not surprising, considering the complications induced by a large sensing volume in microfluidics applications. We also believe that the error to the theoretical profile increases also with particle concentration, as more particles can be be found in the upper part of the beam, leading to an increase of OFI contributions coming from outside of the region of interest.

Finaly, the entire channel was scanned by performing 17 horizontal scans starting from the top of the channel, resulting in a total of 17x17 points. The measured data were then combined to form a two-dimensional map of the fluid flow distribution as depicted in Fig. IV.4.3 and Fig. IV.4.3. A good agreement can be seen between the simulated and measured results in the top half of the channel, but large errors and fluctuations can be observed in deeper locations. The rate of error is very high near the bottom wall, as predicted by the depth flow profile measurement.

IV.4.4 Conclusion

The system's ability to accurately measure a 3-D flow profile has not been demonstrated for microfluidics applications. An idea to counter this problem may consist in adding a spatial pinhole to eliminate out-of-focus light,
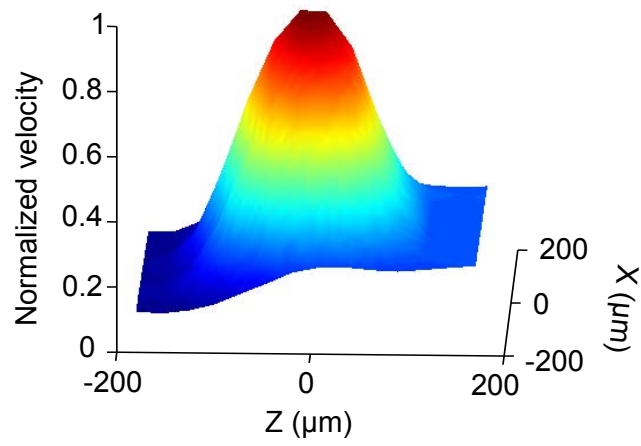
(a)
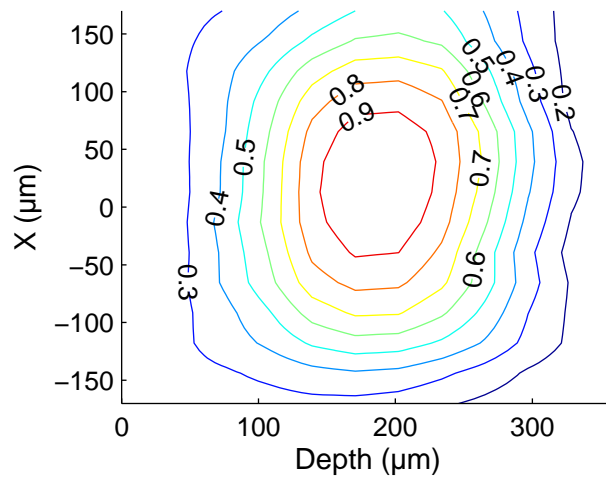
(b)

Figure IV.16: 2D flow profile in a circular flow channel (a) 3D view and (b) equivelocity area.

137

drawing from confocal microscopy principle. In any cases, further studies need to be performed to fully understand the mechanism behind OFI for fluidic applications.

IV.5 Comparison with a well-established technique of flow measurement in microchannels: the dual slit technique (DS)

IV.5.1 Context

The dynamics of blood flow in microvascular networks is of great importance in the exchange of nutrient and waste substances between blood and living tissues. In these vessels of diameter less than 100 µm, the development of quantitative methods for measuring the velocity of red blood cells (RBCs) is still challenging. In this context, the Dual-Slit (DS) technique, a temporal correlation technique first introduced by Wayland and Johnson [125] (See Chapter I), is commonly used. It has recently shown that, as long as several operational conditions are fulfilled, this technique can offer a precise measurement of the transverse velocity profile of RBCs, i.e along the x axis in Fig. IV.17. The measured velocities are maximal velocities in the depth of the channel, i.e. y direction [130]. However, this technique requires expensive equipment (high speed camera) and the related data-treatment is time consuming. Moreover, the duration of the acquisition is long (typically 20 to 40 s). For these reasons, on line measurements, especially in cases of transient regimes, are not possible. The aim of the present work is to determine whether OFI can be used to perform quantitative measurements of RBCs velocity in channels of size less than 100 µm, and it also enable a comparison of performance with an actual sensor dedicated to flow profile measurement in microchannel. For that purpose, the velocity profiles obtained by OFI and DS are compared, using PDMS microchannels and spherical monodisperse particle suspensions in set-up configurations where the DS has been previously validated.

IV.5.2 Experimental conditions

Particle suspensions $(0.1\%(v/v))$ are prepared from a concentrated stock solution of 4 µm diameter latex microspheres (In Vitrogen). The index of refraction of these particles is given by the manufacturer ($n = 1.6$). The flow is controlled in rectangular PDMS micro-channels of size 20 µmx100 µm using a syringe pump (PHD 22/2000 Harvard Apparatus) and Hamilton Gastight glass syringes. First, the DS technique is applied. In this technique, the channel under study is transilluminated and two photo-sensors (slits) are positioned, separated by a known distance, L_s, along the vessel
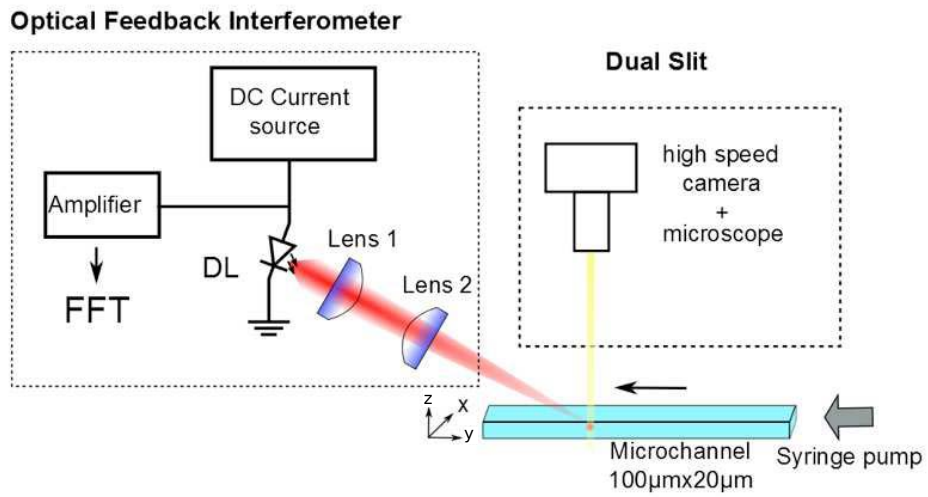
(a)
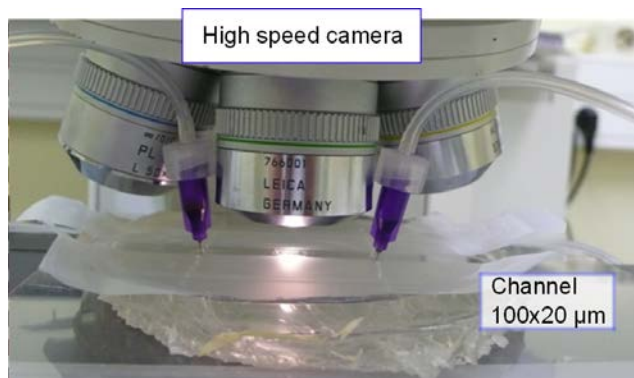
(b)

Figure IV.17: (a) OFI (left) and DS (right) experimental configurations (b) Picture of the DS experimental set-up

Parameter	Numerical values
Flowchannel	rectangular cross-section 100x20 µm
Liquid	Latex sphere (In Vitrogen, 4 µm diameter)
Refractive index	1.33
Lens 1	C260 (f=15.26 mm)
Lens 2	C240 (f = 8 mm)
θ	80°
Q	1 µL/min
LD driving current	1.8 mA
LD wavelength	667 nm

Table IV.6: Parameters used for flow profile measurement in rectangular flowchannel 100x20 µm
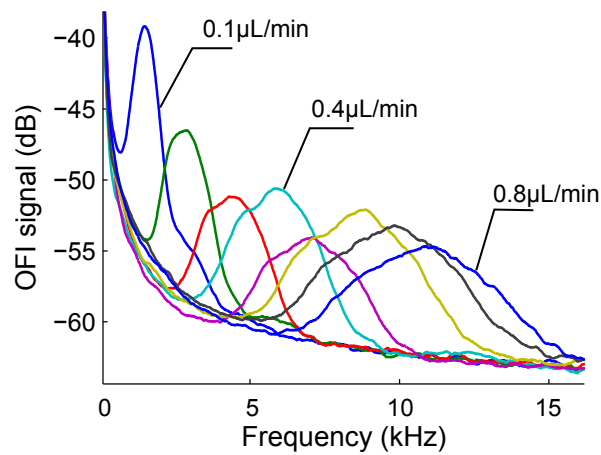
Figure IV.18: OFI spectra for flow rates varying from 0.1 to 0.8 µL/min
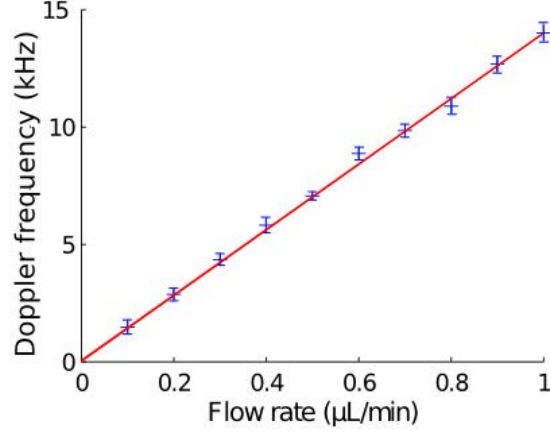
Figure IV.19: Doppler cut-off frequencies (-3 dB) measured in a 100x20 μm rectangular channel for various flow rates Q=[0.1:0.1:1] μL/min

axis (z direction in Fig. IV.17). In our case, the slits are regions of interest (1x3pixels) on images of particle flows recorded using a high speed video camera (PCO Dimax). The time modulation of light, produced by the passage of the particles flowing through the channel, is deduced by performing the sum of grey levels in both slits at each time step. For various distances L_s between the two slits, a cross-correlation velocity, $V_{ds} = L_s/T_d$, is obtained, where T_d is the time delay for which the cross-correlation between the two signals is maximum. For an optimal L_s [130], the final velocity at a given point on the x axis represents the maximal velocity in the y direction. Finally, the slits are successively positioned in the x direction to obtain a profile of RBCs maximal velocities.

The OFI technique is then applied to the same microfluidic set-up. A special attention was paid to the choice of lenses. The optical head components, described in Table IV.6, provide an estimated sensing volume $1.5 \cdot 10^5$ μm³. It is indeed 7 times smaller than the one employed for measuring the flow profile in the 320 μm flowchannel.

Both experimental set-ups are represented on Fig. IV.17. As shown by Roman et al. [131], in the conditions of this experiment for the DS technique, the measured velocity at each point in the x direction corresponds to the maximal velocity in the depth of the channel (z direction).

141
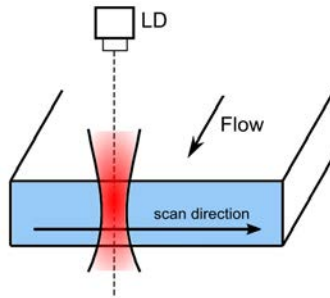
Figure IV.20: OFI sensing scheme in the 20 μmx100 μm flowchannel
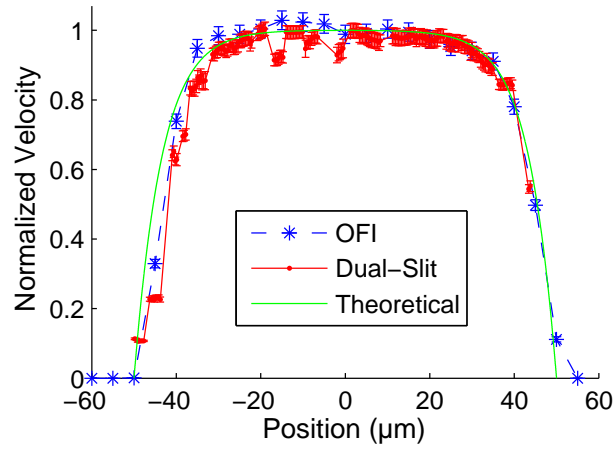
Figure IV.21: Comparison of flow profile in a rectangular flowchannel measured with OFI flowmetry (blue curve) and dual-slit technique (red curve)

IV.5.3 Results

In order to validate the OFI technique, the laser spot was first focused in the middle of the channel, and the pumping rate was set from 0.1 to 1 μL/min. 64 successive spectra were acquired and averaged at each pumping rate, and the corresponding Doppler frequency was calculated. The OFI spectra are depicted in Fig. IV.18. It can be observed that the OFI signal exhibits a Gaussian peak, although the estimated sensing volume is much larger than the flow channel smallest size (see Fig. IV.20). According to the experimental configuration, some frequency contributions should be found for low frequency, as the sensing volume is sampling the channel's walls. A crenel-like shape should be observed. However, we used latex microspheres soaked with surfactant, so that the particles near the surface may bounce along the channel's walls, and do not meet the no-slip boundary conditions.

Furthermore, the Doppler frequency position varies linearly with the flow rate, in accordance with theory as depicted in Fig. IV.19.

Both reconstructed profiles, as well as the Newtonian theoretical profile [250], normalized by the maximal measured velocity, are plotted on Fig. IV.21. The profile shapes are similar for the two techniques showing that OFI is suitable for measuring velocity distributions in such channels. The average error along the profile is lower than 5.2 %, which is the same order of magnitude as the error measured in the 320 μ channel, which is 40 times bigger in volume. These preliminary results demonstrate the feasibility of OFI measurement in microchannels of size below 100 μm.

IV.6   Conclusion

In this chapter, we demonstrated how OFI could be employed to measure velocity distributions in macro and micro channels.

Nevertheless, we identified three necessary conditions so that OFI can provide accurate measurement of flow profile. First, the theoretical sensing volume should be at least 10 times smaller than the scanned dimension of the channel, so that the changes in velocity between two consecutives point can be detected. Then, the density of particles in the liquid should exhibit a single scattering behaviour, so that the Doppler peak can be recognized and linked analytically to the liquid's velocity. Finally, a preliminary calibration should be performed, in order to determine experimental parameters such as the angle between the laser and the flow, and the refractive index of the liquid phase. Under these conditions, the absolute value of the local velocity in a flow distribution can be calculated, and by scanning the area of interest, the entire velocity distribution can be reconstructed.

To confirm the suitability of OFI sensor, we measured the velocity distribution in a channel which dimensions are at the limit of OFI range, and compared the flow profile obtained with the one measured using a standard technique: Dual-Slit. OFI could measure the entire velocity profile within 2 minutes using approximately 20 Mo of data, whereas Dual-slit requires an acquisition time of 5 s but over 10 Gigas of data. As the temporal resolution of OFI is mainly limited by the mechanical scan, we believe that a flow profile acquisition time of approximately 10 ms can be reached by arranging the sensor into a matrix that map the whole channel.

This chapter confirms that OFI can be used to measure and monitor flow distribution in microchannel, and that it can be an alternative to traditional technique for a low cost, portable sensor for industrial and biomedical applications.

Conclusion

The purpose of this thesis is to determine whether there is an interest in a new non-invasive sensor based on Optical Feedback Interferometry to measure accurately flow rate and velocity distribution in microchannels.

In chapter I, we studied the existing optical sensors that measure flow rates and velocity distribution in sub-millimeter flowchannels. We noticed that the new developments of mature technologies (LDV, μ-PIV) are mostly focused on increasing their spatial resolution, as well as their temporal resolution. This results in the preponderance of complex, expensive and bulky systems. OFI appeared as an emerging technology appropriate to measure precise velocity of flowing liquids. Some experimental studies have been randomly conducted in the 90's to measure changes in blood flow rate in-vivo, and showed promising results. The applications to microfluidics had to wait 2005, but are increasing since 2010. This demonstrate a renewed interest in the low cost, compact technique of OFI flowmetry. Consequently, the aim of the OFI flowmeter developed in this thesis is to measure flow velocity with a precision and resolution comparable to the one obtained with LDV, μ-PIV and Dual-Slit. Its other features would be to be versatile (i.e. with the same hardware, velocity, particles concentration and size can be measured), disposable for in-situ measurement, easy to align, low-cost and robust.

We first studied the behaviour of an OFI sensor applied to velocity measurement. Although a large amount of models have already been developed to describe how the coupling of backscattered wave in the active cavity can disturbed the LD and can allow the measurement of the velocity of a moving solid state target, we needed an appropriated model to introduce a target made of several particles. Therefore, we started from the well-known quasi-static compound cavity model, and we modified it by introducing in the equations the frequency shift induced by the Doppler effect on the target's interface. We first validated our model on a rough target in translation in front of the laser, which absolute velocity has been retrieved. In addition, we demonstrated that modulating the LD frequency increases the dynamic range of this sensor, as the Doppler peak is shifted towards higher or lower frequency depending on the modulation type, allowing the measurement of very rapid or slow objects.

This modified model has been applied to a single particle, before being extended to a group of particles. We restricted our study to single scattering behaviour (i.e. each particles can be considered as independent scattering centres). This model provided a good estimation of the shape and position of the signal in frequency domain while measuring the velocity of seeds in aqueous phase. Furthermore, the impact of the flow rate, concentration, particles diameters and refractive index on the OFI signal have been investigated, in order to understand how the signal in OFI flowmetry varies.

146

Based on these theoretical statements, an OFI sensor dedicated to microflow measurement has been designed. It is based on a low-cost commercial VCSEL, chosen for it small beam divergence and beam shape. The VCSEL as well as the optical set-up have been mounted on a precise 3D translation stage. The sensing volume size has been adjusted using two lenses chosen in function of the flowchannel, and the purpose of the experiment. The signal has been measured on the VCSEL's junction voltage, in order to avoid the need of any external photodetector. This configuration reduces the cost and complexity of the sensor. In addition, single VCSELs can be arranged into an array to acquire in one shot an entire map of flow rates.

The measurement of flow rates in microchannels was first performed to validate the sensor. In the first experimental setup, the sensing volume was 10 times smaller than the flowchannel diameter. The OFI signal exhibited a Gaussian shape, and the flow rate varying from 10 to 90 µL/min has been retrieved with less than 2% error. However, we observed that when the sensing volume is on the same order of magnitude than the channel's typical size, the signal becomes crenel-like. Consequently, another signal processing method has been developed, that consists in measuring the 3 dB cut-off frequency of the OFI signal in frequency domain. In such conditions, flow rates between 10 and 90 µL/min have been retrieved with an error less than 8%.

In turbid liquids, the scattering regime becomes multiple scattering, and the OFI spectrum exhibits an exponential decreasing behaviour. Nevertheless, it is possible to recover the flow rate between 10 and 90 µL/min with an average error of 10% using calibration methods. Three signal processing methods have been studied and compared, and it seems that the method specifically devellped for this thesis and that uses the noise power spectrum subtracted to the OFI signal (Method 3) showed the best compromise between accuracy, memory and time consumption.

Beside the flow rate, we demonstrated the measurement of the velocity distribution in microchannels, as it is of great interest to understand fluid transport and mixing, rheology and chemical reactions. Velocity distributions in flowchannels were first measured under low particles concentration, as in such configuration, flow rate measurement showed the best performance. In a 21x3mm flowchannel, the cross-section as well as the depth profile was reconstructed with a precision of 2 %, for velocities varying from 0.01mm/s to 1mm/s. In microchannels, the flow profile (cross section) was successfully reconstructed for various liquids (non Newtonian, various refractive index) at several flow rates (from 10 to 60 µL/min), with an average error lower than 3%. However, in depth, the sensing volume was not small

147

enough because of its asymmetric shape, and leaded to large measurement errors.

Finally, a flow profile has been measured in a 100x20 μm microchannel, and the results obtained were compared with those obtained under the same conditions with the Dual-Slit technique, which has been already validated in this channel. The results concurred to the theoretical profile, with an average precision of 4.6 %. The OFI sensor reconstructed the entire profile within 2 min (40 s for DS). With the future removal of scanning, the time acquisition could easily drop down to 10 ms.

In conclusion, the OFI sensor dedicated to flow measurement in submillimeter channels has been validated under the identified conditions described above.

It is complicated to compare OFI with the technologies develloped in Chapter I, knowing that OFI for microfluidics applications is still in a research stage, and that a large amount of its features remains not well understood. However, after this thesis, the following observations can be highlighted: OFI, like LDV is based on the Doppler effect undergone by a laser beam when it is reflected by particles. However, where LDV requires several optical components to be precisely aligned, the OFI optical system is made of a laser diode and a (or two) simple lens. Without the need of a complex beam alignment, OFI is a low cost, transportable sensor that can be used on various flow systems. The simplicity of manufacturing, coupled with a spatial and temporal resolution similar to LDV makes OFI a good alternative for flow measurement when the flow system is hard to access for example.

Although the spatial resolution of OFI is high enough to reconstruct flow distribution, full field techniques such as μ-PIV and dual slit remain more powerful tools to calculate flow distributions in channels smaller than 100 μm. For theoretical study such as rheology and turbulence in microfluidics, theses techniques are nowadays the most advanced in term of spatial resolution. However, techniques based on algorithms and particles tracking suffer from several drawbacks. First, the flow map reconstruction cannot be calculated in real time, and therefore rapid flow changes cannot be monitored. Then, theses techniques require optical access to the channel, so that the particles path can be reconstructed. This requirement is not suitable for in-vivo blood flow measurement. Finally, the use of bulky and expensive cameras makes theses sensor more appropriated for laboratory and research use rather than for industrial applications.

In term of low cost and ease of transportation, LASCA can be compared to OFI, but the spatial resolution may not be sufficient to accurately measure flow distribution in microchannels. To put it in a nutshell, OFI could be

an interesting technology for industrial and biomedical applications, offering a good compromise between simplicity, cost, spatial and temporal resolution.

The sensor presented here is a prototype that demonstrate the feasibility of OFI to measure accurately flow distribution in micro channels, and it gives an outline of OFI possibilities for fluidic applications.

First, OFI can be employed to study the fluid motion in microsystems, and provide a better understanding of fluid properties and behaviour in microchannels. OFI applied to microfluidics may be able to exploit certain fundamental properties of fluids moving in micrometre-scale channels. For example, surface effects that become increasingly dominant in microfluidics as the size is diminished are still nowadays not completely understood.

The monitoring of flow distribution during the manipulation of multiphase flows is an other strength of OFI. As a matter of fact, multiphase flows enable the generation and manipulation of monodisperse droplets of a dispersed gas or liquid phase in a continuous flow. These dispersions suggest new routes to the production of polymer particles, emulsions and foams. OFI can also being employed in micro mixing monitoring, where the flow velocity and distribution are key parameters to optimize the performance of mixing. The strong attractive feature of OFI for these applications consists in the fact that the sensor can be implemented directly in-situ for industrial applications. Consequently, there is no need of transporting the microsystem to a laboratory for analysis, leading to complexity and cost reduction.

OFI sensors can also be of great interest for various biomedical applications, and especially as a low-cost alternative of traditional flow sensors to monitor changes in skin blood flow. Theses changes can help to assess healing advancement in case of critical burn for example, or to detect Raynaud syndrome. Biomedical applications include also experimental investigations of skin blood flow in humans and animals, evaluation of the efficiency of vessels and of the circulatory restitution after reconstructive surgery. Furthermore, OFI could measure changes in skin blood flow perfusion due to delivery of vasoactive drugs. As mentioned in the introduction, a last biomedical application consists in meliorating the detection of some skin cancers by coupling visualisation methods (ABCD) with skin blood flow monitoring. Histologically, increasing malignancy is reflected by an increase of the vascularisation around the tumour. We believe that OFI blood flow rate measurement might allow differentiation between different types of skin tumours. A previous study has been performed using LDV, where the perfusion pattern of the entire tumour area has been visualized two-dimensionally [251] ; it was higher in the centre of the tumours than at the periphery for malignant melanomas and melanocytic naevi but was

149

the same throughout for basal cell carcinomas. Assessment of tumour blood flow and its pattern may be significant for prognostic prediction, and early evaluation of treatment response. Coupled with some technical advances, OFI could also be manufactured in a disposable skin cancer detector that can be used in private dermatologist office for clinical use.

Moreover, the full integration of optics, circuitry and fluidics opens new opportunities for the creation of compact biomedical microsystems. The main advantage of OFI over traditional techniques is to be ultimately manufactured into a portable device that can be held in the hand by the user. To reach this challenge, several technical changes have to be implemented.

First, the scanning mechanism is bulky and time consuming. To map a large area, it could be advantaging to remove this system, and build a matrix of OFI sensors. The use of VCSEL, which emits light on the top, is of great advantage to build a sensor's matrix that can be manufactured and tested directly on the wafer. Organizing the sensor in array improves the temporal resolution, as an entire flow map can be acquired in approximately 10 ms (corresponding to the time for one acquisition). This allows the measurement and observation of transient regime as well as turbulent flows, and rapid changes in the flow regime.
Then, the acquisition and signal processing has to be fully integrated into an autonomous chip, together with the circuitry. FPGA or DSP technologies are good candidates for the development of a fully integrated OFI sensor. Integration is crucial for miniaturized, low-cost optofluidic devices. A possible integration of lasers and microfluidics may be accomplished by soldering the laser chip to the lower surface of the microfluidic chip. The microfluidic chip usually consists of a PDMS chip covered by a thin glass slide protecting the channel. For full integration, photoresist microlenses can be directly etched on the glass slide. Then, the laser and the microfluidic chip can be merged using a removable adhesive. This provide a fully integrated sensor showing many advantages: in case of clogging of the microchannel, the electronics and optoelectronics part of the sensor car easily be removed and fixed on another chip, leading to cost reduction and simplicity of implementation.

In this thesis, only the use of OFI flowmeter as flow sensor has been demonstrated. However, OFI technology can be exploited to measure other parameters, due to the signal's high dependence on particle concentration and particle size. It may become an useful tool for characterizing and quantifying particle populations, and provide precise measurement to help improve product formulations in chemistry. For environmental purposes, OFI sensors could track particulate water pollution sources such as plastic particles coming from industrial waste flowing in the ocean.

OFI could also being employed for cell counting purposes, which has many applications in medicine and biology. As a matter of fact, the concentration of various blood cells, such as red blood cells and white blood cells, can give crucial information regarding the health situation of a person. Similarly, the concentration of bacteria, viruses and other pathogens in the blood or in other fluids can reveal information about the progress of an infectious disease and the degree of success with which the immune system is dealing with the infection.

Finally, it has been demonstrated theoretically that the OFI spectrum is dependent on the refractive index of the liquid phase. One of its major applications consists in sensing the molecular interactions in biological samples, proteins charaterisation and virus detection. As a matter of fact, virus characterization is based on index of refraction changes that occur upon binding of virus particles to antibodies. The availability of this type of diagnosis test for on-site analysis could be helpful in the control of various epidemics.

To conclude, the development of OFI for microfluidics applications has just begun, and it can be a powerful tool for microfluidics studies where the standard techniques are not applicable.

Glossary

α	Line-width enhancement factor or Henry factor
α_p	Coefficient representing the losses due to absorption by the semiconductor crystal
β_ν	Frequency modulation coefficient
β_I	Current modulation coefficient
C	Coupling coefficient
c	Speed of light
E(t)	Envelop of the electric field, normalized so that E corresponds to the photon density
E_i	Incident electric field
E_0	Incident wave amplitude
E_r	Reflected electric field
f_D	Doppler frequency
f_{shift}	Additional frequency shift induced by the driving current modulation
f_{mod}	Total frequency shift induced by the driving current modulation
Φ_0, Φ_F	Phase of the Electric field without (with) feedback
G_n	Modal gain coefficient
G_{gen}	Electric pumping coefficient
g_{th}	Threshold gain of the LD active region
g	Power gain of the LD active region
γ_0	Absorption coefficient of the LD active region
γ_{in} ,γ_{ext}	Absorption coefficient refering to the wave travelling inside (outside) the laser cavity
I	LD driving current
$\langle I \rangle$	Mean intensity of the photography (LASCA)
I_{eq}	Equivalent interface
K	Speckle contrast
k	Boltzmann constant
k_0	Wavenumber
$k_{\text{in}}, k_{\text{ext}}$	Incident (reflected) wavenumber
L	Distance between the laser and the target
L_s	Distance between two slits in DS technique
l_c	Length of the LD cavity
l_{ext}	Length of the external cavity
λ	Laser wavelength
m	Modulation index
n	Refractive index
$\overline{n_0}$	Effective group index
n_0, n_F	Effective index in freespace (resp. under feedback)
$N(t)$	Spatially averaged carrier density
N_0	Carrier density at transparency
N_{th}	Carrier density at threshold
ν_0, ν_F	LD frequency without (with) feedback

ω	Laser angular frequency
P_0, P_F	Laser optical feedback without (with) feedback
q	the elementary charge
r_1, r_2	Reflection coefficients for the electric field amplitude at I_1 (I_2)
r_{eq}	Reflection coefficient for the electric field amplitude for equivalent cavity
σ	LASCA spatial standard deviation
t	Time
τ_d	Time of flight in the external cavity
τ_l	Time of flight in the laser cavity
θ	Angle between the laser beam and the velocity of a target
V_T	Target velocity
V_A	Target velocity in the direction of the laser
W_0	Beam waist
x, y, z	Cartesian coordinates
Z_R	Rayleigh length

List of Publications

Papers in refereed journals:

Campagnolo L.,Nikolic M., Perchoux J., Lim YL., Bertling K., Loubière K., Prat L., Rakic A. Bosch T., *Flow profile measurement in microchannel using the optical feedback interferometry sensing technique*, Microfluidics and Nanofluidics, 1-7, **2012**.

Papers in international conference proceedings :

Campagnolo L., Roman S., Perchoux J., Lorthois S., *A new optical feedback interferometer for measuring red blood cell velocity distributions in individual capillaries : a feasibility study in microchannels*, Computer Methods in Biomechanics and Biomedical Engineering Vol. 15, Iss. sup1, **2012**

Nikolic M., Campagnolo L., Lim Y.L., Perchoux J, Wilson S.J., Rakic A.D., Bosch T., *Flow profile measurement in micro-channels using changes in laser junction voltage due to Self-mixing effect*, Sensors, 2011 IEEE , vol., no., pp.1394-1397, 28-31 Oct. **2011**

Campagnolo L.,Csont JC, Nikolic M., Perchoux J. and Bosch T. , *Measurement of flows in micro-channels through self-mixing effect in a laser diode* , 6th International Conference on Microtechnologies in Medicine and Biology (MMB) , Luzern, May **2011**.

Perchoux J., Campagnolo L., Lim YL, Rakic, A.D., *Lens-free self-mixing sensor for velocity and vibrations measurements*, Optoelectronic and Microelectronic Materials and Devices (COMMAD), 2010 Conference on , vol., no., pp.43-44, 12-15 Dec. **2010**

Papers in national conference proceedings :

Campagnolo L., Nikolic M., Perchoux J., *Vélocimetrie par réinjection optique appliquée à la mesure d'écoulements microfluidiques*, Mesures et Techniques Optiques pour l'Industrie Lille **2011**

Campagnolo L., Tanasoiu C., Perchoux J., *Discrimination du sens de deplacement par modulation d'une diode laser soumise à une réinjection optique*, Mesures et Techniques Optiques pour l'Industrie Toulouse-Labège **2010**

Appendix A: The Doppler effect
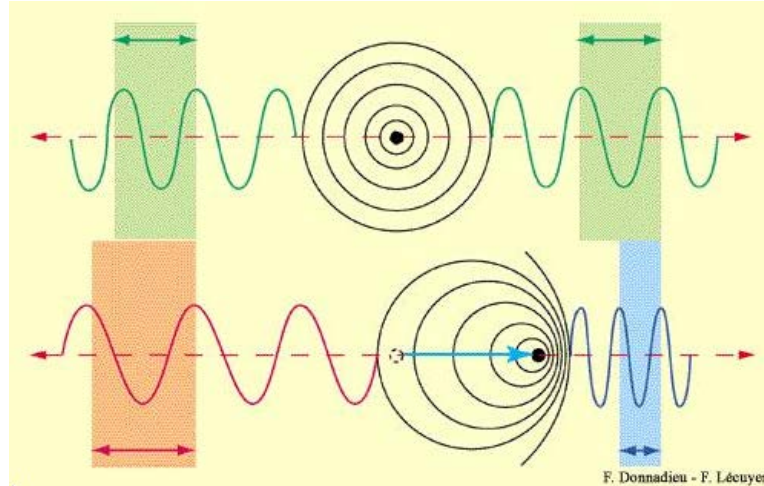
Figure V.1: Illustration of the Doppler effect. **Top**: The source is stationary, the wave frequency is the same in every spatial direction. **Bottom**: The source is moving, the frequency increases (decreases) when the source moves towards (away) an external observer.
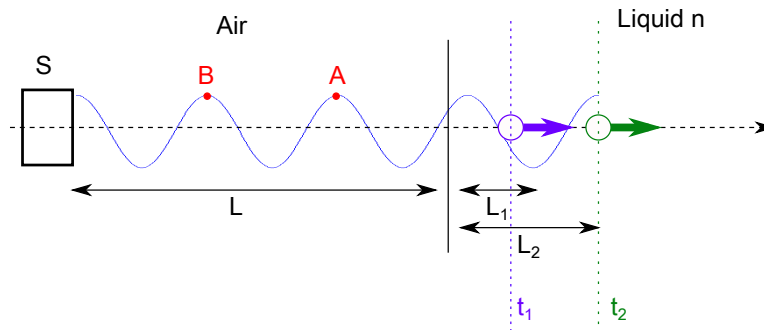
Figure V.2: Schematic arrangement for the Doppler effect in a fluid.

The Doppler effect has been discovered in 1842 by the Austrian physicist C. Doppler on sound waves, and the French scientist H. Fizeau discovered independently the same phenomenon on light waves in 1848. The Doppler effect is observed whenever the source of waves is moving with respect to an observer. Indeed, when a wave is incident on an observer (or object), the frequency of the wave perceived by the observer differs from the emitted frequency. If the object is moving towards the source, the perceived frequency is higher than the emitted frequency, and if it is moving away from the source, the perceived frequency is lower. The change in frequency or

155

Doppler shift that is observed by the object is $f_D = F_R - F_S$ where F_R is the received frequency and F_S is the emitted frequency.

Let consider the case of moving particle embedded in a surrounding liquid phase with a refractive index n, flowing in a flow-channel. The source is a laser situated at a distance L to the flow-channel wall, as depicted in Fig. V.2. The particle motion $\overline{V}$ is considered in the source direction, where $\overline{V}$ is an algebric value. At $t_0 = 0$, a sinusoidal wave leaves the source S. The particle perceived the first maximum (noted A) after a time $t_1 = L/c + nL_1/c$. The second maximum (noted B), that left the source after a time T_s corresponding to the period of the wave, arrives on the particle at $t_2 = L/c + nL_2/c$. The particle perceived points A and B separated with a time T_r, which differs from T_s, as the particle has moved during the propagation time. $L_2 - L_1$ is the distance travelled during T_r, and can be expressed as $L_2 - L_1 = \overline{V}T_r$.

So, T_r can be expressed as:

$$T_r = t_2 - t_1 = T_s + \frac{(L_2 - L_1)n}{c} \tag{V.5}$$

Yieldings,

$$T_r = \frac{T_s}{1 - \frac{\overline{V}n}{c}} \tag{V.6}$$

In frequency domain, the apparent frequency perceived by the particle is:

$$F_r = F_s \left(1 - \frac{\overline{V}n}{c} \right) \tag{V.7}$$

Leading to a frequency shift due to the Doppler effect f_D:

$$f_D = F_r - F_s = -\frac{\overline{V}n}{\lambda} \tag{V.8}$$

Where $\lambda = \frac{c}{F_s}$ is the wavelength of the wave.

In LDV case, the frequency shift is combined with the incident beam, and the resulting beat frequency is proportional to the particle velocity.

Appendix B: LDV application: In-vivo Blood flow measurement

LDV has been of great interest for various biomedical applications. However, the penetration depth of laser light in tissue varies approximately between 0.2 and 5 mm, so that LDV non-invasive blood flow measurement is restricted to subcutaneous microcirculation [252]. A schematic illustration for blood flow measurement using LDV technology is presented in Fig. V.3.
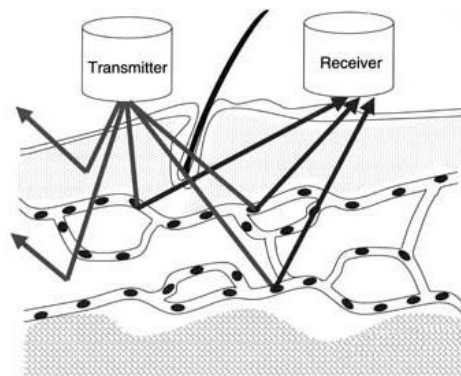
Figure V.3: LDV principle for in-vivo blood flow rate measurement

In 1972, Riva and co-workers first noticed the LDV potential for measuring in vivo blood velocities [253]. The laser was projected through an optical system into the blood and the light was scattered by the red blood cells. They also simplified the experimental set-up by removing the beamsplitter and using directly the light scattered by the tube itself as a local oscillator. This new configuration provides a simpler and easy sensor alignment. They measured the flow rate of blood in a synthetic 200µm flow-channel, and in the retinal artery of an albino rabbit.

Nevertheless, the principal interest of research groups working on LDV for biomedical applications was to build a practical instrument in order to measure human blood flow clinically.

Flow measurement in human retinal vessels was the easiest way to demonstrate that in-vivo human blood flow measurement was possible [84], insofar as the laser beam can be directly focused on the arteriole. The next step was to measure the human skin blood flow [13, 85]. A small and relatively inexpensive laser was used, in order to permit reasonable cost as well as portability, coupled with a fiber-optic probe that can be placed on any skin surface.
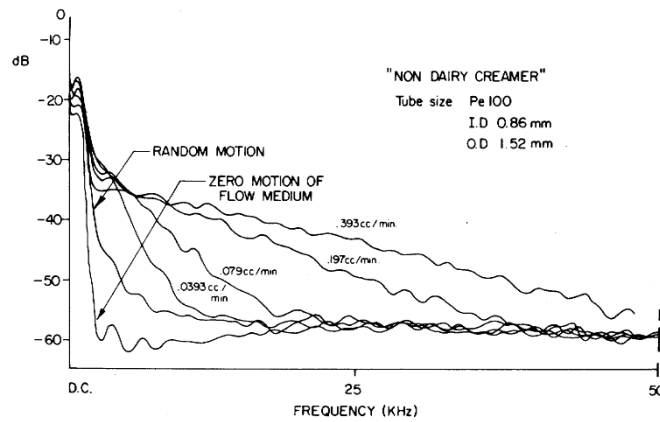
Figure V.4: First observation of multiple scattering effect in blood flow [13].

For the first time, the influence of the human skin on the LDV signal was observed. Indeed, the properties of the skin induce additional scattering effect, and the power spectrum of light does not exhibit a Doppler peak any more, but a statistical frequency repartition. Even though the spectrum varies with the average blood flow in the sensing volume, there is no longer an analytical relationship between the particle velocity and the Doppler beat frequency (Fig. V.4).

Bonner and Nassal [254] observed that very little of the backscattered luminescence derives from photons scattered only by the flowing blood cells, because photons generally suffer from several collisions with somatic cells, connective tissue, blood vessel walls, etc. before interacting with a blood cell. The effect of such interactions is to randomize the direction of the light which is incident upon the moving erythrocytes. They developed a model to show that the backscattered autocorrelation function and power spectrum depend on several parameter such as the particle density, size and scattering cross section. They also introduced a new signal processing, by showing the linear relationship between blood flow and the spectrum first moment.

Bonner also demonstrated that the quantity measured in laser Doppler monitoring or imaging is not the true flow rate but the perfusion [247]. The perfusion is the product of the local speed and concentration of blood cells [255], and the Laser Doppler sensors records the integrated perfusion within the sampling volume. This is one of the most sever limitation of LDV for in-vivo measurement, insofar as it is nowadays impossible to measure the shape of the velocity profile within a vessel surrounded by tissues [247].

158
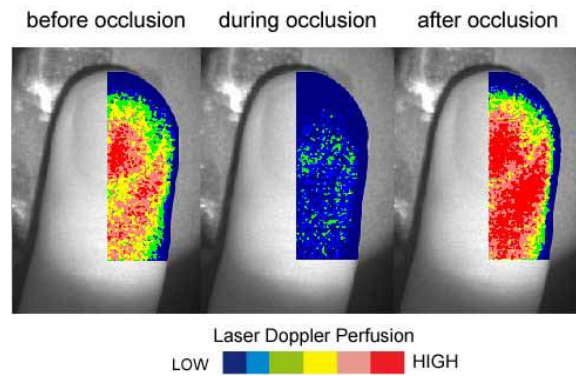
Figure V.5: LDV perfusion images of the finger obtained before, during, and after occlusion of the upper arm [14].

To avoid multiple scattering effect, and therefore improve LDV resolution for blood flow measurement, Chen et al. developed the Optical Doppler tomography (ODT) [256–258]. ODT combines LDV with optical coherence tomography (OCT) [259], by employing a low-coherence source (superluminescent diode) instead of a conventional laser diode. They successfully reconstructed the velocity profile of a 580 µm diameter channel imerged in a 1 mm thick scattering media that mimics skin [256].

Appendix C: Sensing volume estimation

The ray-transfer theory has been used to estimate the shape, position and size of the OFI sensing volume in flowchannels. This example described the case of the VCSEL based sensor, in dual lens configuration, beaming onto the 320 µm circular flowchannel.

The complex Gaussian beam parameter q_{in} is defined by:

$$\frac{1}{q_{\text{in}}} = \frac{1}{R} - j\frac{\lambda}{\pi W_{\text{in}}^2} \tag{V.9}$$

Where R is the radius of curvature of the beam, W_{in} represents the spot size at the laser output, and λ is the LD wavelength.

After travelling through an optical system, the complex Gaussian beam parameter becomes:

$$\frac{1}{q_{\text{out}}} = \frac{C + D\frac{1}{q_{\text{in}}}}{A + B\frac{1}{q_{\text{in}}}} \tag{V.10}$$

Where A, B, C and D are the components of M, the matrix that describes the optical system:

$$M = \begin{bmatrix} A & B \\ C & D \end{bmatrix} \tag{V.11}$$

To calculate the equivalent ray matrix of the optical system, the notations have been used described in Table. V.1. For a better visualisation of the results, typical numerical values are proposed. The first lens (L1) and the second lens (L2) can be chosen to adjust the sensing volume. In this example, the flowchannel (FC) is made of PDMS and has a circular cross-section. The liquid pushed through is milk diluted in water.

To measure the flow velocity using OFI techniques, a non-zero angle between the laser beam and the flow direction is required. This leads to an experimental set-up where the laser head is tilted with respect to the flowchannel. This tilt has to be taken into account while writing the matrix describing the optical set-up. The angle between the flowchannel and the laser beam is noted θ, the angle after refraction at the air/PDMS interface is noted $\theta_{\text{PDMS}} = n_{\text{air}}\theta/n_{\text{PDMS}}$, and the angle after refraction at the PDMS/liquid interface is noted $\theta_{\text{liquid}} = n_{\text{air}}\theta/n_{\text{liquid}}$.

Parameter	Description	Values
f_1	Focal length (L1)	11 mm
f_2	Focal length (L2)	8 mm
L_{air1}	Distance between the LD and L1	f_1
L_{air2}	Distance between L1 and L2	10 cm
L_{air3}	Distance between L2 and the FC	/
L_{pdms}	Distance FC first interface/ liquid	1.5 mm
L_{liquid}	Penetration depth in the liquid	/
n_{air}	Air refractive index	1
n_{pdms}	PDMS refractive index	1.41
n_{liquid}	Milk refractive index	1.35
θ	Angle between the laser beam and the channel	$25°$
λ	LD wavelength	667 nm
W_{in}	Laser beam waist	12.2 µm
r	Flowchannel radius	160 µm

Table V.1: Parameters used to describe the optical system

(a)   (b)
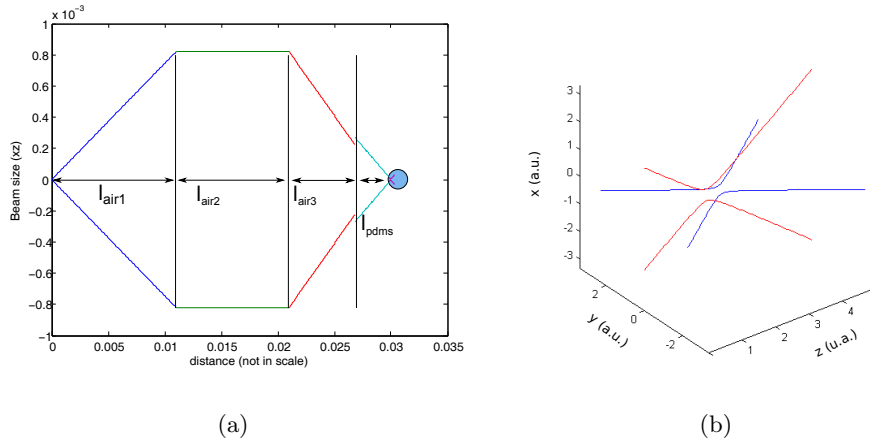
Figure V.6: (a) Ray transfer matrix are used to model the Gaussian beam propagation through the optical set-up. (b) The experimental configuration can lead to severe beam waist position change that needs to be taken into account while measuring flow rate in a microchannel.

Step description	Matrix
free space LD → L1	$M_{\text{air1}} = \begin{bmatrix} 1 & L_{\text{air1}} \\ 0 & 1 \end{bmatrix}$
Thin lens L1	$M_{\text{f1}} = \begin{bmatrix} 1 & 0 \\ \frac{-1}{f_1} & 1 \end{bmatrix}$
free space L1 → L2	$M_{\text{air2}} = \begin{bmatrix} 1 & L_{\text{air2}} \\ 0 & 1 \end{bmatrix}$
Thin lens L2	$M_{\text{f2}} = \begin{bmatrix} 1 & 0 \\ \frac{-1}{f_2} & 1 \end{bmatrix}$
free space L2 → PDMS	$M_{\text{air3}} = \begin{bmatrix} 1 & L_{\text{air3}} \\ 0 & 1 \end{bmatrix}$
Tilted interface PDMS/Air	$M_{\text{pdms-air-xz}} = \begin{bmatrix} \frac{\cos(\theta_{\text{PDMS}})}{\cos(\theta)} & 0 \\ 0 & \frac{n_{\text{air}}\cos(\theta)}{n_{\text{PDMS}}\cos(\theta_{\text{PDMS}})} \end{bmatrix}$
(Astigmatism)	$M_{\text{pdms-air-yz}} = \begin{bmatrix} 1 & 0 \\ 0 & \frac{n_{\text{air}}}{n_{\text{PDMS}}} \end{bmatrix}$
Propagation PDMS → Liquid	$M_{\text{pdms}} = \begin{bmatrix} 1 & L_{\text{pdms}} \\ 0 & 1 \end{bmatrix}$
Tilted and curved interface	$M_{\text{l-pdms-xz}} = \begin{bmatrix} \frac{\cos(\theta_{\text{liquid}})}{\cos(\theta_{\text{PDMS}})} & 0 \\ \frac{n_{\text{liquid}}\cos(\theta_{\text{liquid}}) - n_{\text{PDMS}}\cos(\theta_{\text{PDMS}})}{n_{\text{liquid}}r\cos(\theta_{\text{PDMS}})\cos(\theta_{\text{liquid}})} & \frac{n_{\text{PDMS}}\cos(\theta_{\text{PDMS}})}{n_{\text{liquid}}\cos(\theta_{\text{liquid}})} \end{bmatrix}$
Liquid/PDMS	$M_{\text{l-pdms-yz}} = \begin{bmatrix} 1 & 0 \\ \frac{n_{\text{liquid}}\cos(\theta_{\text{liquid}}) - n_{\text{PDMS}}\cos(\theta_{\text{PDMS}})}{n_{\text{liquid}}r} & \frac{n_{\text{PDMS}}}{n_{\text{liquid}}} \end{bmatrix}$
Propagation in liquid	$M_{\text{liquid}} = \begin{bmatrix} 1 & L_{\text{liquid}} \\ 0 & 1 \end{bmatrix}$

Table V.2: Ray transfer matrix for Gaussian beam

162

The optical path is divided in steps that are described with their respective ray matrix in Table. V.2.

To model the whole system, the ABCD matrix are multiplied, and the resulting matrix $M_x z$ et $M_y z$ describe the behaviour of the Gaussian beam in the plan (xz) and (yz). The beam propagation in the plan (xz) is plotted in Fig. IV.6, and the beam focus in the flowchannel is plotted in Fig. IV.6. From this simulation can be deduced that the sensing volume shape is ellipsoid, and this ellipsoid shape depends strongly on the angle between the laser beam and the flowchannel, the refractive index of the PDMS and the of the liquid, as well as on the radius of curvature of the flowchannel.

Therefore, to minimize the spot size, and to achieve a high spatial resolution in microchannels, the lens L1 and L2 have to be chosen carefully, the incident angle θ has to be close to $90°$, and square flowchannels has to be preferred to microchannels.

This model is not valid for multiple scattering regime (highly concentrated liquids) as the idea of focus, beam waist and Gaussian beam are not valid any more. Furthermore, this model is also not appropriated for biomedical applications, where the scattering due to skin has to be taken into account. However, it gives a good idea of what is happening in the flowchannel for in vitro measurement.

Appendix D: Microchannel fabrication

In microfluidics, a simple way to build microchannel is to use Polydimethylsiloxane (PDMS), which is an organic polymer of chemical formula: CH3[Si(CH3)2O]nSi(CH3)3. The state of the material varies with the parameter n, and PDMS without treatment can be liquid (low n) to quasi-solid (high n). Furthermore, PDMS is low-cost and hydrophobic, so that water or glycerol don't deform or leak into the flowchannels. Therefore, PDMS can be used without fearing from microchannel change and deformation.
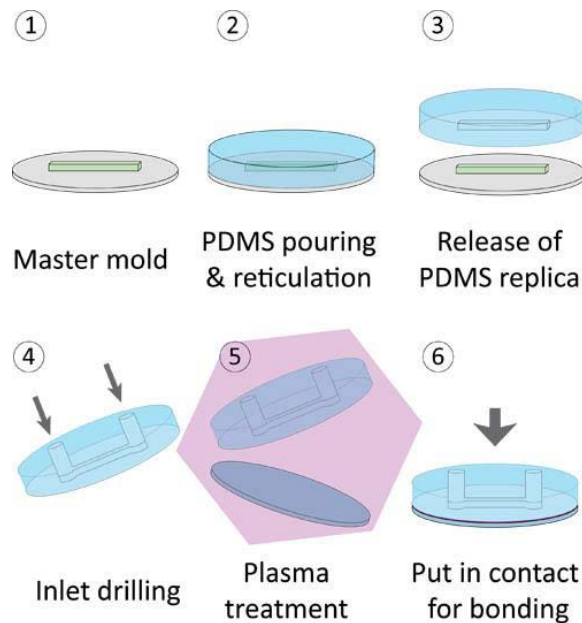
Figure V.7: Schematic description for rapid microchip fabrication using PDMS and softlithography technique.

The properties of PDMS can be changed by oxidation, as a plasma treatment modifies its surface chemistry. The PDMS can be bounded to PDMS or glass slices in a quasi-permanent manner.

Finally, PDMS is optically clear at visible wavelength (240 nm to 1100 nm), and can be easily observed using microscope. Theses advantages make PDMS flowchannels suitable for OFI flowmetry experimentations.

The experimental protocol to build square or rectangular microchannel is described in Fig. V.7.

- Liquid PDMS is mixed with a cross-linking agent (to harden the

PDMS), and the mix is poured into a mould made of using classic microelectronics fabrications techniques (photolithography on silicon master for example) Then, it is placed in a oven at low temperature (65 °) until it is hardened.

- Once the PDMS is hardened, it can be taken out of the mould, and a replica of the microchannel in PDMS is obtain.

- To allow the injection of fluids for future experiments, the inputs and outputs of the microfluidic device are drilled with a needle or a punch of the size of future outer tubes.

- Finally, the face of the PDMS block with micro-channels is bonded to a glass slide using a plasma treatment to close the microfluidic chip.

To build microchannels with a circular cross-section, no silicon master were used. PDMS was simply poured into a mould, with a fiber embedded in it. Once the PDMS is hardened, the fiber is gently pulled out.

Bibliography

[1] Y. Yeh and H. Z. Cummins. Localized fluid flow measurements with an hene laser spectrometer. *Applied Physics Letters*, 4(10):176 –178, may 1964.

[2] D. B. Barker and M. E. Fourney. Measuring fluid velocities with speckle patterns. *Opt. Lett.*, 1(4):135–137, Oct 1977.

[3] Ralph Lindken, Massimiliano Rossi, Sebastian Grosse, and Jerry Westerweel. Micro-particle image velocimetry ([small micro]piv): Recent developments, applications, and guidelines. *Lab Chip*, 9:10–11, 2009.

[4] S. Devasenathipathy, JG Santiago, ST Wereley, CD Meinhart, and K. Takehara. Particle imaging techniques for microfabricated fluidic systems. *Experiments in Fluids*, 34(4):504–514, 2003.

[5] K. Takehara, RJ Adrian, GT Etoh, and KT Christensen. A kalman tracker for super-resolution piv. *Experiments in fluids*, 29:34–41, 2000.

[6] F. Sarrazin, K. Loubiere, L. Prat, C. Gourdon, T. Bonometti, and J. Magnaudet. Experimental and numerical study of droplets hydrodynamics in microchannels. *AIChE journal*, 52(12):4061–4070, 2006.

[7] J.D. Briers. Laser speckle contrast imaging for measuring blood flow. *Optica Applicata*, 37(1/2):139, 2007.

[8] Hitoshi Fujii, Kunihiko Nohira, Yuhei Yamamoto, Hiroharu Ikawa, and Takehiko Ohura. Evaluation of blood flow by laser speckle image sensing. part 1. *Appl. Opt.*, 26(24):5321–5325, Dec 1987.

[9] H. Fujii. Visualisation of retinal blood flow by laser speckle flowgraphy. *Medical and Biological Engineering and Computing*, 32:302–304, 1994. 10.1007/BF02512526.

[10] F.F.M. Mul, MH Koelink, AL Weijers, J. Greve, JG Aarnoudse, R. Graaff, and ACM Dassel. Self-mixing laser-doppler velocimetry of liquid flow and of blood perfusion in tissue. *Applied optics*, 31(27):5844–5851, 1992.

[11] K. Mito, H. Ikeda, M. Sumi, and S. Shinohara. Self-mixing effect of the semiconductor laser doppler method for blood flow measurement. *Medical and Biological Engineering and Computing*, 31(3):308–310, 1993.

[12] C. Zakian and M. Dickinson. Laser doppler imaging through tissues phantoms by using self-mixing interferometry with a laser diode. *OPTICS LETTERS*, 32(19):2798, 2007.

[13] Dennis Watkins and G. Allen Holloway. An instrument to measure cutaneous blood flow using the doppler shift of laser light. *Biomedical Engineering, IEEE Transactions on*, BME-25(1):28 –33, jan. 1978.

[14] Alexandre Serov and Theo Lasser. High-speed laser doppler perfusion imaging using an integrating cmos image sensor. *Opt. Express*, 13(17):6416–6428, Aug 2005.

[15] N.E. Dorsey. Properties of ordinary water-substance, in all its phases: water-vapor, water and all the ices. *American chemical society Monograph Series*, 1968.

[16] Carlo S. Effenhauser, Andreas Manz, and H. Michael Widmer. Glass chips for high-speed capillary electrophoresis separations with submicrometer plate heights. *Analytical Chemistry*, 65(19):2637–2642, 1993.

[17] A. Manz, N. Graber, and H.M. Widmer. Miniaturized total chemical analysis systems: A novel concept for chemical sensing. *Sensors and Actuators B: Chemical*, 1:244–248, 1990.

[18] D.C. Duffy, J.C. McDonald, O.J.A. Schueller, and G.M. Whitesides. Rapid prototyping of microfluidic systems in poly (dimethylsiloxane). *Analytical Chemistry*, 70(23):4974–4984, 1998.

[19] Milan Mrksich and George M. Whitesides. Patterning self-assembled monolayers using microcontact printing: A new technology for biosensors? *Trends in Biotechnology*, 13(6):228 – 235, 1995.

[20] Xiao-Mei Zhao, Younan Xia, and George M. Whitesides. Fabrication of three-dimensional micro-structures: Microtransfer molding. *Advanced Materials*, 8(10):837–840, 1996.

[21] B.-H. Jo, L.M. Van Lerberghe, K.M. Motsegood, and D.J. Beebe. Three-dimensional micro-channel fabrication in polydimethylsiloxane (pdms) elastomer. *Microelectromechanical Systems, Journal of*, 9(1):76 –81, mar 2000.

[22] B. A. Grzybowski, R. Haag, N. Bowden, and G. M. Whitesides. Generation of micrometer-sized patterns for microanalytical applications using a laser direct-write method and microcontact printing. *Analytical Chemistry*, 70(22):4645–4652, 1998.

[23] Irene Fernandez-Cuesta, Anna Laura Palmarelli, Xiaogan Liang, Jingyu Zhang, Scott Dhuey, Deirdre Olynick, and Stefano Cabrini. Fabrication of fluidic devices with 30 nm nanochannels by direct imprinting. *Journal of Vacuum Science & Technology B: Microelectronics and Nanometer Structures*, 29(6):06F801, 2011.

[24] C. Yi, C.W. Li, S. Ji, and M. Yang. Microfluidics technology for manipulation and analysis of biological cells. *Analytica Chimica Acta*, 560(1):1–23, 2006.

[25] C. Zhang, J. Xu, W. Ma, and W. Zheng. Pcr microfluidic devices for dna amplification. *Biotechnology advances*, 24(3):243–284, 2006.

[26] A. Bange, H.B. Halsall, and W.R. Heineman. Microfluidic immunosensor systems. *Biosensors and Bioelectronics*, 20(12):2488–2503, 2005.

[27] C. Situma, M. Hashimoto, and S.A. Soper. Merging microfluidics with microarray-based bioassays. *Biomolecular engineering*, 23(5):213–231, 2006.

[28] H.C. Fan, Y.J. Blumenfeld, Y.Y. El-Sayed, J. Chueh, and S.R. Quake. Microfluidic digital pcr enables rapid prenatal diagnosis of fetal aneuploidy. *American journal of obstetrics and gynecology*, 200(5):543–e1, 2009.

[29] T.D. Chung and H.C. Kim. Recent advances in miniaturized microfluidic flow cytometry for clinical use. *Electrophoresis*, 28(24):4511–4520, 2007.

[30] L. Cao, S. Mantell, and D. Polla. Implantable medical drug delivery systems using microelectromechanical systems technology. In *Microtechnologies in Medicine and Biology, 1st Annual International, Conference On. 2000*, pages 487–490. IEEE, 2000.

[31] D.L. Polla, A.G. Erdman, W.P. Robbins, D.T. Markus, J. Diaz-Diaz, R. Rizq, Y. Nam, H.T. Brickner, A. Wang, and P. Krulevitch. Microdevices in medicine 1. *Annual review of biomedical engineering*, 2(1):551–576, 2000.

[32] H. Song, D.L. Chen, and R.F. Ismagilov. Reactions in droplets in microfluidic channels. *Angewandte chemie international edition*, 45(44):7336–7356, 2006.

[33] X. Niu, M. Zhang, S. Peng, W. Wen, and P. Sheng. Real-time detection, control, and sorting of microfluidic droplets. *Biomicrofluidics*, 1:044101, 2007.

[34] Y. Zhan, J. Wang, N. Bao, and C. Lu. Electroporation of cells in microfluidic droplets. *Analytical chemistry*, 81(5):2027–2031, 2009.

[35] Y.C. Tan, K. Hettiarachchi, M. Siu, Y.R. Pan, and A.P. Lee. Controlled microfluidic encapsulation of cells, proteins, and microbeads in lipid vesicles. *Journal of the American Chemical Society*, 128(17):5656–5658, 2006.

[36] M. Washizu. Electrostatic actuation of liquid droplets for micro-reactor applications. *Industry Applications, IEEE Transactions on*, 34(4):732–737, 1998.

[37] L.F. Cheow, L. Yobas, and D.L. Kwong. Digital microfluidics: Droplet based logic gates. *Applied physics letters*, 90(5):054107–054107, 2007.

[38] C.J. Pipe and G.H. McKinley. Microfluidic rheometry. *Mechanics Research Communications*, 36(1):110–120, 2009.

[39] WB Zimmerman, JM Rees, and TJ Craven. Rheometry of non-newtonian electrokinetic flow in a microchannel t-junction. *Microfluidics and Nanofluidics*, 2(6):481–492, 2006.

[40] HC Hemaka Bandalusena, W.B. Zimmerman, and J.M. Rees. Microfluidic rheometry of a polymer solution by micron resolution particle image velocimetry: a model validation study. *Measurement Science and Technology*, 20:115404, 2009.

[41] V. Berejnov, N. Djilali, and D. Sinton. Lab-on-chip methodologies for the study of transport in porous media: energy applications. *Lab Chip*, 8(5):689–693, 2008.

[42] J. Koo and C. Kleinstreuer. Liquid flow in microchannels: experimental observations and computational analyses of microfluidics effects. *Journal of Micromechanics and Microengineering*, 13:568, 2003.

[43] T.M. Squires and S.R. Quake. Microfluidics: Fluid physics at the nanoliter scale. *Reviews of modern physics*, 77(3):977, 2005.

[44] E. Lauga, M.P. Brenner, and H.A. Stone. Microfluidics: the no-slip boundary condition. *Arxiv preprint cond-mat/0501557*, 2005.

[45] E.A. Mansur, M. Ye, Y. Wang, and Y. Dai. A state-of-the-art review of mixing in microfluidic mixers. *Chinese Journal of Chemical Engineering*, 16(4):503–516, 2008.

[46] B. He, B.J. Burke, X. Zhang, R. Zhang, and F.E. Regnier. A picoliter-volume mixer for microfluidic analytical systems. *Analytical chemistry*, 73(9):1942–1947, 2001.

[47] W.Y. Lin, Y. Wang, S. Wang, and H.R. Tseng. Integrated microfluidic reactors. *Nano Today*, 4(6):470–481, 2009.

[48] S.J. Haswell and V. Skelton. Chemical and biochemical microreactors. *TrAC Trends in Analytical Chemistry*, 19(6):389–395, 2000.

[49] D. Erickson and D. Li. Integrated microfluidic devices. *Analytica Chimica Acta*, 507(1):11–26, 2004.

[50] J.C.T. Eijkel and A. Berg. Nanofluidics: what is it and what can we expect from it? *Microfluidics and Nanofluidics*, 1(3):249–267, 2005.

[51] S.E. Charm and G.S. Kurland. *Blood flow and microcirculation*, volume 14. Wiley, 1974.

[52] D. Park, J. Hwang, K. Jang, D. Han, K. Ahn, and B. Baik. Use of laser doppler flowmetry for estimation of the depth of burns. *Plastic and reconstructive surgery*, 101(6):1516, 1998.

[53] G. McHedlishvili, N. Maeda, et al. Blood flow structure related to red cell flow: determinant of blood fluidity in narrow microvessels. *The Japanese journal of physiology*, 51(1):19, 2001.

[54] J.J. Bishop, P.R. Nance, A.S. Popel, M. Intaglietta, and P.C. Johnson. Effect of erythrocyte aggregation on velocity profiles in venules. *American Journal of Physiology-Heart and Circulatory Physiology*, 280(1):H222–H236, 2001.

[55] H.H. Lipowsky. Microvascular rheology and hemodynamics. *Microcirculation*, 12(1):5–15, 2005.

[56] AR Pries, TW Secomb, et al. Rheology of the microcirculation. *Clinical hemorheology and microcirculation*, 29(3):143–148, 2003.

[57] F. Nachbar, W. Stolz, T. Merkle, A.B. Cognetta, T. Vogt, M. Landthaler, P. Bilek, O. Braun-Falco, and G. Plewig. The abcd rule of dermatoscopy: high prospective value in the diagnosis of doubtful melanocytic skin lesions. *Journal of the American Academy of Dermatology*, 30(4):551–559, 1994.

[58] M Stucker, M. Esser, M. Hoffmann, U. Memmel, A.H. LLER, C. Von Bormann, K. Hoffmann, and P. Altmeyer. High-resolution laser doppler perfusion imaging aids in differentiating between benign and malignant melanocytic skin tumours. *Acta Derm Venereol*, 82:25–29, 2002.

[59] M. Stücker, C. Springer, V. Paech, N. Hermes, M. Hoffmann, and P. Altmeyer. Increased laser doppler flow in skin tumors corresponds to elevated vessel density and reactive hyperemia. *Skin Research and Technology*, 12(1):1–6, 2006.

[60] M.J.W. Povey. *Ultrasonic techniques for fluids characterization*. Academic Pr, 1997.

[61] Y. Takeda. Velocity profile measurement by ultrasonic doppler method. *Experimental thermal and fluid science*, 10(4):444–453, 1995.

[62] R. Tabrizchi and M.K. Pugsley. Methods of blood flow measurement in the arterial circulatory system. *Journal of pharmacological and toxicological methods*, 44(2):375–384, 2000.

[63] M.A. Smith. The measurement and visualisation of vessel blood flow by magnetic resonance imaging. *Clinical Physics and Physiological Measurement*, 11:101, 1990.

[64] WG Bradley Jr and V. Waluch. Blood flow: magnetic resonance imaging. *Radiology*, 154(2):443–450, 1985.

[65] M.A. Lodge, H. Braess, F. Mahmoud, J. Suh, N. Englar, S. Geyser-Stoops, J. Jenkins, S.L. Bacharach, V. Dilsizian, et al. Developments in nuclear cardiology: transition from single photon emission computed tomography to positron emission tomography-computed tomography. *The Journal of invasive cardiology*, 17(9):491, 2005.

[66] A. Cuocolo, W. Acampa, M. Imbriaco, N. De Luca, GL Iovino, M. Salvatore, et al. The many ways to myocardial perfusion imaging. *The quarterly journal of nuclear medicine and molecular imaging: official publication of the Italian Association of Nuclear Medicine (AIMN)[and] the International Association of Radiopharmacology (IAR),[and] Section of the Society of..*, 49(1):4, 2005.

[67] H. Zhao, R.H. Webb, and B. Ortel. Review of noninvasive methods for skin blood flow imaging in microcirculation. *Journal of Clinical Engineering*, 27(1):40, 2002.

[68] J.D. Anderson and J.F. Wendt. *Computational fluid dynamics*, volume 206. McGraw-Hill, 1995.

[69] TJ Chung. *Computational fluid dynamics*. Cambridge Univ Pr, 2010.

[70] D. Sinton. Microscale flow visualization. *Microfluidics and Nanofluidics*, 1:2–21, 2004. 10.1007/s10404-004-0009-4.

[71] B R Clayton and B S Massey. Flow visualization in water: a review of techniques. *Journal of Scientific Instruments*, 44(1):2, 1967.

[72] H. Z. Cummins, N. Knable, and Y. Yeh. Observation of diffusion broadening of rayleigh scattered light. *Phys. Rev. Lett.*, 12:150–153, Feb 1964.

[73] E.W. Washburn. The dynamics of capillary flow. *Physical review*, 17(3):273, 1921.

[74] J. Foreman, E. George, J. Jetton, R. Lewis, J. Thornton, and H. Watson. 8c2–fluid flow measurements with a laser doppler velocimeter. *Quantum Electronics, IEEE Journal of*, 2(8):260 − 266, aug 1966.

[75] M J Rudd. A new theoretical model for the laser dopplermeter. *Journal of Physics E: Scientific Instruments*, 2(1):55, 1969.

[76] K. Kyuma, S. Tai, K. Hamanaka, and M. Nunoshita. Laser doppler velocimeter with a novel optical fiber probe. *Applied Optics*, 20(14):2424–2427, 1981.

[77] F. F. M. de Mul, J. van Spijker, D. van der Plas, J. Greve, J. G. Aarnoudse, and T. M. Smits. Mini laser-doppler (blood) flow monitor with diode laser source and detection integrated in the probe. *Appl. Opt.*, 23(17):2970–2973, Sep 1984.

[78] D. Dopheide, M. Faber, G. Reim, and G. Taux. Laser and avalanche diodes for velocity measurement by laser doppler anemometry. *Experiments in Fluids*, 6:289–297, 1988. 10.1007/BF00538819.

[79] R J Adrian. A bipolar, two component laser-doppler velocimeter. *Journal of Physics E: Scientific Instruments*, 8(9):723, 1975.

[80] K A Blake. Simple two-dimensional laser velocimeter optics. *Journal of Physics E: Scientific Instruments*, 5(7):623, 1972.

[81] George R. Grant and Kenneth L. Orloff. Two-color dual-beam backscatter laser doppler velocimeter. *Appl. Opt.*, 12(12):2913–2916, Dec 1973.

[82] D. B. Brayton, H. T. Kalb, and F. L. Crosswy. Two-component dual-scatter laser doppler velocimeter with frequency burst signal readout. *Appl. Opt.*, 12(6):1145–1156, Jun 1973.

[83] Alexander Serov, Wiendelt Steenbergen, and Frits De Mul. Laser doppler perfusion imaging with a complimentary metal oxide semiconductor image sensor. *Optics Letters*, 27(5):300 − 302, 2002.

[84] Toyoichi Tanaka, Charles Riva, and Isaac Ben-Sira. Blood velocity measurements in human retinal vessels. *Science*, 186(4166):830–831, 1974.

[85] M.D. Stern. In vivo evaluation of microcirculation by coherent light scattering. *Nature*, 254(5495):56 – 8, 1975. in vivo;evaluation if microcirculation;coherent light scattering;noninvasive method;microvascular compartments;flow velocities;laser Doppler spectroscopy;.

[86] Alexandre Serov, Beda Steinacher, and Theo Lasser. Full-field laser doppler perfusion imaging and monitoring with an intelligent cmos camera. *Opt. Express*, 13(10):3681–3689, May 2005.

[87] DA Compton and JK Eaton. A high-resolution laser doppler anemometer for three-dimensional turbulent boundary layers. *Experiments in fluids*, 22(2):111–117, 1996.

[88] AK Tieu, MR Mackenzie, and EB Li. Measurements in microscopic flow with a solid-state lda. *Experiments in fluids*, 19(4):293–294, 1995.

[89] L. Büttner, C. Skupsch, J. König, J. Czarske, et al. Optic simulation and optimization of a laser doppler velocity profile sensor for microfluidic applications. *Optical Engineering*, 49:073602, 2010.

[90] J. König, A. Voigt, L. Büttner, and J. Czarske. Precise micro flow rate measurements by a laser doppler velocity profile sensor with time division multiplexing. *Measurement Science and Technology*, 21:074005, 2010.

[91] R. Grousson and S. Mallick. Study of flow pattern in a fluid by scattered laser light. *Appl. Opt.*, 16(9):2334–2336, Sep 1977.

[92] John Dainty, Anthony Ennos, Maurice Francon, Joseph Goodman, Thomas McKechnie, Gareth Parry, and J. Goodman. Statistical properties of laser speckle patterns. In *Laser Speckle and Related Phenomena*, volume 9 of *Topics in Applied Physics*, pages 9–75. Springer Berlin / Heidelberg, 1975. 10.1007/BFb0111436.

[93] J.M. Burch and J.M.J. Tokarski. Production of multiple beam fringes from photographic scatterers. *Optica Acta: International Journal of Optics*, 15(2):101–111, 1968.

[94] R.J. Binnington, G.J. Troup, and D.V. Boger. A low cost laser-speckle photographic technique for velocity measure-

ment in slow flows. *Journal of Non-Newtonian Fluid Mechanics*, 12(3):255 – 267, 1983.

[95] MA Sutton, WJ Wolters, WH Peters, WF Ranson, and SR McNeill. Determination of displacements using an improved digital correlation method. *Image and Vision Computing*, 1(3):133 – 139, 1983.

[96] C. J. D. Pickering and N. A. Halliwell. Laser speckle photography and particle image velocimetry: photographic film noise. *Appl. Opt.*, 23(17):2961–2969, Sep 1984.

[97] N. Barakat, H. El-Ghandoor, W. Merzkirch, and U. Wernekinck. Speckle velocimetry applied to pipe flow. *Experiments in Fluids*, 6:71–72, 1988. 10.1007/BF00226139.

[98] J.M. Coupland, C.J.D. Pickering, and N.A. Halliwell. Particle image velocimetry: theory of directional ambiguity removal using holographic image separation. *Applied optics*, 26(9):1576–1578, 1987.

[99] A. Cenedese and A. Paglialunga. A new technique for the determination of the third velocity component with piv. *Experiments in Fluids*, 8:228–230, 1989. 10.1007/BF00195799.

[100] HG Maas, A. Gruen, and D. Papantoniou. Particle tracking velocimetry in three-dimensional flows. *Experiments in Fluids*, 15(2):133–146, 1993.

[101] NA Malik, T. Dracos, and DA Papantoniou. Particle tracking velocimetry in three-dimensional flows. *Experiments in Fluids*, 15(4):279–294, 1993.

[102] RD Keane, RJ Adrian, and Y. Zhang. Super-resolution particle imaging velocimetry. *Measurement Science and Technology*, 6:754, 1995.

[103] A. Stitou and ML Riethmuller. Extension of piv to super resolution using ptv. *Measurement Science and Technology*, 12:1398, 2001.

[104] R.D. Keane and R.J. Adrian. Prospects for super-resolution with particle image velocimetry. In *Proceedings of SPIE*, volume 283, 2005.

[105] J. G. Santiago, S. T. Wereley, C. D. Meinhart, D. J. Beebe, and R. J.

Adrian. A particle image velocimetry system for microfluidics. *Experiments in Fluids*, 25:316–319, 1998. 10.1007/s003480050235.

[106] C. D. Meinhart, S. T. Wereley, and J. G. Santiago. Piv measurements of a microchannel flow. *Experiments in Fluids*, 27:414–419, 1999. 10.1007/s003480050366.

[107] M.G. Olsen and R.J. Adrian. Brownian motion and correlation in particle image velocimetry. *Optics & Laser Technology*, 32(7-8):621–627, 2000.

[108] N. Erkan, K. Shinohara, S. Someya, and K. Okamoto. Three-component velocity measurement in microscale flows using time-resolved piv. *Measurement Science and Technology*, 19:057003, 2008.

[109] H.S. Chuang, L. Gui, and S.T. Wereley. Nano-resolution flow measurement based on single pixel evaluation piv. *Microfluidics and Nanofluidics*, pages 1–16, 2012.

[110] S.J. Williams, C. Park, and S.T. Wereley. Advances and applications on microfluidic velocimetry techniques. *Microfluidics and Nanofluidics*, 8(6):709–726, 2010.

[111] Y. Sugii, S. Nishio, and K. Okamoto. In vivo piv measurement of red blood cell velocity field in microvessels considering mesentery motion. *Physiological Measurement*, 23:403, 2002.

[112] P. Vennemann, K.T. Kiger, R. Lindken, B.C.W. Groenendijk, S. Stekelenburg-de Vos, T.L.M. Ten Hagen, N.T.C. Ursem, R.E. Poelmann, J. Westerweel, and B.P. Hierck. In vivo micro particle image velocimetry measurements of blood-plasma in the embryonic avian heart. *Journal of biomechanics*, 39(7):1191–1200, 2006.

[113] AF Fercher and JD Briers. Flow visualization by means of single-exposure speckle photography. *Optics communications*, 37(5):326–330, 1981.

[114] J. W. Goodman. *Laser Speckle and Related Phenomena*, chapter Statistical Properties of Laser Speckle Patterns, pages 9 – 75. Springer-Verlag, 1975.

[115] J D Briers and A F Fercher. Retinal blood-flow visualization by means of laser speckle photography. *Investigative Ophthalmology & Visual Science*, 22(2):255–9, 1982.

[116] D.A. Boas and A.K. Dunn. Laser speckle contrast imaging in biomedical optics. *Journal of biomedical optics*, 15:011109, 2010.

[117] M. Draijer, E. Hondebrink, T. Van Leeuwen, and W. Steenbergen. Review of laser speckle contrast techniques for visualizing tissue perfusion. *Lasers in medical science*, 24(4):639–651, 2009.

[118] JD Briers. Wavelength dependence of intensity fluctuations in laser speckle patterns from biological specimens. *Optics Communications*, 13(3):324–326, 1975.

[119] Y. Aizu, H. Ambar, T. Yamamoto, and T. Asakura. Measurements of flow velocity in a microscopic region using dynamic laser speckles based on the photon correlation. *Optics Communications*, 72(5):269–273, 1989.

[120] Y. Aizu and T. Asakura. Bio-speckle phenomena and their application to the evaluation of blood flow. *Optics & Laser Technology*, 23(4):205–219, 1991.

[121] B. Ruth. Superposition of two dynamic speckle patterns. *Journal of Modern Optics*, 34(2):257–273, 1987.

[122] B. Ruth. Non-contact blood flow determination using a laser speckle method. *Optics & Laser Technology*, 20(6):309–316, 1988.

[123] B. Ruth. Blood flow determination by the laser speckle method. *International journal of microcirculation, clinical and experimental/sponsored by the European Society for Microcirculation*, 9(1):21, 1990.

[124] B. Ruth. Measuring the steady-state value and the dynamics of the skin blood flow using the non-contact laser speckle method. *Medical engineering & physics*, 16(2):105–111, 1994.

[125] H. Wayland and P.C. Johnson. Erythrocyte velocity measurement in microvessels by a two-slit photometric method. *Journal of applied physiology*, 22(2):333–337, 1967.

[126] P. Gaehtgens, H.J. Meiselman, and H. Wayland. Erythrocyte flow velocities in mesenteric microvessels of the cat. *Microvascular Research*, 2(2):151–162, 1970.

[127] H. Wayland. Photosensor methods of flow measurement in the microcirculation. *Microvascular Research*, 5(3):336–350, 1973.

[128] M. Intaglietta, NR Silverman, and WR Tompkins. Capillary flow velocity measurements in vivo and in situ by television methods. *Microvascular research*, 10(2):165–179, 1975.

[129] F. Sapuppo, M. Bucolo, M. Intaglietta, P.C. Johnson, L. Fortuna, and P. Arena. An improved instrument for real-time measurement of blood flow velocity in microvessels. *Instrumentation and Measurement, IEEE Transactions on*, 56(6):2663–2671, 2007.

[130] S Roman, S Lorthois, P Duru, and F Risso. An optimized technique for red blood cells velocity measurement in microvessels. *J. Biomech.*, 2012.

[131] Sophie Roman, Sylvie Lorthois, Paul Duru, and Frederic Risso. Velocimetry of red blood cells in microvessels by the dual-slit method: Effect of velocity gradients. *Microvascular Research*, (0):–, 2012.

[132] M.H. Koelink, M. Slot, F.F.M. de Mul, J. Greve, R. Graaff, A.C.M. Dassel, and J.G. Aarnoudse. Laser doppler velocimeter based on the self-mixing effect in a fiber-coupled semiconductor laser: theory. *Applied Optics*, 31(18):3401 – 3408, 1992.

[133] MH Koelink, FFM De Mul, AL Weijers, J. Greve, R. Graaff, ACM Dassel, and JG Aarnoudse. Fiber-coupled self-mixing diode-laser doppler velocimeter: technical aspects and flow velocity profile disturbances in water and blood flows. *Applied optics*, 33(24):5628–5641, 1994.

[134] A.P. Shepherd and P.Å. Öberg. *Laser-Doppler blood flowmetry*, volume 107. Springer, 1990.

[135] FFM De Mul, MH Koelink, AL Weijers, J. Greve, JG Aarnoudse, R. Graaff, and ACM Dassel. A semiconductor laser used for direct measurement of the blood perfusion of tissue. *Biomedical Engineering, IEEE Transactions on*, 40(2):208–210, 1993.

[136] J. Hast, R. Myllylä, H. Sorvoja, and J. Miettinen. Self-mixing interferometry in noninvasive pulse wave velocity measurement. *Molecular and Quantum Acoustics*, 22:95–106, 2001.

[137] J.T. Hast, R.A. Myllylae, H. Sorvoja, and S.M. Nissilae. Baroreflex regulation measurement using a noninvasive laser doppler method. In *Proceedings of SPIE*, volume 4251, page 232, 2001.

[138] J. Hast, R. Myllylä, H. Sorvoja, and J. Miettinen. Arterial pulse shape measurement using self-mixing effect in a diode laser. *Quantum Electronics*, 32:975, 2002.

[139] J.T. Hast, R.A. Myllyla, H. Sorvoja, and J. Miettinen. Arterial pulse shape measurement using self-mixing inteferometry. In *Proceedings of SPIE*, volume 4956, page 341, 2003.

[140] J.T. Hast, R.A. Myllylae, H. Sorvoja, and S.M. Nissilae. Arterial compliance measurement using a noninvasive laser doppler measurement system. In *Proceedings of SPIE*, volume 4163, page 24, 2000.

[141] C. Zakian, M. Dickinson, and T. King. Particle sizing and flow measurement using self-mixing interferometry with a laser diode. *Journal of Optics A: Pure and Applied Optics*, 7:S445, 2005.

[142] C. Zakian, M. Dickinson, and T. King. Dynamic light scattering by using self-mixing interferometry with a laser diode. *Applied optics*, 45(10):2240–2245, 2006.

[143] M. Norgia, A. Pesatori, and L. Rovati. Optical flowmeter for blood extracorporeal circulators. In *Instrumentation and Measurement Technology Conference, 2009. I2MTC'09. IEEE*, pages 1759–1762. IEEE, 2009.

[144] M. Norgia, A. Pesatori, and L. Rovati. Low-cost optical flowmeter with analog front-end electronics for blood extracorporeal circulators. *Instrumentation and Measurement, IEEE Transactions on*, 59(5):1233–1239, 2010.

[145] L. Rovati, S. Cattini, and N. Palanisamy. Measurement of the fluid-velocity profile using a self-mixing superluminescent diode. *Measurement Science and Technology*, 22:025402, 2011.

[146] H. Wang, J. Shen, B. Wang, B. Yu, and Y. Xu. Laser diode feedback interferometry in flowing brownian motion system: a novel theory. *Applied Physics B: Lasers and Optics*, 101(1):173–183, 2010.

[147] H. Wang and J. Shen. Power spectral density of self-mixing signals from a flowing brownian motion system. *Applied Physics B: Lasers and Optics*, pages 1–8, 2012.

[148] Y.L. Lim, R. Kliese, K. Bertling, K. Tanimizu, PA Jacobs, and A.D. Rakic. Self-mixing flow sensor using a monolithic vcsel array with parallel readout. *Optics Express*, 18(11):11720–11727, 2010.

[149] R. Kliese, Y.L. Lim, E. Stefan, J. Perchoux, S.J. Wilson, and A.D. Rakic. Rapid scanning flow sensor based on the self-mixing effect in a vcsel. In *Optoelectronic and Microelectronic Materials and Devices (COMMAD), 2010 Conference on*, pages 7–8. IEEE, 2010.

[150] R. Kliese, Y.L. Lim, T. Bosch, and A.D. Rakić. Gan laser self-mixing velocimeter for measuring slow flows. *Optics letters*, 35(6):814–816, 2010.

[151] S.K. Ozdemir, S. Takamiya, S. Ito, S. Shinohara, and H. Yoshida. Self-mixing laser speckle velocimeter for blood flow measurement. *Instrumentation and Measurement, IEEE Transactions on*, 49(5):1029–1035, oct 2000.

[152] Ş.K. Özdemir, S. Shinohara, S. Takamiya, and H. Yoshida. Noninvasive blood flow measurement using speckle signals from a self-mixing laser diode: in vitro and in vivo experiments. *Optical Engineering*, 39:2574, 2000.

[153] S.K. Ozdemir, I. Ohno, and S. Shinohara. Assessment on self-mixing laser interferometry for blood flow measurement over skin surface. In *Instrumentation and Measurement Technology Conference, 2006. IMTC 2006. Proceedings of the IEEE*, pages 27–31. IEEE, 2006.

[154] S.K. Ozdemir, I. Ohno, and S. Shinohara. A comparative study for the assessment on blood flow measurement using self-mixing laser speckle interferometer. *Instrumentation and Measurement, IEEE Transactions on*, 57(2):355–363, 2008.

[155] D. A. Kleinman and P. P. Kisliuk. Discrimination against unwanted orders in the fabry-perot resonator. *Bell Sys. Tech. J.*, 41:453–462, 1962.

[156] H. Kogelnik and C.K.N. Patel. Mode suppression and single frequency operation in gaseous optical masers. *Proceedings of the Institute of Radio Engineers*, 50(11):2365 – 2366, 1962.

[157] J.W. Crowe and Jr. Craig, R.M. Gaas laser linewidth measurements by heterodyne detection. *Applied Physics Letters*, 5:72 – 74, 1964.

[158] O.V. Bogdankevich, B.I. Vasil'ev, A.S. Nasibov, A.N. Pechenov, and K.P. Fedoseev. Spectral characteristics and directionality of a semiconductor laser with an external mirror. *Fizika i Tekhnika Poluprovodnikov*, 4:29 – 34, 1970.

[159] PG Eliseev, I ISMAILOV, and YUF FEDOROV. Injection lasers for multichannel optical communication. QE-6:38 – 41, 1970.

[160] H. Bachert and S. Raab. The influence of external optical coupling on the threshold current density of gaas injection lasers. *Physica Status Solidi*, 29:175 – 8, 1968.

[161] R.F. Broom. Self modulation at gigahertz frequencies of a diode laser coupled to an external cavity. *Electronics Letters*, 5:571 –572, 1969.

[162] V. N. Morozov, V. V. Nikitin, and A. A. Sheronov. Self-synchronization of modes in a gaas semiconductor injection laser. *JETP Lett*, 7:256–258, 1968.

[163] RF Broom, E Mohn, C Risch, and R Salathe. Microwave self-modulation of a diode laser coupled to an external cavity. QE-6:328 – 34, 1970.

[164] R. Lang and K. Kobayashi. External optical feedback effects on semiconductor injection laser properties. *IEEE J. Quantum Electron.*, QE-16(3):347 – 55, 1980.

[165] WM Wang, WJO Boyle, KTV Grattan, and AW Palmer. Self-mixing interference in a diode laser: experimental observations and theoretical analysis. *Applied optics*, 32(9):1551–1558, 1993.

[166] Guy Plantier, Caroline Bes, and Thierry Bosch. Behavioral model of a self-mixing laser diode sensor. *IEEE Journal of Quantum Electronics*, 41(9):1157 – 1167, 2005.

[167] Guido Giuliani, Michele Norgia, Silvano Donati, and Thierry Bosch. Laser diode self-mixing technique for sensing applications. *Journal of Optics A: Pure and Applied Optics*, 4:283–294 –, 2002.

173

[168] G.A. Acket, D. Lenstra, A.J. den Boef, and B.H. Verbeek. The influence of feedback intensity on longitudinal mode properties and optical noise in index-guided semiconductor lasers. *IEEE J. Quantum Electron.*, QE-20(10):1163 − 1169, 1984. feedback intensity;longitudinal mode properties;optical noise;index-guided semiconductor lasers;optical feedback effects;index-guided single-mode semiconductor lasers;characteristic parameter;low-frequency intensity noise;hysteresis;instabilities;.

[169] K. Petermann. *Laser diode modulation and noise*. Advances in Optoelectronics. Kluwer Academic Publishers, Dordrecht, 1991.

[170] CHarles H. Henry. Theory of the linewidth of semiconductor lasers. *IEEE Journal of Quantum Electronics*, QE-18:259 − 264, 1982.

[171] Klaus Petermann. External optical feedback phenomena in semiconductor lasers. *IEEE Journal on Selected Topics in Quantum Electronics*, 1(2):480 − 489, 1995. Optical feedback;Vertical cavity surface emitting laser;Mode hopping noise;Fiber pigtail;Fabry Perot lasers;.

[172] Thierry Bosch, Caroline Bes, Lorenzo Scalise, and Guy Plantier. Optical feedback interferometry. In *Encyclopedia of Sensors*. American Scientific Publishers, 2006.

[173] Deborah M. Kane and K. Alan Shore. *Unlocking Dynamical Diversity: Optical Feedback Effects on Semiconductor Lasers*. John Wiley, 2005.

[174] Yah Leng Lim, K. Bertling, Pierre Rio, J.R. Tucker, and A.D. Rakic. Displacement and distance measurement using the change in junction voltage across a laser diode due to the self-mixing effect. volume 6038 of *Proc. SPIE*, pages 60381O − 1, Brisbane, Australia, 2006.

[175] Russell Kliese, Yah Leng Lim, Karl Bertling, A. Ashrif A. Bakar, Thierry Bosch, and Aleksandar D. Rakic. Self-mixing displacement sensing using the junction voltage variation in a GaN laser. In *Proceedings of the 2008 Conference on Optoelectronic and Microelectronic Materials and Devices*, 2008.

[176] J. Perchoux, H.E. Dougan, F. Bony, and A.D. Rakic. Photodiode-free doppler velocimeter based on self-mixing effect in commercial vcsels. In *Sensors, 2008 IEEE*, pages 290–293, Oct. 2008.

[177] A. Dandridge, R.O. Miles, and T.G. Giallorenzi. Diode laser sensor. *Electronics Letters*, 16:948 −949, 1980.

[178] E.T. Shimizu. Directional discrimination in the self-mixing type laser doppler velocimeter. *Applied Optics*, 26(21):4541 − 4544, 1987.

[179] Thierry Bosch, Noel Servagent, and Frederic Boyer. Vibrations measurements with a self-mixing type laser displacement sensor for modal analysis. 1996.

[180] Thierry Bosch, Noel Servagent, and Marc Lescure. Displacement sensor for spectrum analysis using the optical feedback in a single-mode laser diode. volume 2, pages 870 − 873, Ottawa, Can, 1997. Displacement sensors;Self mixing effects;Optical feedback;.

[181] T. Bosch, N. Servagent, F. Gouaux, and G. Mourat. The self-mixing interference inside a laser diode: application for displacement, velocity and distance measurement. 1998.

[182] Noel Servagent, Thierry Bosch, and Marc Lescure. Laser displacement sensor using the self-mixing effect for modal analysis and defect detection. *IEEE Transactions on Instrumentation and Measurement*, 46(4):847 − 850, 1997.

[183] N. Servagent, F. Gouaux, and T. Bosch. Measurements of displacement using the self-mixing interference in a laser diode. *Journal of Optics*, 29(3):168 − 73, 1998.

[184] S. Donati. Laser interferometry by induced modulation of cavity field. *Journal of Applied Physics*, 49:495 − 497, 1978.

[185] Silvano Donati, Guido Giuliani, and Sabina Merlo. Laser diode feedback interferometer for measurement of displacements without ambiguity. *IEEE Journal of Quantum Electronics*, 31:113 − 119, 1995.

[186] Silvano Donati, Luca Falzoni, and Sabina Merlo. Pc-interfaced, compact laser-diode feedback interferometer for displacement measurements. *IEEE Transactions on Instrumentation and Measurement*, 45:942 − 944, 1996.

174

[187] W.M. Wang, K.T.V. Grattan, A.W. Palmer, and W.J.O. Boyle. Self-mixing interference inside a single-mode diode laser for optical sensing applications. *Journal of Lightwave Technology*, 12(9):1577 − 1587, 1994.

[188] Ming Wang. Fourier transform method for self-mixing interference signal analysis. *Optics and Laser Technology*, 33(6):409 − 16, 2001.

[189] J. Kato, N. Kikuchi, I. Yamaguchi, and S. Ozono. Optical feedback displacement sensor using a laser diode and its performance improvement. *Measurement Science & Technology*, 6(1):45 − 52, 1995.

[190] T. Yoshino, M. Nara, S. Mnatzakanian, B.S. Lee, and T.C. Strand. Laser diode feedback interferometer for stabilization and displacement measurements. *Applied Optics*, 26(5):892 − 7, 1987.

[191] Morio Toyoshima, Tetsuya Ohashi, Shigenobu Shinohara, Hirofumi Yoshida, Hiroaki Ikeda, and Masao Sumi. New digital displacement measuring circuit for aperiodic vibration using self-mixing type ldv. *Conference Record - IEEE Instrumentation and Measurement Technology Conference*, 1:336 − 339, 1994.

[192] Caroline Bes, Guy Plantier, and Thierry Bosch. Displacement measurements using a self-mixing laser diode under moderate feedback. *IEEE Transactions on Instrumentation and Measurement*, 55(4):1101 − 1105, 2006. Displacement measurement;Optical feedback interferometry;Interferometric displacement sensor;.

[193] M. Norgia and S. Donati. A displacement-measuring instrument utilizing self-mixing interferometry. *IEEE Transactions on Instrumentation and Measurement*, 52(6):1765 − 1770, 2003.

[194] J. Hast, L. Krehut, and R. Myllyla. Displacement sensor based on optical feedback interferometry in a gan laser diode. *Optical Engineering*, 44:080504, 2005.

[195] T. Bosch, S. Pavageau, D. D'Alessandro, N. Servagent, V. Annovazzi-Lodi, and S. Donati. A low-cost, optical feedback laser range-finder with chirp-control. 2001.

[196] P.J. de Groot, G.M. Gallatin, and S.H. Macomber. Ranging and velocimetry signal generation in a backscatter-modulated laser diode. *Applied Optics*, 27:4475 − 80, 1988.

[197] P.J. de Groot and G.M. Gallatin. Backscatter-modulation velocimetry with an external-cavity laser diode. *Optics Letters*, 14:165 − 167, 1989.

[198] Shigenobu Shinohara, Minoru Andou, Masafumi Miyata, Hirofumi Yoshida, Hiroaki Ikeda, Jun-ichi Yoshida, Ken-ichi Nishide, Toshio Kondo, and Masao Sumi. High-resolution range finder with wide dynamic range of 0.2 m to 1 m using a frequency-modulated laser diode. volume 3, pages 646 − 651, Philadelphia, PA, USA, 1989.

[199] Shigenobu Shinohara, Hirofumi Yoshida, Hiroaki Ikeda, Ken-ichi Nishide, and Masao Sumi. Compact and high-precision range finder with wide dynamic range using one sensor head. pages 126 − 130, Atlanta, GA, USA, 1991.

[200] Shigenobu Shinohara, Yoshiji Yoshida, Hirofumi Yoshida, Hiroaki Ikeda, Masafumi Miyata, Ken-ichi Nishide, and Masao Sumi. High-precision range finder for slowly moving target with rough surface. volume 1, pages 659 − 664, Pacific Grove, CA, USA, 1990.

[201] Yoshiji Yoshida, Shigenobu Shinohara, Hiroaki Ikeda, Ken-ichi Tada, Hirofumi Yoshida, Ken-ichi Nishide, and Masao Sumi. Application of semiconductor laser range finder to position control of lens in auto-focus camera. volume 3, pages 2357 − 2361, Kobe, Jpn, 1991.

[202] Naoki Tsukuda, Shigenobu Shinohara, Takaaki Shibata, Hirofumi Yoshida, Hiroaki Ikeda, and Masao Sumi. New range-finding speedometer using a self-mixing laser diode modulated by triangular wave pulse current. *Conference Record - IEEE Instrumentation and Measurement Technology Conference*, 1:332 − 335, 1994.

[203] T. Bosch, N. Servagent, R. Chellali, and M. Lescure. A scanning range finder using the self-mixing effect inside a laser diode for 3-d vision. In *Quality Measurements: The Indispensable Bridge between Theory and Reality (No Measurements? No Science!) Joint Conference - 1996: IEEE Instrumentation and Measurement Technology Conference and IMEKO Technical Committee 7. Conference Proceedings*, 1996.

[204] F. Gouaux, N. Servagent, and T. Bosch. Absolute distance measurement with an optical feedback interferometer. *Applied Optics*, 37:6684 − 9, 1998.

[205] N. Servagent, G. Mourat, F. Gouaux, and T. M. Bosch. Analysis of some intrinsic limitations of a laser range finder using self-mixing interference. In R. J. Pryputniewicz, G. M. Brown, and W. P. Jueptner, editors, *Proc. SPIE Vol. 3479, p. 76-83, Laser Interferometry IX: Applications, Ryszard J. Pryputniewicz; Gordon M. Brown; Werner P. Jueptner; Eds.*, volume 3479 of *Presented at the Society of Photo-Optical Instrumentation Engineers (SPIE) Conference*, pages 76–83, 1998.

[206] Eric Gagnon and Jean-Francois Rivest. Laser range imaging using the self-mixing effect in a laser diode. *IEEE Trans. Instrum. Meas.*, 48:693 − 699, 1999.

[207] J.R. Tucker, L. Leng, and A.D. Rakic. Laser range finding using the self-mixing effect in a vertical-cavity surface emitting laser. pages 583 − 6, Sydney, NSW, Australia, 2002.

[208] Michele Norgia, Guido Giuliani, and Silvano Donati. New absolute distance interferometric technique. In Wolfgang Osten and Mitsuo Takeda, editors, *Proceedings of SPIE*, volume 5457, pages 423–431. SPIE, 2004.

[209] F. Vogel and B. Toulouse. A low-cost medium-resolution rangefinder based on the self-mixing effect in a vcsel. *IEEE Transactions on Instrumentation and Measurement*, 54(1):428 − 31, 2005.

[210] K. Bertling, J.R. Tucker, and A.D. Rakic. Optimum injection current waveform for a laser range finder based on the self-mixing effect. volume 5277, pages 334 − 345, Perth, WA, Australia, 2004. Self mixing;Laser range finder;Current reshaping;Optical feedback;.

[211] M.J. Rudd. A laser doppler velocimeter employing the laser as a mixer-oxcillator. *Journal of Scientific Instruments (Journal of Physics E)*, 1:723 − 726, 1968.

[212] S. Shinohara, A. Mochizuki, H. Yoshida, and M. Sumi. Laser doppler velocimeter using the self-mixing effect of a semiconductor laser diode. *Applied Optics*, 25(9):1417 − 1419, 1986.

[213] P.J. de Groot, G.M. Gallatin, and M.F. Cullen. Compact imaging system with ranging and velocimetry. 1988.

[214] Shigenobu Shinohara, Hideaki Naito, Hirofumi Yoshida, Hiroaki Ikeda, and Masao Sumi. Compact and versatile self-mixing type semiconductor laser doppler velocimeters with direction-discrimination circuit. *IEEE Transactions on Instrumentation and Measurement*, 38(2):574 − 577, 1989.

[215] S. Shinohara, H. Naito, H. Yoshida, H. Ikeda, and M. Sumi. High-performance versatile semiconductor laser diode doppler velocimeter. pages 93 − 4, Tsukuba, Japan, 1988.

[216] Taku Aoshima and Junji Ohtsubo. Two-dimensional vector ldv using laser diode frequency change and self-mixing effect. *Optics Communications*, 92:219 − 224, 1992.

[217] E.A. Callan and J.G. McInerney. Measurements of velocities by backscatter modulation in semiconductor injection lasers. 1992.

[218] M.H. Koelink, M. Slot, F.F.M. de Mul, J. Greve, R. Graaff, A.C.M. Dassel, and J.G. Aarnoudse. Laser doppler velocimeter based on the self-mixing effect in a fiber-coupled semiconductor laser: theory. *Applied Optics*, 31:3401 − 3408, 1992.

[219] Guy Plantier, Noel Servagent, Thierry Bosch, and Anthony Sourice. Real-time tracking of time-varying velocity using a self-mixing laser diode. *IEEE Transactions on Instrumentation and Measurement*, 53(1):109 − 115, 2004.

[220] G. Plantier, N. Servagent, A. Sourice, and T. Bosch. Real-time parametric estimation of velocity using optical feedback interferometry. *IEEE Transactions on Instrumentation and Measurement*, 50(4):915 − 919, 2001.

[221] G. Plantier, N. Servagent, A. Sourice, and T. Bosch. A low-cost optical feedback interferometer for real-time velocity measurement. volume vol.2, pages 738 − 43, Baltimore, MD, USA, 2000.

[222] Xavier Raoul, Thierry Bosch, Guy Plantier, and Noel Servagent. A double-laser diode onboard sensor for velocity measurements. *IEEE Transactions on Instrumentation and Measurement*, 53(1):95 − 101, 2004.

[223] Lorenzo Scalise, Yanguang Yu, Guido Giuliani, Guy Plantier, and Thierry Bosch. Self-mixing laser diode velocimetry: Application to vibration and velocity measurement. *IEEE Trans. Instrum. Meas.*, 53(1):223 – 232, 2004.

[224] H.-E. Albrecht, M. Borys, N. Damaschke, and C. Tropea. *Laser Doppler and Phase Doppler Measurement Techniques.* Springer Verlag, Berlin, 2003.

[225] R.H. Hage, T. Bosch, G. Plantier, and A. Sourice. Modeling and analysis of speckle effects for velocity measurements with self-mixing laser diode sensors. In *Sensors, 2008 IEEE*, pages 953–956. IEEE, 2008.

[226] G. Hua-Qiao, L. Liang, H. De-Yong, X. Jun, X. Jian-Ping, Z. Tian-Peng, W. An-Ting, and M. Hai. New laser doppler velocimetry with wide dynamic range and clear directional discrimination. *Chinese Physics Letters*, 22:1344, 2005.

[227] H.C. Hulst and HC Van De Hulst. *Light scattering by small particles.* Dover Pubns, 1957.

[228] C.F. Bohren and D.R. Huffman. Absorption and scattering of light by small particles. *J Wiley & Sons, New York*, 1983.

[229] M.I. Mishchenko. *Light scattering by nonspherical particles: theory, measurements, and applications.* Academic Pr, 2000.

[230] MI Mishchenko. Light scattering by randomly oriented axially symmetric particles. *JOSA A*, 8(6):871–882, 1991.

[231] M.I. Mishchenko, L.D. Travis, and A.A. Lacis. *Scattering, absorption, and emission of light by small particles.* Cambridge Univ Pr, 2002.

[232] G. Gouesbet, B. Maheu, and G. Grehan. Light scattering from a sphere arbitrarily located in a gaussian beam, using a bromwich formulation. *JOSA A*, 5(9):1427–1443, 1988.

[233] G. Gouesbet, G. Gréhan, and B. Maheu. Scattering of a gaussian beam by a mie scatter center using a bromwich formalism. *Journal of optics*, 16:83, 1985.

[234] G. Grehan, B. Maheu, and G. Gouesbet. Scattering of laser beams by mie scatter centers: numerical results using a localized approximation. *Applied optics*, 25(19):3539–3548, 1986.

[235] J.M. Taylor. Scattering theory. *Optical Binding Phenomena: Observations and Mechanisms*, pages 11–49, 2011.

[236] M.I. Mishchenko, J.W. Hovenier, and D.W. Mackowski. Single scattering by a small volume element. *JOSA A*, 21(1):71–87, 2004.

[237] A. Quirantes, F. Arroyo, and J. Quirantes-Ros. Multiple light scattering by spherical particle systems and its dependence on concentration: a t-matrix study. *Journal of colloid and interface science*, 240(1):78–82, 2001.

[238] Joseph T. Verdeyen. *Laser electronics.* Prentice-Hall, Englewood Cliffs, N.J. :, 1981.

[239] J.T. Verdeyen. Laser electronics. 1989.

[240] AN Bashkatov, EA Genina, VI Kochubey, and VV Tuchin. Optical properties of human skin, subcutaneous and mucous tissues in the wavelength range from 400 to 2000 nm. *Journal of Physics D: Applied Physics*, 38:2543, 2005.

[241] Yah Leng Lim. *Self-mixing sensors based on monolithic VCSEL arrays: A new approach to imaging.* PhD thesis, School of Information Technology and Electrical Engineering, The University of Queensland, 2011.

[242] F.F.M. de Mul, M.H. Koelink, M.L. Kok, P.J. Harmsma, J. Greve, R. Graaff, and J.G. Aarnoudse. Laser doppler velocimetry and monte carlo simulations on models for blood perfusion in tissue. *Applied Optics*, 34(28):6595 – 611, 1995. laser Doppler velocimetry;Monte Carlo simulations;tissue blood perfusion models;optical sample volume dimensions;heterodyne scattering;homodyne scattering;laser penetration angle;laser-detector distance;780 nm;.

[243] R. Graaff, MH Koelink, FFM De Mul, WG Zijistra, ACM Dassel, and JG Aarnoudse. Condensed monte carlo simulations for the description of light transport. *Applied optics*, 32(4):426–434, 1993.

[244] HW Jentink, FFM De Mul, R. Hermsen, R. Graaff, and J. Greve. Monte carlo simulations of laser doppler blood flow measurements in tissue. *Applied optics*, 29(16):2371–2381, 1990.

[245] V. Twersky. Absorption and multiple scattering by biological suspensions. *JOSA*, 60(8):1084–1093, 1970.

[246] V. Twersky. Multiple scattering of waves and optical phenomena. *JOSA*, 52(2):145–169, 1962.

[247] R.F. Bonner and R. Nossal. Principles of laser-doppler flowmetry. *Laser-Doppler Blood Flowmetry, AP Shepherd and PÅ Öberg, Eds*, pages 17–45, 1990.

[248] Klaus Schätzel. Suppression of multiple scattering by photon cross-correlation techniques. *Journal of Modern Optics*, 38(9):1849–1865, 1991.

[249] J. G. Santiago, S. T. Wereley, C. D. Meinhart, D. J. Beebe, and R. J. Adrian. A particle image velocimetry system for microfluidics. *Experiments in Fluids*, 25:316–319, 1998. 10.1007/s003480050235.

[250] M. Spiga and GL Morino. A symmetric solution for velocity profile in laminar flow through rectangular ducts. *International communications in heat and mass transfer*, 21(4):469–475, 1994.

[251] M. Stucker, I. Horstmann, C. Nuchel, A. Rochling, K. Hoffmann, and P. Altmeyer. Blood flow compared in benign melanocytic naevi, malignant melanomas and basal cell carcinomas. 1999.

[252] V.V. Tuchin. Tissue optics: light scattering methods and instruments for medical diagnosis. SPIE-International Society for Optical Engineering, 2007.

[253] C. Riva, B. Ross, and G.B. Benedek. Laser doppler measurements of blood flow in capillary tubes and retinal arteries. *Investigative Ophthalmology & Visual Science*, 11(11):936–944, 1972.

[254] R. Bonner and R. Nossal. Model for laser doppler measurements of blood flow in tissue. *Appl. Opt.*, 20(12):2097–2107, Jun 1981.

[255] M.J. Leahy, F.F.M. de Mul, G.E. Nilsson, and R. Maniewski. Principles and practice of the laser-doppler perfusion technique. *Technology and Health Care*, 7(2-3):143 – 62, 1999. laser-Doppler perfusion technique;microvascular blood perfusion;instrumentation basic principles;standardisation;calibration method;basic theoretical background;perfusion monitors;perfusion imagers;medical instrumentation;.

[256] Z. Chen, T.E. Milner, S. Srinivas, X. Wang, A. Malekafzali, M.J.C. van Gemert, and J.S. Nelson. Noninvasive imaging of< i> in vivo</i> blood flow velocity using optical doppler tomography. *Optics letters*, 22(14):1119–1121, 1997.

[257] Z. Chen, T.E. Milner, D. Dave, and J.S. Nelson. Optical doppler tomographic imaging of fluid flow velocity in highly scattering media. *Optics letters*, 22(1):64–66, 1997.

[258] Xiao-jun Wang, Thomas E. Milner, Zhongping Chen, and J. Stuart Nelson. Measurement of fluid-flow-velocity profile in turbid media by the use of optical doppler tomography. *Applied Optics*, 36(1):144 –, 1997.

[259] J.M. Schmitt. Optical coherence tomography (oct): a review. *Selected Topics in Quantum Electronics, IEEE Journal of*, 5(4):1205 –1215, jul/aug 1999.

Le phénomène d'interférométrie par réinjection optique, ou effet « self-mixing » dans un laser permet de concevoir des capteurs non-invasifs, auto-alignés et ne nécessitant que peu d'éléments optiques. Ce type de capteurs a été développé pour des mesures de déplacement, de vitesse ou de distance de cibles dite coopératives (cibles réfléchissantes ou fortement diffusantes). Dans cette étude, ce type de capteurs est appliqué à la mesure de débits et de profil d'écoulement de fluides dans des microcanaux. Le faible coût et la polyvalence probable des capteurs à réinjection optique sont d'un grand intérêt dans l'industrie biomédicale et chimique, ainsi que pour la recherche en mécanique des fluides. Dans un premier temps, et en se basant sur les études réalisées dans des macro-canaux, nous avons proposé un modèle d'interferométrie par réinjection optique dans une diode laser lorsque la cible est constitué de particules en mouvement, en suspension dans un liquide. A partir de ce modèle, nous avons étudié expérimentalement l'impact de la taille du faisceau ainsi que de la taille et concentration des particules sur la tension de jonction de la diode laser. Nous avons ensuite proposé des méthodes de traitement du signal permettant le calcul du débit du fluide, ainsi que sous certaines conditions, la mesure de vitesse locale en tout point d'un microcanal. Ces études préliminaires nous ont permis de reconstruire le profil d'écoulement de différents liquides dans des canaux de 320 µm de diamètre. Enfin, nous avons comparé les performances du capteur développé dans cette thèse avec un capteur basé sur la technique du Dual-slit en mesurant le profil d'écoulement dans des canaux de 100x20 µm.

The phenomenon of optical feedback interferometry or "self-mixing" effect in a laser is used to design non-invasive sensors, self-aligned and requiring only a few optical elements. This type of sensor was previously proposed to measure the displacement, velocity or distance from cooperative target (reflective targets or strongly scattering). In this study, this type of sensor is applied to the measurement of flow rate and fluid flow profile in microchannels. Possible low cost and versatility of optical feedback sensors would be of great interest in biomedical and chemical industry as well as for research in fluid mechanics. As a first step, and based on studies in macro-channels, we proposed a model of optical feedback interferometry in a laser diode when the target consists of moving particles suspended in a liquid. From this model, we studied experimentally the impact of the beam shape and the size and concentration of the particles on the junction voltage of the laser diode. We then proposed signal some processing methods for calculating the fluid flow, and under certain conditions, the local velocity at any point in a microchannel. These preliminary studies allowed us to reconstruct the flow profile of different liquids in a channel of 320 µm diameter. Finally, we compared the performance of the sensor developed in this thesis with a sensor based on the dual-slit technique by measuring the flow profile in a rectangular shaped channel (100x20 µm).

179